Spring 1-20-2014

Optimization of Wind Turbine Airfoils/Blades and Wind Farm Layouts

Xiaomin Chen
Washington University in St. Louis

WASHINGTON UNIVERSITY IN ST. LOUIS

School of Engineering and Applied Science

Department of Mechanical Engineering & Materials Science

Dissertation Examination Committee:
Ramesh Agarwal, Chair
Ken Jerina
Norman Katz
Mori Mani
David Peters
Palghat Ramanchandran

Optimization of Wind Turbine Airfoils/Blades and Wind Farm Layouts

by

Xiaomin Chen

A dissertation presented to the
Graduate School of Arts and Sciences
of Washington University in
partial fulfillment of the
requirements for the degree
of Doctor of Philosophy

May 2014

Saint Louis, Missouri

Table of Contents

List of Figures

List of Tables

Nomenclature

Nomenclature

a_n	normal induction factor (of v_n)
a_t	tangential induction factor (of v_t)
B	number of wind turbine blades
c	chord length of an airfoil
C_l	section lift coefficient
C_d	section drag coefficient
C_L	lift coefficient
C_D	drag coefficient
D	drag force
F_n	force normal to the rotor plane
F_t	force tangential to the rotor plane
L	lift force
M	Mach number
R	blade radius
Re	Reynolds number
R_{tip}	hub radius
t	maximum thickness of the airfoil
U_∞	free stream wind speed
v_n	normal component of induced velocity to the rotor plane
V_n	inflow velocity in the normal direction
v_t	tangential component of induced velocity to the rotor plane
V_t	inflow velocity in the tangential direction
W	absolute value of the inflow velocity

Greeks

α	angle of attack

Θ	pitch of the blade element
λ	tip speed raito
λ_r	local tip speed ratio
μ	dynamic viscosity of air
ν	kinematic viscosity
ρ	density of the fluid
σ	solidity of wind turbine blade
ϕ	inflow angle
ω	angle velocity of the blade wake
Ω	rotational speed of wind turbines

Abbreviations

BEM	blade element momentum
BSDS	Blade System Design Study
CFD	Computational Fluid Dynamics
FB	Flatback
GA	Genetic Algorithm
HAWT	Horizontal Axis Wind Turbine
MOGA	Multi-Objective Genetic Algorithm
NREL	National Renewable Energy Laboratory
NURBS	Non-Uniform Rational Basic Spine
RANS	Reynolds-averaged Navier Stokes
SOGA	Single-Objective Genetic Algorithm
VAWT	Vertical Axis Wind Turbine

Acknowledgments

This dissertation is my remarkable achievement of many years of dedication towards innovative science and technologies. I feel extremely blessed for all the support and inspiration I have received from many professors, family members and friends, who directly and indirectly contributed this work. I would especially like to thank my advisor, Dr. Ramesh K. Agarwal, for his tremendous commitment and wholehearted guidance, and his profound wisdom during my doctoral study at Washington University. His expertise and personality have inspired me in many ways towards my growth as a science researcher. It has been a pleasant and fascinating journey for the past five years and I was honored to be under his direction.

I would like to extend my gratefulness to the professors who have supported and advised me all the way. They are Dr. David Peters, Dr. Daren Chen, Dr. Ken Jerina, Dr. Mori Mani, Dr. Norman Katz, Dr. Palghat Ramanchandran and Dr. Philip Bayly.

I also want to thank my colleagues in the MEMS department and my friends all over the world. It has been an enjoyment to have them in my life and to taste the bitterness and sweetness of life together with them.

I especially want to thank my family for everything. They are always there for me no matter what, and never want anything back in return. Their biggest wish is for me to live a happy life.

Xiaomin Chen

Washington University in St. Louis
January 2014

To my beloved family, my Dad Weikun Chen and Mom Cuihong Le

ABSTRACT OF THE DISSERTATION

Optimization of Wind Turbine Airfoil/Blades and Wind Farm Layouts

by

Xiaomin Chen

Doctor of Philosophy in Mechanical Engineering

Washington University in St. Louis, 2014

Professor Ramesh K. Agarwal, Chair

Shape optimization is widely used in the design of wind turbine blades. In this dissertation, a numerical optimization method called Genetic Algorithm (GA) is applied to address the shape optimization of wind turbine airfoils and blades. In recent years, the airfoil sections with blunt trailing edge (called flatback airfoils) have been proposed for the inboard regions of large wind-turbine blades because they provide several structural and aerodynamic performance advantages. The FX, DU and NACA 64 series airfoils are thick airfoils widely used for wind turbine blade application. They have several advantages in meeting the intrinsic requirements for wind turbines in terms of design point, off-design capabilities and structural properties. This research employ both single- and multi-objective genetic algorithms (SOGA and MOGA) for shape optimization of Flatback, FX, DU and NACA 64 series airfoils to achieve maximum lift and/or maximum lift to drag ratio.

The commercially available software FLUENT is employed for calculation of the flow field using the Reynolds-Averaged Navier-Stokes (RANS) equations in conjunction with a two-equation Shear Stress Transport (SST) turbulence model and a three equation k-kl-ω turbulence model. The optimization methodology is validated by an optimization study of subsonic and

transonic airfoils (NACA0012 and RAE 2822 airfoils). All the optimization results have demonstrated that the GA technique can be employed efficiently and accurately to produce globally optimal airfoils with excellent aerodynamic properties using a desired objective value (minimum C_d and/or maximum C_l /C_d). It is also shown that the multi-objective genetic algorithm based optimization can generate superior airfoils compared to those obtained by using the single objective genetic algorithm.

The applications of thick airfoils are extended to the assessment of wind turbine performance. It is well established that the power generated by a Horizontal-Axis Wind Turbine (HAWT) is a function of the number of blades B, the tip speed ratio λ (blade tip speed/wind free stream velocity) and the lift to drag ratio (C_l/C_d) of the airfoil sections of the blade. The airfoil sections used in HAWT are generally thick airfoils such as the S, DU, FX, Flat-back and NACA 6-series of airfoils. These airfoils vary in (C_l/C_d) for a given B and λ, and therefore the power generated by HAWT for different blade airfoil sections will vary. Another goal of this study is to evaluate the effect of different airfoil sections on HAWT performance using the Blade Element Momentum (BEM) theory.

In this dissertation, we employ DU 91-W2-250, FX 66-S196-V1, NACA 64421, and Flat-back series of airfoils (FB-3500-0050, FB-3500-0875, and FB-3500-1750) and compare their performance with S809 airfoil used in NREL Phase II and III wind turbines; the lift and drag coefficient data for these airfoils sections are available. The output power of the turbine is calculated using these airfoil section blades for a given B and λ and is compared with the original NREL Phase II and Phase III turbines using S809 airfoil section. It is shown that by a suitable choice of airfoil section of HAWT blade, the power generated by the turbine can be significantly

increased. Parametric studies are also conducted by varying the turbine diameter. In addition, a simplified dynamic inflow model is integrated into the BEM theory. It is shown that the improved BEM theory has superior performance in capturing the instantaneous behavior of wind turbines due to the existence of wind turbine wake or temporal variations in wind velocity.

The dissertation also considers the Wind Farm layout optimization problem using a genetic algorithm. Both the Horizontal –Axis Wind Turbines (HAWT) and Vertical-Axis Wind Turbines (VAWT) are considered. The goal of the optimization problem is to optimally position the turbines within the wind farm such that the wake effects are minimized and the power production is maximized. The reasonably accurate modeling of the turbine wake is critical in determination of the optimal layout of the turbines and the power generated. For HAWT, two wake models are considered; both are found to give similar answers. For VAWT, a very simple wake model is employed.

Finally, some preliminary investigation of shape optimization of 3D wind turbine blades at low Reynolds numbers is conducted. The optimization employs a 3D straight untapered wind turbine blade with cross section of NACA 0012 airfoils as the geometry of baseline blade. The optimization objective is to achieve maximum C_l/C_d as well as maximum C_l. The multi-objective genetic algorithm is employed together with the commercially available software FLUENT for calculation of the flow field using the Reynolds-Averaged Navier-Stokes (RANS) equations in conjunction with a one-equation Sparlart-Allmaras turbulence model. The results show excellent performance of the optimized wind turbine blade and indicate the feasibility of optimization on real wind turbine blades with more complex shapes in the future.

Chapter 1 Introduction

1.1 Overview

There has been continuous development and utilization of wind energy since the 1980s. Part of the reason has been the oil crisis of the 1970s and even more so the anti-nuclear power movement of 1980s. In recent year, one of the key reasons has been the increased environmental concerns caused by the used of traditional fossil fuel energy sources such as coal and oil. Figure 1-1 shows the increase in wind power capacity of the whole world in recent decades.

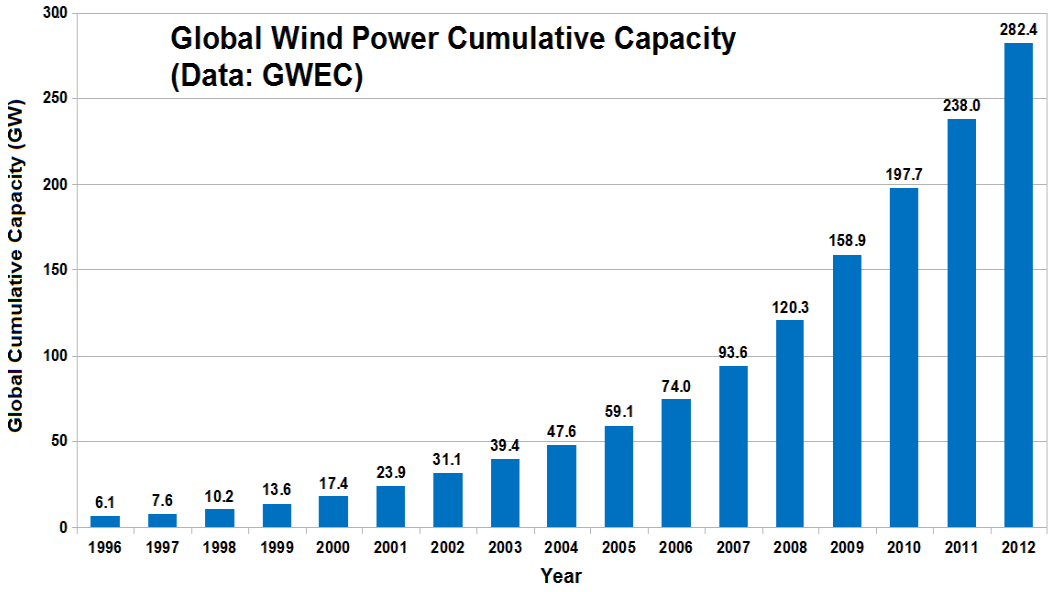

Figure 1-1 Global wind power cumulative capacity [1]

The advantage of wind energy is that it's clean and doesn't pollute the air like the traditional power plants that rely on combustion of fossil fuels. There are no atmospheric emissions that cause acid rain or create greenhouse gases [2]. Wind energy is also renewable and is abundant. As long as there is solar energy which heats up the atmosphere and causes the

motion of air, wind energy will always exist. It's also abundant in all parts of the world where wind speeds are significant.

U.S. is among the first few countries to utilize wind energy at large production scale. In 1980 the world's first wind farm, consisting of twenty 30kW wind turbines was installed at Crotched Moutain in New Hampshire [3]. Ever since, both the installed wind power generating capacity and the generated wind power have has grown exponentially. Figure 1-2 (a) and (b) illustrate the huge increase in wind power recent decades.

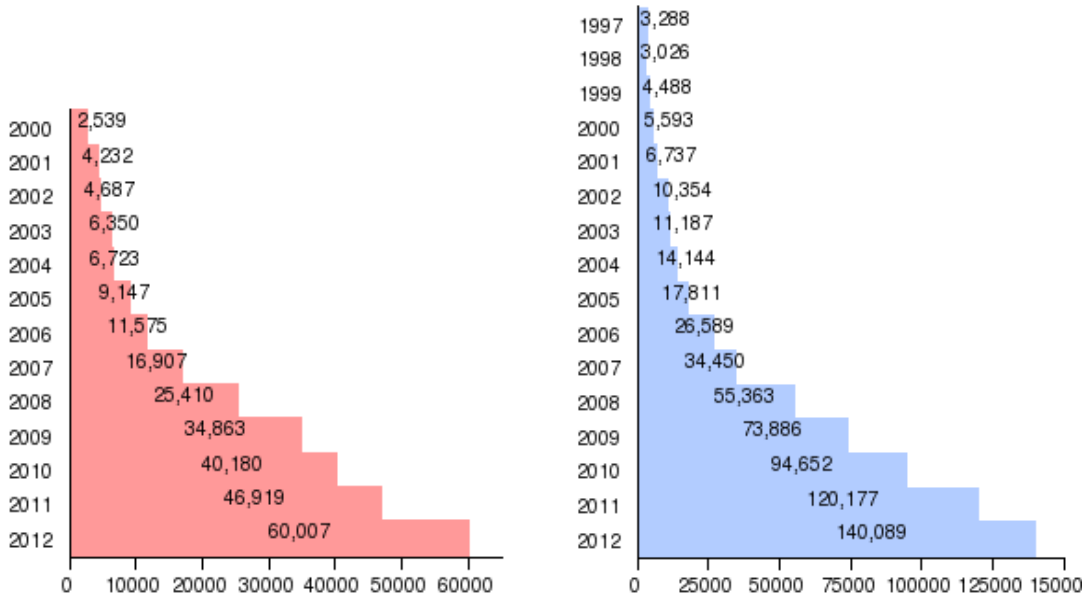

(a) (b)

Figure 1-2 (a) Megawatts of installed wind power generating capacity since 2001 [4, 5] (b) Thousand megawatthours generated since 1997 [6]

Currently, US ranks second in the world in terms of installed wind power capacity. Figure 1-3 is a map illustrating installed wind power generating capacity in various states of the United States. Most of them are in the middle and south and on the west coast. As of December 2012, the top five states with the most wind power capacity installed are [7]: Texas (12,212 MW), California (5,549MW), Iowa (5,137 MW), Illinois (3,568 MW) and Oregon (3,158 MW). The United States generates more electricity than either Germany or China for the same installed capacity. The top five states according to percentage of power generation by wind in 2012 are [8]: Iowa (24.5%), South Dakota (23.9%), North Dakota (14.7%), Minnesota (14.3%) and Kansas (11.4%)

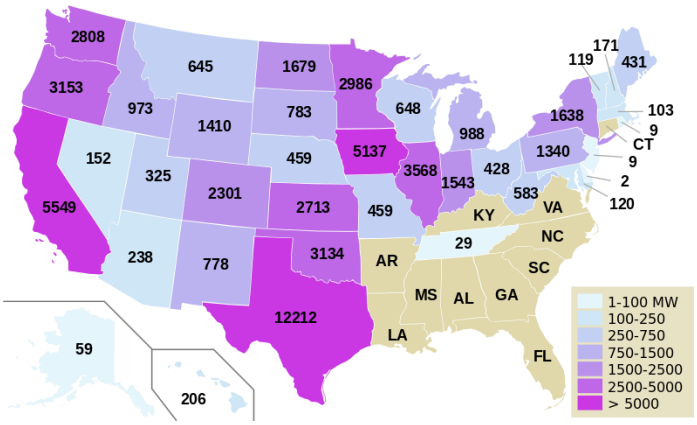

Figure 1-3 Map illustrating installed wind power generating capacity for U.S. states at the end of 2012 [9]

1.2 Wind Turbines

Wind turbines are the most important part of the wind energy industry. They are the machines which convert wind power to electrical energy. There can be many different types of them. For mass production industry, they are mainly divided into two types: Horizontal Axis Wind Turbine (HAWT) and Vertical Axis Wind Turbine (VAWT). They are the mature designs from decades of investigation and have been used throughout the world as a sustainable source of power supply. HAWT and VAWT are quite different in that HAWTs have the main rotor shaft and electrical generator at the top of a tower and must be pointed into the direction of the wind while VAWTs have the main rotor shaft arranged vertically. Figure 1-4 and 1-5 show examples of HAWT and VAWT respectively. Figure 1-4 is a wind farm installed with three-bladed HAWTs and Figure 1-5 is a VAWT wind farm using Darius type VAWTs.

Figure 1-4 An example of off-shore HAWT wind farm [10]

Figure 1-5 An example of Darius type VAWT wind farm [11]

Both HAWTs and VAWTs have their advantages: HAWTs are more commonly used because of their high efficiency in power production while VAWTs are more suitable on sites where the wind direction is highly variable and also they can be easily integrated into buildings. The disadvantages for HAWTs are that they need higher wind speeds to start generating

electricity and also become less efficient at producing power in very high winds over 90 MPH. They cannot be installed in turbulent wind conditions because they must point into the wind direction to produce power and their blades are structurally less strong as wind speeds increase. Therefore they cannot withstand extreme weather conditions due to frost, freezing rain or heavy snow plus heavy winds in excess of 110MPH. The key disadvantages of VAWTs include the low rotational speed with the consequential higher torque and hence higher cost of the drive train, the inherently lower power coefficient, the 360 degree rotation of the aerofoil within the wind flow during each cycle and hence the highly dynamic loading on the blade, the pulsating torque generated by some rotor designs on the drive train, and the difficulty of modeling the wind flow accurately and hence the challenges of analyzing and designing the rotor prior to fabricating a prototype [12]. In this dissertation, the major focus of design and optimization is HAWT because they are more commonly used. Some study and discussion of VAWT are also included.

During the operation of HAWT, it is the turbine blades mounted on the hub of the wind turbine that experience forces and capture the wind energy. Modern wind turbines use principles of aerodynamics to realize the full potential of rotating wind blades. A turbine blade looks like an aircraft wing as shown in Figure 1-6. The difference is that the wind turbine blades are usually twisted with varying chord and thickness along the blade from root to tip; they are thicker at the root and thinner at the tip.

Figure 1-6 An example of Horizontal-Axis Wind Turbine (HAWT) [13]

The cross section of a wind turbine blade is an airfoil as shown in Figure 1-7. The geometry of the airfoil has a direct effect on the coefficient of lift and drag; the airfoil curvature creates a lower pressure region above the airfoil and higher pressure region below the airfoil resulting in a net force acting on the airfoil. The net force is customarily resolved into two components, one perpendicular and the other parallel to the oncoming wind. The two force components are called lift and drag force respectively. The lift force has a component that produces power on turbine rotation, whereas the drag force has a component that impacts negatively on power production.

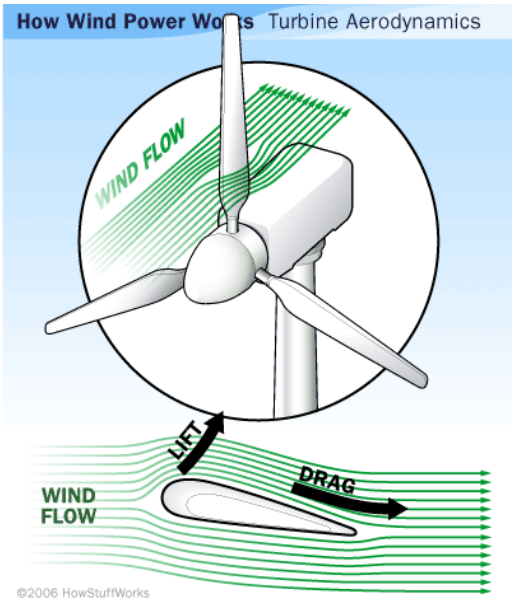

Figure 1-7 An example of wind turbine airfoil [9]

1.3 Wind Farms

Generally, power companies rely on wind farms instead of individual wind turbines to provide large-scale power. Wind farm is a group of wind turbines installed on one fixed site to provide significant amount of wind energy. A large wind farm usually requires hundreds of square miles of area for installation of hundreds of wind turbines. Wind farms can be classified as HAWT wind farms and VAWT wind farms based on the type of wind turbines installed. They are also classified as onshore wind farms and offshore wind farms depending upon their installation area. Compared to onshore wind farms, offshore wind farms enjoy considerably higher capacity

factors because the average wind speed over sea is usually much higher than the wind speed over the land surface. Figure 1-8 and 1-9 show examples of onshore and offshore wind farms respectively.

Figure 1-8 Example of onshore wind farm: the Shepherds Wind Farm [14]

Figure 1-9 Example of offshore wind farm near Copenhagen, Denmark [15]

1.4 CFD, BEM and Genetic Algorithms

1.4.1 Introduction to CFD

CFD is the abbreviation for Computational Fluid Dynamics. It is a branch of fluid mechanics that uses numerical methods and algorithms to solve the governing equations of fluid flow and provide useful information for analysis and design of systems involving fluid flow. CFD based

analysis requires computers to perform the calculations. The main advantage of CFD is that it can be used to solve very complex fluid flow problems.

The CFD analysis procedures are generally divided into three steps: pre-processing, simulation and post-processing. During the preprocessing, the geometry of the problem is defined and the volume occupied by the fluid is divided into discrete cells known as the mesh. The simulation step involves discretizing the governing equations on the mesh generated in the first step by employing a suitable numerical algorithm. The discretized equations are then solved on a computer and the values of the flow variables are obtained at the mesh points. In the final post-processing step, the simulation data is analyzed, visualized and used for producer improvement and design.

1.4.2 Introduction to BEM

Blade Element Momentum (BEM) Theory is a calculation method that is commonly used to determine the performance of a wind turbine. It provides a good estimate of power generated by a HAWT of a given diameter and number of blades for a given wind speed.

The BEM theory combines two methods to describe the aerodynamic behavior of a wind turbine. The first method is based on the Momentum Theory which uses momentum balance on a rotating annular stream tube passing through an actuator disc model of a wine turbine. The second method is based on the Blade Element Theory which evaluates the forces generated at various sections along the blades. By equating the force and torque relations derived separately from momentum and blade element theory, the induced velocities and induction factors at the actuator disk can be predicted. Once induced velocities are modeled accurately, the power and thrust of a wind turbine can be determined.

1.4.3 Genetic Algorithms

The traditional optimization algorithms are not adequate to solve the airfoil/blade shape optimization and wind farm optimization problems considered in this dissertation. The traditional approaches rely on real functions to compute the objective values, which can get stuck in local optima so that it becomes difficult to obtain the global optimization solutions. Besides, the traditional methods also have difficulties in handling large number of parameters. The optimization problems considered in this dissertation require CFD software to evaluate the objective values such as lift and drag of a blade and also deal with relative large number of variables (e.g. in case of wind farm optimization). Therefore, we don't use the traditional optimization algorithms in the dissertation.

We employ a Genetic Algorithm as the optimization technique for solving the optimization problems considered in this dissertation. Genetic algorithms are a class of evolutionary algorithms which generate solutions to optimization problems in a wide range of applications including bioinformatics, phylogenetics, computational science and engineering, economics, chemistry, manufacturing, mathematics, physics, pharmacometrics, etc.

Genetic algorithms mimic the natural evolution process by using techniques such as inheritance, selection, crossover, and mutation. Each process function is the realization of one evolution process. Figure 1-10 is an illustration of the general iteration process involved in using GA for obtaining an optimized solution. Every generation contains a number of solutions (x) whose performances are evaluated. Those with better performance are selected through natural selection. They are chosen as the parent (solutions) to create children (solutions) through crossover. Mutation mimics the natural genetic mutation in order to add diversity to the solution set, thus preventing the local optimization. Thus, a new group of solution set is created which goes to the next generation. This procedure continues until convergence to a solution with optimal objective value/s is achieved. This solution is optimized solution to the problem under consideration.

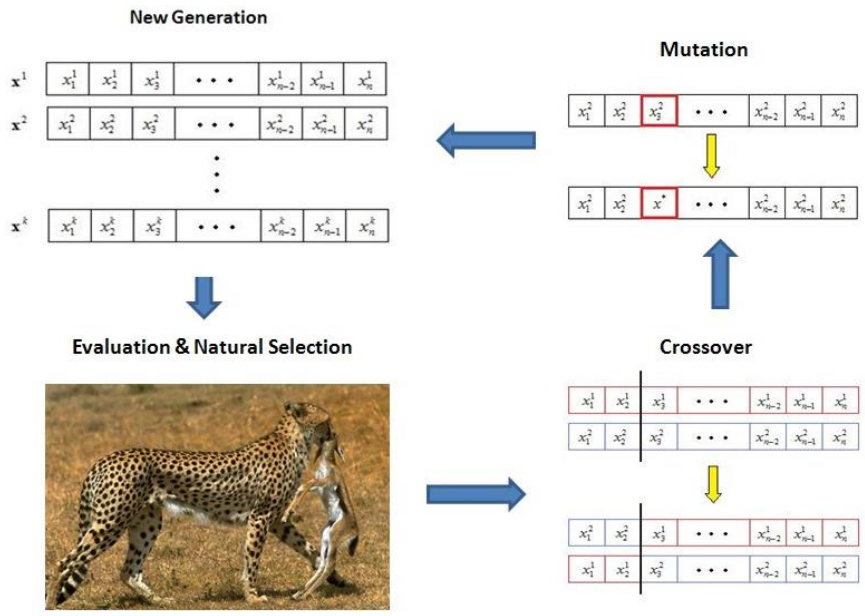

Figure 1-10 An illustration of the general iteration process using GA for achieving the optimized solution

1.5 Dissertation Outline

This dissertation consists of 11 chapters. Chapter 2 describes the importance wind energy. It emphasizes why it is important to optimize the shape of wind turbine airfoils/blades and how the optimized shapes affect the wind-harvesting performance of a wind turbine. Optimization of wind farm layouts is introduced. The application of genetic algorithms to these two optimization problems is explained.

Chapter 3 reviews previous work on wind turbines and wind farm optimization. A brief review of previous work on optimization methods is also given.

Chapter 4 explains the optimization methodology used in the dissertation. Both the Single-objective Genetic Algorithms (SOGA) and Multi-objective Genetic Algorithm (MOGA) are introduced. The chapter also explains the entire optimization process and how GA, CFD and the Bezier curves interact with each other. The shape parameterization method is also introduced.

Chapter 5 presents the results of benchmark used for validating the optimization methodology. The validation cases consider the optimization of RAE 2822 and NACA 0012

airfoils at subsonic and transonic speeds. By showing the superior aerodynamic performance of the optimized RAE 2822 and NACA0012 airfoils, the results in this chapter proves that the GA technique can be employed efficiently and accurately to produce globally optimal airfoils with excellent aerodynamic properties using a desired objective value, and the application of multi-objective GA can result in superior shock-free airfoils by minimizing the drag and maximizing the lift to drag ratio.

In Chapter 6, GA techniques are applied to the shape optimization of thick airfoils including Flatback airfoils, FX 66-S196-V1, DU 91-W2-250, NACA 64418 and NACA 64421 airfoils. The optimization results show that the application of multi-objective GA can result in superior airfoils by maximizing both the lift and lift to drag ratio.

Chapter 7 presents the application of BEM theory to 3D wind turbines. This chapter has two parts. The first part focuses on assessing the wind turbine performance for power generation using thick airfoils from Chapter 6 for blades sections of NREL II, III and Risoe wind turbines. The second part focuses on modifying the BEM theory by including a simplified dynamic inflow model to capture the instantaneous response of wind turbines due to changes in the input operating conditions.

Chapter 8 presents the results of wind farm layout optimization. The optimization results for a HAWT wind farms are first shown by employing several wind turbine wake models. Then the development of a simple wake model for a VAWT is presented and the optimization results for a VAWT wind farm are given.

Chapter 9 shows the results of a preliminary investigation on shape optimization of a 3D wind turbine blade at low Reynolds number. The optimization is based on a 3D straight untapered wind turbine blade with the cross section shape of NACA 0012 airfoil with the optimization objective of achieving maximum C_l/C_d as well as maximum C_l. The results show excellent performance of the optimized wind turbine blade and indicate the promise of optimization of geometrically more complex blade shapes.

Chapter 10 provides the conclusion of all the work described in Chapter 1-9. Chapter 11 mentions some ideas for future work.

Chapter 2 Motivation

2.1 Overview

Modern world relies heavily on energy. We need all kinds of energy sources to support our economic and other activities in daily life, such as industry production, transportation, entertainment, communication, etc. Electric power is one of the most important energy engines for sustaining modern life. Modern human societies cannot function without electricity power.

We are currently facing challenging energy issues. On one hand, the most commonly used traditional fossil fuel sources such as coal, petroleum and natural gas are limited. They will be depleted in not too distant a future. The solution is to find the replacement for these traditional sources of energy. On the other hand, decades of use of fossil fuels has created severe global environmental issues such as global warming which have again necessitated the need for environment-friendly energy sources. The new energy source should be clean, emission-free and renewable. Therefore, due to increasing demand for clean, emission-free energy and also due to the foreseeable depletion of fossil fuel sources in the future, wind energy (among other renewable energy sources) has been receiving considerable attention in recently years as an important low cost alternative to traditional fossil fuel energy sources. In past several decades, there has been increased effort on wine energy research to make it cost effective and efficient.

In wind industry, in recent year the aerodynamic and structural optimization of wind turbines and the optimization of wind farm layouts for maximum power production with minimum land use have been the subject of great deal of research. For wind turbines, one of the most important design criteria is to maximize the harvested wind energy while satisfying other conditions such as structural integrity, economics, geography, etc. Therefore, wind turbine design is a multidisciplinary design process. Figure 2-1 shows the schematic of the design process. Among various areas, optimization of aerodynamics is a major component of wind

turbine design because the power production of a wind turbine is directly affected by its aerodynamic performance.

The realization of aerodynamic optimization lies in the optimization of wind turbine shape including the airfoil/blade shape. The reason is that various airfoil shapes result in different lift and drag forces and therefore in different power curves. The aerodynamically efficient design of wind turbine heavily relies on the shape of airfoils/blades. Which airfoil/blade shape could result in greater power is an important area of research in wind turbine aerodynamics.

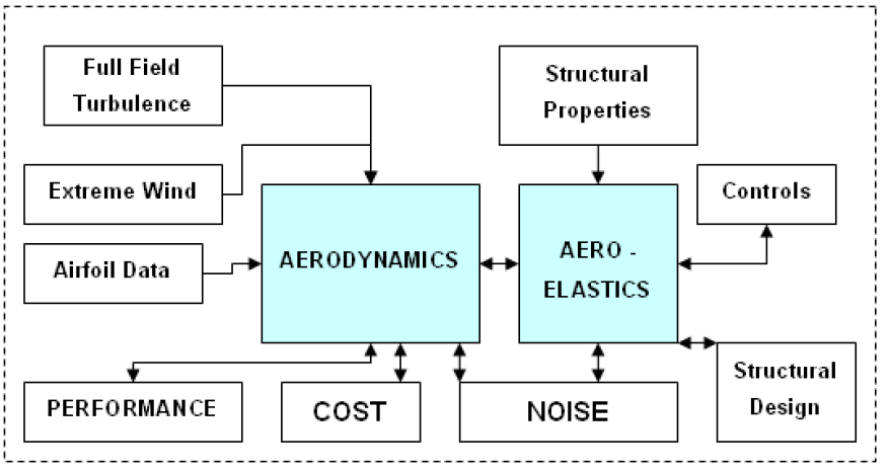

Figure 2-1 Wind turbine design process [16]

Optimization of wind turbines distribution in a wind farm is another problem of interest in the utilization of wind energy. Although there exist many individual wind turbines in the suburban areas of cities, for multi-megawatt production a large number of wind turbines are required to be installed in a land are that has excellent wind speed. The efficiency of a wind-farm is highly influenced by positioning of wind turbines because the flow interference due to turbines' wakes can adversely impact the overall power generation.

This dissertation focuses on the above two optimization problems – the aerodynamic optimization of a wind turbine airfoils/blade and the optimization of a wind-farm layout. The topics include the shape optimization of wind turbine airfoils/blades, the assessment of the performance of various airfoil sections on power generation from a wind turbine and the optimization of wind turbines distribution in wind farms. The optimization targets include the

maximization of aerodynamic performance parameters for airfoils/blades, and the maximization of power output for either individual wind turbine or a group of them in wind farms.

2.2 Optimization of Wind-Turbine Airfoils and Blades

The aerodynamic characteristics of wind turbine airfoils/blades rely highly on their shapes. The geometry of an airfoil can directly affect the lift and drag coefficients during operation and in turn affect the amount of energy a wind turbine can generate [17]. Improving the shapes of airfoils/blades can effectively improve wind turbine performance in energy harvesting. Therefore, we consider the aerodynamic shape optimization of wind turbine airfoils/blades as a topic of research in this dissertation.

Shape optimization is an important branch in design optimization that basically involves determination of the shape of an object so as to minimize or maximize an objective function subject to design constraints. It is widely used in industry and business to improve products as well as to reduce risks due to bad designs. Wind-turbine designers use shape optimization to improve its performance in utilizing wind energy. In vehicle industry, manufacturers use shape optimization to determine what kind of car shapes can reduce drag. It is also applied to the design of diffusers to maximize the recovery of static pressure. In aircraft industry, shape optimization can help in improving the aerodynamic properties by increasing lift and reducing drag.

This study focuses on shape optimization of 2D airfoils and 3D blades to improve their aerodynamic characteristics, in particular to achieve two targets: increase the lift and reduce the drag. A combination of lift and drag, which is the lift-to-drag ratio (*L/D* ratio), is also used as an optimization target combined with lift force maximization.

The reason behind wind turbine designers focusing on optimizing the *L/D* ratio is that the rotor blade of a wind turbine acts like a wing with lift force turning the blade around the wind turbine axis and thereby driving an electric generator to generate electricity. The energy produced by a wind turbine scales with the lift-to-drag ratio and the rotational speed of the rotor.

It is desirable to have large L with large lift-to-drag ratio for extracting greater power from oncoming wind.

Optimization of transonic airfoils for drag reduction is selected for validation study to test the capability of CFD-based tools for shape optimization using genetic algorithms. The optimization goal in this case focuses on drag reduction (especially shock drag reduction) while maintaining lift. The reason for this study is that drag plays a major role in the aircraft performance and therefore the shape optimization of an aircraft at transonic speeds to minimize the shock drag is a topic of great interest in Computational Aerodynamics.

Majority of modern commercial aircrafts operate at transonic cruise speeds. An aircraft in motion at transonic speeds encounters a rapid increase in drag due to the shock waves appearing at various locations on its surface, especially on the wings. These shock waves cause flow instability and increase in drag force which result in higher fuel consumption or reduced energy efficiency. The goal of drag reduction is to eventually design shock-free airfoils with reduced shock drag or even eliminate the shock altogether. However, the drag reduction alone cannot be the optimization target if it adversely affects the lift; in general there is a tradeoff between lift and drag [18]. Several important criteria must be met in the optimization process to achieve not only a shock-free but also an efficient airfoil that has good drag characteristics, a buffet boundary high enough to permit cruising at design lift coefficient, and no unsatisfactory off-design performance etc. [19].

2.3 Blade Element Momentum (BEM) Theory for 3D Wind Turbine Applications

When it comes to the optimization of the performance of a real 3D wind turbine, CFD-based shape optimization is computationally very complex and intensive. Although shape optimization is applied in wind turbine design, it is done mostly for airfoil sections of a blade or in some cases for the entire 3-D blade. Airfoil sections at different positions along the blade usually have varying twist angles, chord lengths, maximum thicknesses, and cambers, etc. Thus the design of

3D blade leads to a large number of design parameters. Furthermore, CFD evaluation of a 3D wind turbine requires much greater computing capability and more challenging meshing etc., which makes the solution process very complex and extremely computationally intensive. In this dissertation therefore we do not consider CFD based design optimization of a real wind turbine.

However, we can still use simpler methods to evaluate and improve the performance of a real wind turbine. One can combine these simpler methods with improved (optimized) blade airfoil sections to design better turbines with greater efficiency.

This study employs the Blade Element Momentum Theory based analysis tools to evaluate the overall power output of an individual wind turbine. The BEM method is known for its simplicity, high computational efficiency and reasonable accuracy when compared to the real test data. This method is only suitable for Horizontal-Axis Wind Turbines. For HAWTs, it is well established that the power output is a function of the number of blades *B*, the tip speed ratio λ (blade tip speed/wind free stream velocity) and the lift to drag ratio (C_l/C_d) of the airfoil sections of the blade. The BEM tool uses this information to evaluate the performance of a HAWT (the power generation).

The Java-based BEM aerodynamic analysis tool used in this study is developed based on Ceyhan's method [20]. The Java programming language is convenient for coding and debugging. The BEM analysis tool is validated against the field test data and Ceyhan's BEM results for three wind turbines: NREL (National Renewable Energy Laboratory, USA) Phase II and Phase III wind turbines and Risoe wind turbine. The NREL Phase II wind turbine has an untwisted and un-tapered blade while the NREL Phase III wind turbine has a twisted and un-tapered blade. The Risoe wind turbine has both twist and taper in the blades. Computations are performed and compared with calculations of Ceyhan [20] and field test data to validate our BEM analysis tool. The results show that the developed BEM tool is accurate and efficient in calculating the wind turbine performance.

The airfoil sections used in the improved wind turbines come from the 2D shape optimization. We consider some commercially popular airfoils for wind-turbine blade sections to improve the wind turbine power generation. The airfoil sections employed in this thesis are thick

airfoils such as the S, DU, FX, Flat-back and NACA 6-series of airfoils. They are used as the baseline airfoils for shape optimization using genetic algorithms [21, 22] because of their aerodynamic and structural advantages [23]. These airfoils vary in (C_l/C_d) for a given B and λ, and therefore the power generated by HAWT for different blade airfoil sections is also different.

After evaluating the effect of different airfoil sections on HAWT performance using the Blade Element Momentum (BEM) theory, we compare their performance with S809 airfoil used in NREL Phase II and III wind turbines; the lift and drag coefficient data for these airfoils sections are available. The output power of the turbine is calculated using these airfoil section blades for a given B and λ and is compared with the original NREL Phase II and Phase III turbines using S809 airfoil section. It is shown that by a suitable choice of airfoil section of HAWT blade, the power generated by the turbine can be significantly increased.

2.4 Wind Farm Layout Optimization

With increased emphasis on wind power generation worldwide, the optimal placement of large number of wind-turbines in a wind farm is currently a problem of great interest. Many wind turbines are installed in large area wind farms because multi-megawatt production requires a large number of wind turbines placed where large wind resources exist. However, the efficiency of a wind farm is greatly influenced by their positioning. This requires systematic analysis and optimization to plan the layout of wind turbines for maximal utilization of wind resources.

The main cause for wind farm inefficiency has been attributed to wake losses due to turbine/wake interference among wind turbines. Wind turbines generate rotating wakes due to the blade rotation which interact with other turbines behind them. The influences of these vortical structures extend to 10 rotor diameters downstream of a wind turbine. Therefore, dense arrangement of wind turbines can result in poor performance of the wind farm in power production as well as increase the maintenance cost due to increase in wear and tear. On the other hand, sparse arrangements can result in inefficient usage of land. Therefore, an optimized arrangement of wind turbines in a wind farm can maximize the wind farm efficiency.

In this dissertation, the goal of wind farm optimization is to optimally position the turbines within the wind farm such that the wake effects are minimized and the power production is maximized. The power-to-cost ratio is used as the objective function for optimization. Both HAWTs and VAWTs are considered. Several reasonably accurate turbine wake models are used to account for the wake effects. Some mathematical models for power output and cost are also employed.

2.5 Genetic Algorithms

Aerodynamic shape optimization has always been a challenging problem because the governing fluid dynamics are nonlinear [24]. Genetic algorithm is a good shape optimization algorithm because it can deal with large number of continuous and integer design variables as it searches highly multimodal and discontinuous design spaces. It can also find the global optimum without requiring an initial design point [25]. Genetic algorithms are also capable of obtaining the best solution to the wind-farm layout optimization due to their unique ability to model the behavior of a wind farm configuration and to find the global optimum.

The goal of this paper is to employ both single- and multi- objective genetic algorithms for shape optimization of wind turbine airfoils, blades and for layout optimization of wind farms.

The commercially available software ANSYS-FLUENT [26] is used for calculation of the flow field using the Reynolds-Averaged Navier-Stokes (RANS) equations in conjunction with either a two-equation or a three-equation turbulence model. Using the CFD software with a genetic algorithm, we obtain globally optimal airfoils for given flow condition.

Chapter 3 Literature Review

3.1 Airfoil and Wind Turbine Optimization

Computational optimization has been applied for decades to systematically solve the aerodynamic design problems. Dating back to the 1970s, Hicks, Murman, and Vanderplaats [27, 28] were among the first who investigated the problem of aerodynamic shape optimizaion. Although encouraging, their results for transonic airfoil optimization showed some quite unexpected results and pointed several difficulties. The main difficulty was in the inadequate number of design parameters, which was due to relatively limited computing power in those days.

With the development of computer speed and memory capacity and especially the advances in parameter gradient calculation methods such as the adjoint method [29] and the Newton-based direct method, the limitation on the number of design parameters is largely reduced. Several contributions have been made during the 1980s describing the optimization strategies for airfoil design. Drela [30] employed a global optimization method embedded with his inverse scheme for airfoil design. Cosentino and Holst [31] employed an efficient three-dimensional full potential flow solver coupled with a modified quasi-Newton unconstrained optimization algorithm to design advanced transonic wing configurations. Jameson [29] proposed the use of control theory for aerodynamic design to achieve an efficient optimization solution.

Wind turbine designers have been constantly seeking a low cost, highly efficient blade design method. In earlier days, the Glauert and Wilson's method was mostly used for blade design [32, 33]. Traditionally, wind turbine blades use general aviation airfoils because they are low speed airfoils and their aerodynamic characteristics have been thoroughly studied in the last few decades.

The current researches on the viability of the wind turbine for power generation have covered the entire design process of wind turbine from the blade to the intricate control systems which allow for optimum performance. Some important work on the wind turbine aerodynamic theory include Betz equation, which shows a mathematical approach for evaluating various parameters involved in the design of the wind turbine [34].

During the recent decade, a number of researchers have focused on the optimization of wind turbines. Fuglsang and others [35] developed optimization methods for wind turbine rotors. Stiesdal [36] developed the wind turbine, components and operation. Hansen [37] worked on aerodynamics of wind turbines. Fuglsang and others [35] developed site-specific design optimization of 1.5-2.0 MW wind turbine. Benini and others [38] developed optimal design of horizontal axis wind turbines using blade-element theory and evolutionary computation. Grauers [39] worked on efficiency of three wind energy generator systems.

Tan [40] compares the effectiveness of an evolutionary algorithm with a swarm algorithm in inverse design, and in single objective and multiple objective airfoil shape optimization problems. He utilizes the PARSEC method for airfoil representation for Mach numbers up to 0.78 and his optimization targets are drag-to-lift ratio minimization while lift is either predefined or set a minimum or left unconstrained. Although Tan finds that both methods are well suited to airfoil shape optimization problems, many airfoil shapes resulting from the unconstrained lift coefficient problem display the unconventional characteristic of having multiple changes in airfoil curvature.

Alpman [41] applied the GA to the airfoil shape optimization problem in incompressible flow with the NACA 4-digit series airfoils. A boundary layer/panel method coupled flow solver is linked to the optimization algorithm within an automated design loop. The optimization objective is the minimization of drag-to-lift coefficient with constraints on lift coefficient, moment coefficient and flow angle of attack. His results showed that differential evolution can be effectively used for airfoil shape optimization. However, the resulting airfoils were very thin and the optimized drag-to-lift ratio appeared to be unrealistically small, of the order of 3e-6.

Burger [42] and Hartfield apply a GA to a wind turbine optimization problem which utilizes a vortex lattice method for predicting wind turbine performance. The optimization is based on NACA 4-digit airfoils shapes. The optimization variables included the maximum camber, position of maximum camber, wind turbine blade length, blade width at the root and tip, blade sweep, and blade angle of attack as a function of radial position. Their work accurately predicted the wind turbine performance under the described constraints and they recommended for future work the inclusion of variable blade sections with differing camber along the rotor span.

Michael [43] carried out an economic optimization analysis of a variable speed, three bladed horizontal-axis wind turbine to show that modern wind turbines have become economically competitive form of clean and renewable power generation source and optimizing wind turbines for specific sites can further increase their economic competitiveness. His work focused on optimizing the blade shape of wind turbines in order to maximize the energy yield of the wind turbine. He presented a design tool for optimizing wind turbine blades using the genetic algorithm code in MATLAB for any type of wind turbine provided that the objective function is the same.

Kenway [44] and Martins investigated the aerostructural shape optimization of wind turbine rotor with respect to site-specific winds. The objective function was to minimize the Cost of Energy (COE). The design variables were chord, twist, spar thickness, spar location, spar length, airfoil thickness, and rotation rate. The baseline airfoil was from NACA 44XX series with the thickness determined by a gradient based method called SNOPT optimization scheme, as opposed to GA, which is based on the sequential quadratic programming approach. XFOIL was used to calculate the aerodynamic coefficients in the attached flow region. Wind turbines with a diameter of 5m were optimized at two different locations, with different average wind velocities. Significant increases in power production at each site were achieved. Smaller, but still significant power increases were obtained when the optimized wind turbines were modeled at the opposite wind site.

Xuan et. al [45] optimized the aerodynamic and aeroacoustic behavior of a 0.5 MW and a 1.5 MW wind turbine using a GA. The rotor was defined by a single airfoil, represented by a

Bezier curve. The aerodynamic coefficients were calculated by XFOIL while the sound pressure levels were determined by NAFNoise. For the 1.5 MW wind turbine, a small reduction in noise generation was achieved with negligible differences in power production. The airfoil shape was only slightly different from the original, possibly due to the erratic point distribution of the Bezier curve control points. Recent research has been conducted by coupling models used for performance prediction with optimization algorithms.

Authors in Ref. [46] used CFD coupled with a design of experiments/response surface method approach, focusing on only symmetric blade profiles in two dimensions using a seven-control-point Bezier curve.

Bourguet [47] simulated only one blade with a low solidity as to avoid undesirable unsteady effects. He found that when there exists a possibility of several local optima, therefore stochastic optimization algorithms are better suited for the job as they tended to be more efficient than gradient-based algorithms.

Research has also led to patented blade designs using CFD coupled with optimization [48]. Other than using optimization techniques, inverse design methods can also be used to find an optimum design for a fixed tip speed ratio that satisfies the specified design performance characteristics. However, inverse design techniques require experience and intuition in order to specify desired performance, whereas optimization allows for designs to be generated that are more often than not beyond the intuition of a designer.

3.2 Optimization Methods

Optimization methods are widely used in the design process of wind turbine blades, airfoils and other system parts. Among the many optimization methods applied to airfoil design and optimization, genetic algorithms have been applied in practice to solve many complex problems due to their ability to avoid the computation of gradients and their advantage in dealing with all of the facets of soft computing, namely robustness, nonlinearity and uncertainty.

Vicini and Quagliarella [46] studied the capabilities of multi-objective genetic algorithms for the aerodynamic design of transonic airfoils. They compared their results with a single point and a multipoint approach and demonstrated the advantages of multi-objective optimization.

Sun [49] investigated the design of a wind turbine airfoil under various operating conditions through the use of a suitable combination of flow analysis and optimization techniques. The incompressible Navier-Stokes equations and the k-ε turbulence model were used to compute the aerodynamic coefficient of an airfoil. The response surface method (RSM) was applied to obtain the optimum solution of the defined objective function and the penalty term of the constraint. The optimized airfoil shapes have good aerodynamic performance according to various operating conditions (such as change in angle of attack), objective functions (minimum of drag coefficient or maximum of lift-to-drag ratio), and constraints (the lift coefficient of a designed airfoil is higher than that of a baseline airfoil at a certain angle of attack).

Lee et al. [50] proposed an approach to design a horizontal-axis wind turbine using two step optimization procedures with probability approach. The probability of success was greatly improved from the initial design space to the final design space.

Casas et al. [51] established an automatic design environment combined with an aerodynamic simulation and used a design optimization process to improve the aerodynamic performance of a wind-turbine blade.

3.3 Wind Farm Optimization

There is limited literature on the optimization of wind farm layouts, probably due to its complexity. The optimization problem exhibits convexity, which cannot be completely described in an analytical form. Besides, the design spaces of some variables have a character of non-allowed values and some others are discrete variables. This makes the problem non-derivable, preventing the use of any of the classic analytical optimization techniques.

Several studies have addressed the problem of optimal placement of horizontal axis wind turbines (HAWT) for maximum power generation capacity [52-54]. These studies employ a

genetic algorithm for determining the optimal placement of turbines to maximize the generated wind power while limiting the number of turbines installed and the acreage of land occupied. The optimal spacing between the turbines in general depends upon the terrain, the wind direction and the speed, and turbine size. The optimization strategy requires the models for the wake and investment cost for the turbines (which depends on the number of turbines and their size). Most of the studies have employed a very simple wake model of Jensen [55, 56] and a simple cost model of Mosetti et al. [52]. There are also some relevant papers on turbine location problems due to location services or undesirable facilities [57-59]

Among the literature on wind farm optimization, Mosetti et al. [52] were the first to propose the mathematical optimization of positioning the wind turbines in wind farms. They introduced a genetic algorithm to maximize the power at minimum cost. Their study was based on the assumption that momentum is conserved inside the wake stream. They also proposed a rather simple wind farm cost model. In 2004, Ozturk and Norman [60] published a paper about wind turbine distribution optimization in a wind farm. They developed a different heuristic method using Jensen's wake decay model and Mosetti's wind farm cost model by evaluating the suppression, translation or addition of turbines until a maximum wind farm profit is achieved. The advantage of this method is that it's useful to readjust the locations of the turbines. The disadvantage is that there is a strong trend to fall into local maxima which requires random perturbations to resume the search.

In 2005, Grady et al [53] revised Mosetti's approach and contributed some algorithm modifications to improve the final wind farm layout. In 2007, Lackner and Elkinton [61] developed a method using the levelized cost of energy as the objective function for offshore wind farm layout optimization problems. The method converts the cost of energy into a function of turbine position only. When combined with wind farm cost estimates, the levelized cost of energy is still only a function of turbine position and can then be used as an objective function within a variety of optimization algorithms.

In 2007, Castro Mora et al. [62] also used a genetic algorithm to maximize an economic function, which is related to turbine parameters and locations. The wind farm is represented with a square grid. One of the shortcomings of their approach was that wake loss was not considered.

In 2009, Wan et al [54] investigated the micro-sitting of wind turbines for wind farm configuration. They used Weibull function to describe the probability of wind speed distribution and employed turbine speed-power curve to estimate turbine power generation. They used a binary-encoded genetic algorithm to search for the minimum of the cost per unit energy of the wind farm. Their results showed better performance and more realistic and effective strategy.

In 2010, Kusiak and Song [63] published their results for design of wind farm layout for maximum wind energy capture. They proposed a model for wind turbine placement based on the wind distribution. The model considers wakes loss, which can be calculated based on wind turbine locations and wind direction. They also transformed the optimization constraints into a second objective function. Using a multi-objective evolutionary strategy algorithm, they achieved the optimal results which maximized the expected energy output as well as minimized the constraint violations.

In 2011, Dabiri et al [64] published his contribution on the potential order-of-magnitude enhancement of wind farm power density via counter-rotating vertical-axis wind turbine arrays. They investigated the use of counter-rotating vertical-axis wind turbines (VAWTs) for higher power output per unit land area than existing wind farm consisting of HAWTs. Their results indicates that the power densities an order of magnitude greater can potentially be achieved by arranging VAWTs in layouts that enables them to extract energy from adjacent wakes and from above the wind farm. The positive aspect of their findings is that this improved performance does not require higher individual wind turbine efficiency, only closer wind turbine spacing and a sufficient vertical flux of turbulence kinetic energy from the atmospheric surface layer.

In 2011, Mittal et al. [65] developed a previous code 'Wind Farm Optimization using a Genetic Algorithm' (referred as WFOG) for optimizing the placement of wind turbines in large wind farms by using a new wake model from Ishihara et al. [66]. The new wake model took into account the effect of atmospheric turbulence and rotor generated turbulence on the wake recovery. Their results showed that Ishihara's wake model estimated the velocity in the wake more accurately than the Jensen's model.

In 2012, Gonzalez [67] proposed a new contribution to optimal wind farm design including the main risk management aspects. Their optimization objective was to optimize the expected profits of the wind farm by taking into account that the wind data used to design the wind farm involves some degree of uncertainty that affects the final return on the project. Net present value (NPV) was used as a figure of profitability in the proposed method. Their method was successfully verified by analyzing a set of test cases with different wind scenarios.

In 2013, Chen et al. [68] published their research focusing on optimizing a wind farm's layout in a two-dimensional area using different hub height wind turbines. Three different wind conditions were analyzed using nested genetic algorithm. Their results showed that the power output of the wind farm using different hub height wind turbines was increased even when the total numbers of wind turbines are same. Different cost models were also taken into account in the analysis, and results showed that different hub height wind turbines could also improve cost per unit power of a wind farm. A large wind farm with commercial wind turbines was analyzed to further examine the benefits of using different hub height wind turbines in more realistic conditions.

3.4 Brief Literature Review of Flatback, DU, FX, NACA 64 Series, RAE 2822 and NACA 0012 Airfoils

3.4.1 Flatback Airfoils

In recent years, there has been sufficient interest on the design optimization of flatback airfoils because they have been proposed for the inboard regions of large wind-turbine blades. They provide several structural and aerodynamic performance advantages [69-71]. The structural advantage of flatback is due to increase in the sectional area and sectional moment of inertia for a given airfoil of maximum thickness.

The aerodynamic advantage of the flatback airfoil is due to increase in sectional maximum lift coefficient and lift curve slope; it reduces the well-known sensitivity of the lift characteristics of thick airfoils to surface soiling [70-72]. One example of the improvement of aerodynamic characteristics is shown by the pressure distributions of TR-35 and TR-35-10 airfoils in Figure 3.1 [70]. Incorporation of trailing edge thickness allows for a portion of the pressure recovery to occur in the airfoil wake, thereby reducing the severity of adverse pressure gradient on the suction surface. This reduction in adverse pressure gradient on the suction surface alleviates the tendency toward premature boundary layer separation for both clean and soiled conditions and improves lift performance [73]. The disadvantages of the flatback airfoils are increased drag and greater aero-acoustics emissions.

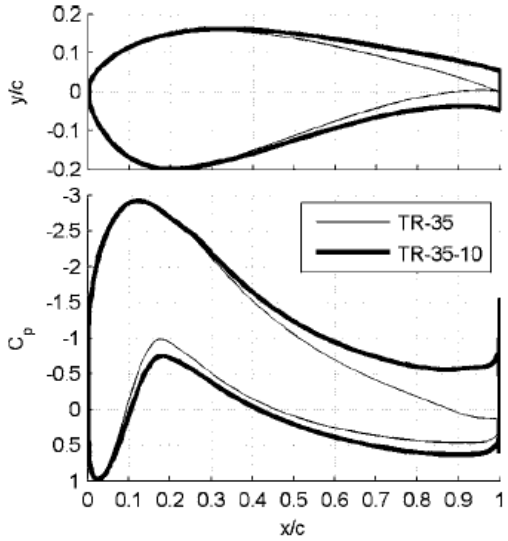

Figure 3-1 Time-averaged pressure distributions of the TR-35 and TR-35-10 airfoils at Re=4.5x10^6, α=8 deg, free transition [73]

3.4.2 FX, DU and NACA 64 Series of Airfoils

In last several decades, many remarkable contributions have been made to provide wind turbine manufacturers with superior airfoil families such as FX, DU and NACA 64 series of airfoils that fulfill the intrinsic requirements in terms of design point performance, off-design capabilities and structural properties [23].

The FX airfoils were designed by Professor F.X. Wortmann of the University of Stuttgart. Most of the FX airfoils are characterized by a wide low drag range together with a high maximum lift coefficient corresponding to the requirements of sailplane design [74]. The DU airfoils were designed at the Delft University of Technology. They were designed as alternatives to the thick members of the NACA family of airfoils which suffer from severe degradation in performance due to premature flow transition [75]. The NACA 63 and 64 six-digit series airfoils are another kind of airfoils still being used in wind turbine blades today. These airfoils are optimized for high speed wind condition with an advantage of high maximum lift coefficient and very low drag over a small range of operating conditions [76, 77].

The FX, DU and NACA 64 series airfoils all have an upper surface contoured so as to increase the flow velocity to avoid separation for the desired incidence angle range. The lower surface is contoured so as to maintain the desired thickness (dictated typically by considerations of strength). In these airfoils, the S shaped transition towards the trailing edge increases the lift [72].

Chapter 4 Methodology

4.1 Overview

This dissertation is dedicated to developing the optimization systems in the mechanical design fields. Contributions are made especially to the wind energy industry, including wind turbine blade optimization and wind farm optimization. The optimization systems are constructed based on evolutionary algorithms. Both single- and multi- objective genetic algorithms are employed.

The optimization systems employed in this dissertation have successfully integrated the optimization algorithms with both numerical and analytical simulation methodologies, which are capable of evaluating the objectives of each individual design candidate generated during the optimization. Figure 4-1 shows a schematic of the design systems. It illustrates how the optimization algorithms interface with the external simulation methods.

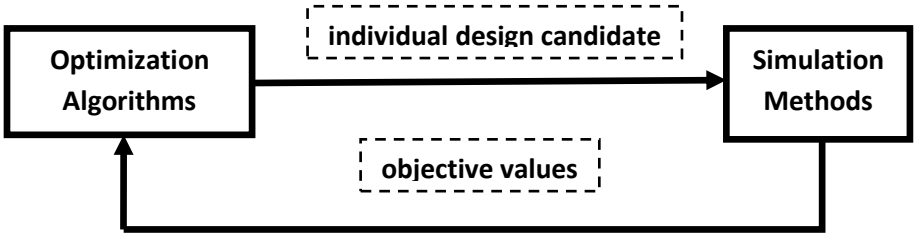

Figure 4-1 Illustration of information flow in optimization process

For the shape optimization problems of wind turbine airfoils/blades, an individual is represented by an airfoil geometry data file, which is passed on to the pre-processing program *Gambit* [78]. Gambit is used to create the geometry of the airfoil and mesh; it creates a two-dimensional structured or unstructured mesh which is then passed on as input to the CFD flow solver FLUENT for computation of the flow field. FLUENT is used to solve for the coefficient of lift C_l and the coefficient of drag C_d. Some combination of these values (either C_l and/or C_l/C_d) are taken as the quantities of interest (single or multiple objective values) to determine the fitness

of the airfoil. The algorithm shown in Figure 4-2 continues until the convergence in the objective values is achieved.

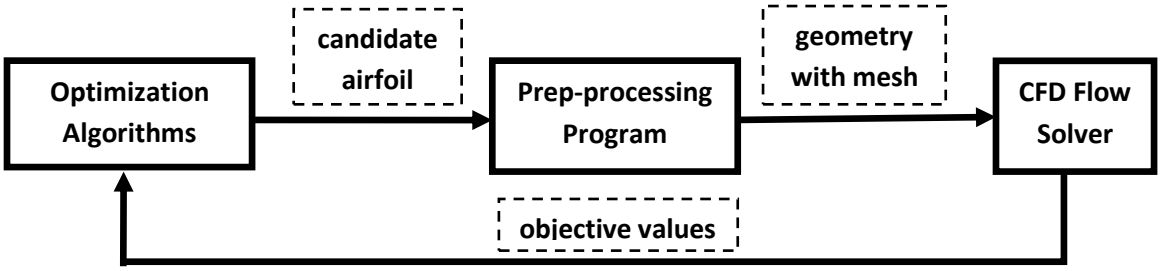

Figure 4-2 Illustration of information flow in optimization process

For wind farm layout optimization problems, individuals are represented by arrays or vectors which store the information of wind turbine distributions for one wind farm layout. This information is passed on to the Power Evaluation Program coded by JAVA programming language. The Power Evaluation Program extracts the location information of wind turbines, determines the wake effects between them based on several wake models, and calculates the power output for each wind turbine using some aerodynamic model. The total power output of all wind turbines is taken as the objective value which determines the fitness of the wind farm layout. The algorithm shown in Figure 4-3 continues until the convergence in the objective value is achieved.

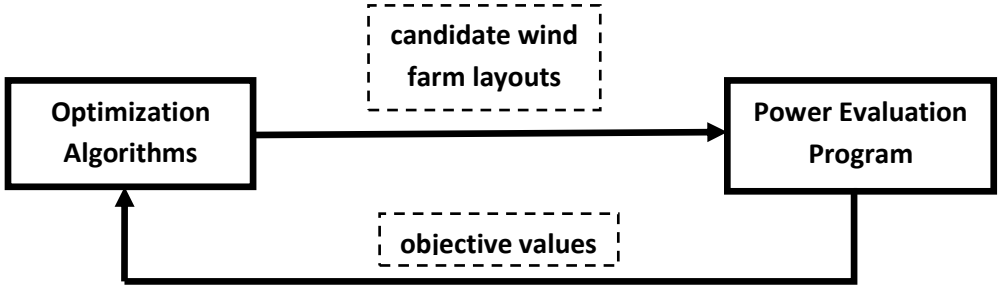

Figure 4-3 Illustration of information flow in optimization process

4.2 Genetic Algorithm

In this section, the genetic algorithm concepts employed in this work are described. The discussion starts from the Single-Objective Genetic Algorithm optimization technique, followed by the introduction of Multi-Objective Genetic Algorithm.

4.2.1 Single-Objective Genetic Algorithm (SOGA)

Genetic algorithms are a class of stochastic optimization algorithms inspired by the biological evolution. SOGA is the most commonly applied GA. In SOGA, a set or generation of input vectors, called individuals, is iterated over, successively combining traits (aspects) of the best individuals until a convergence is achieved. In general, GA employs the following steps [79].

1. **Initialization**: Randomly create *k* individuals. Each individual (*x*) is chromosome with *n* alleles as illustrated in Figure 4-4. Each individual (*x*) mimics one single creature in a biological group as shown in Figure 4-5.

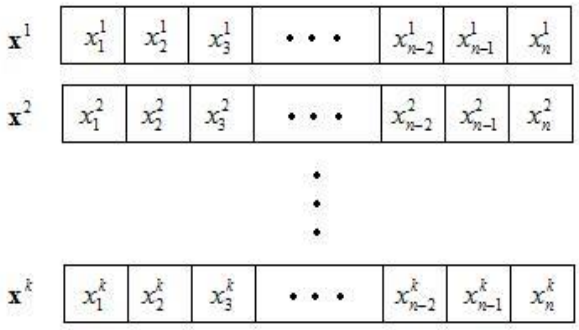

Figure 4-4 Illustration of *k* individuals in the initial generation

Figure 4-5 Biological individual from a biological generation

2. **Evaluation**: Evaluate the fitness of each individual.

3. **Natural selection**: Sort individuals in order of decreasing fitness and remove a subset of the individuals. Often the individuals that have the lowest fitness are removed; although culling, the removing of those individuals with similar fitness, is sometimes performed. This step mimics the natural selection process in the biological world shown in Figure 4-6. The left individuals are called survivors and will go to the next steps.

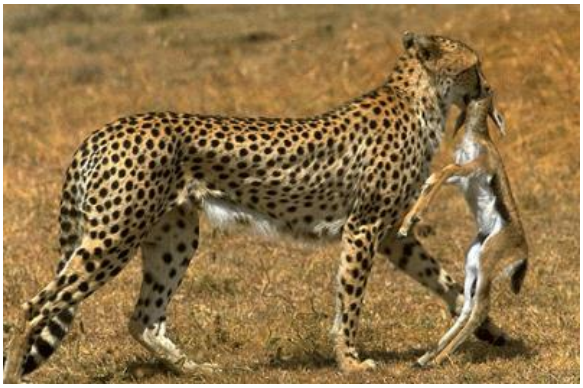

Figure 4-6 An example of natural selection in the biological world

4. **Reproduction**: Pick pairs of individuals from the survivors from the last step as parents to produce an offspring. This is often done by roulette wheel sampling; that is, the probability of selecting some individual h_i for reproduction is given by:

$$P[h_i] = \frac{fitness(h_i)}{\sum_j fitness(h_j)} \tag{4-1}$$

A *crossover* function is then performed to produce the offspring. Generally, crossover is implemented by choosing a crossover point on each individual and swapping *alleles* – or vector elements – at this point as illustrated in Figure 4-7. This procedure stops when the total number of survivors and offspring equals the number of individuals of the initial generation (*k*).

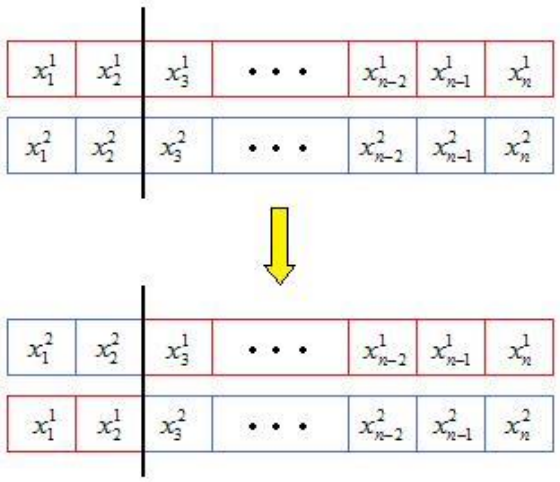

Figure 4-7 Illustration of the General Crossover Function in GA

4. Mutation: Randomly alter some small percentage of the population. This is analogous to biological mutation. The purpose is to maintain genetic diversity and prevent local optima.

5. Check for Convergence: If the solution has converged, return the best individual observed. If the solution has not yet converged, label the new generation as the current generation and go to step 2. Convergence is often defined by a certain number of generations or a similarity threshold.

4.2.2 Multi-Objective Genetic Algorithm (MOGA)

For many design problems, it is desirable to achieve, if possible, simultaneous optimization of multiple objectives [80]. These objectives, however, are usually conflicting, preventing simultaneous optimization of each objective [81]. Therefore, instead of searching for a single optimal solution, a multi-objective genetic algorithm is necessary to find a set of optimal solutions (generally known as *Pareto-optimal solutions*). In this dissertation, the MOGA algorithms used to find the *Pareto-optimal solutions* to the airfoil optimization problem in this study is widely known as Nondominated Sorting Genetic Algorithm II (NSGA-II) [82].

In NSGA-II, a Pareto-optimal solution set is defined as the one such that any individual inside the set dominates any individual outside the set while any individual in the set is not dominated by another individual in this solution set. Here, a feasible solution **x** is said to dominate another feasible solution **y,** if and only if, all the objectives of **x** are not worse than those of **y** and at least one objective of **x** is better than that of **y**. A solution is said to be *Pareto optimal* if it is not dominated by any other solution in the solution space [81].

The NSGA-II algorithm is employed in this study due to the following three features: (1) it uses an elitist principle, (2) it uses an explicit diversity preserving mechanism, and (3) it emphasizes non-dominated solutions in a population [83]. The implementation procedure of NSGA-II is as follows [82]:

1) At ***0*-th generation**, a random parent population P_0 of size N is created; it is sorted based on the non-domination. Then the individuals in P_0 are ranked: 1 is the best level, 2 is the next-best level, and so on. Then P_0 is sent to selection, recombination, and mutation operators to create offspring population Q_0 of size N.

2) At ***t*- th generation**, a combined population $R_t = P_t \cup Q_t$ of size 2N is formed and is sorted according to non-domination. Then individuals in R_t are divided into the best non-dominated set F_1, the next-best non-dominated set F_2 and so on. If the size of F_1 is smaller than N, all members of F_1 go to P_{t+1}, with the remaining members chosen from F_2, F_3 ... until the size of P_{t+1} is N. Then new population P_{t+1} are sent to selection, crossover, and mutation operators to create a new population Q_{t+1} of size N.

3) **Termination:** the procedure terminates when convergence criterion is met.

This study utilizes a Java code package called jMetal. It is a Java-based framework for multi-objective optimization using meta-heuristics. It is easy-to-use and is flexible and extensible [84].

4.3 Computational Fluid Dynamics

4.3.1 Overview

All the wind turbine airfoils/blades optimization problems in this dissertation employ Computational Fluid Dynamics (CFD) methodology to compute the flow field. CFD is a branch of fluid mechanics that uses numerical methods and algorithms to solve the governing equations of fluid dynamics.

The continuity equation and the Navier-Stokes equations are the fundamental equations solved by the CFD technology. Given the complexity and nonlinearity of the Navier-Stokes equations, they are often simplified by invoking several assumptions. The equations are simplified by assuming the fluid to be inviscid and therefore deleting the viscous terms to yield the Euler equations. By making addition assumption that the fluid flow is irrotational, one obtains the full potential equation. Finally, for small perturbations in subsonic and supersonic flows (not transonic or hypersonic) the full potential equation can be linearized to yield the linearized potential equation. Most well-known CFD codes developed during last thirty years are FLUENT, ARC3D, OVERFLOW, CFL3D, etc.

The basic procedure employed in obtaining the CFD solution is as follows:

(1) Pre-processing:

(a) The geometry of the problem is defined in discretized form.

(b) The volume occupied by the fluid inside a computational domain is divided into discrete cells called the mesh. The mesh may be uniform or non uniform and can have a variety of types of elements (structural, unstructural, hybrid, etc.), and a variety of topologies (O-type, C-type, H-type or hybrid)

(c) Boundary conditions are defined. This involves specifying the fluid behavior and properties at all the boundaries of the computational domain including the object under consideration. For transient problems, the initial conditions are also defined.

(2) Flow field simulation: The governing equations are discretized at mesh points generated in step (1) and are solved using an appropriate algorithm on a computer to obtain the values of the flow variables at mesh points

(3) Post-processor: Post-processing software is used for analysis and visualization of the resulting solution.

4.3.2 Governing Equations

The governing equations of fluid flow are partial differential equations that describe the conservation of mass, momentum and energy. These equations can be written as:

Continuity equation:

$$\frac{\partial \rho}{\partial t} + \frac{\partial}{\partial x_i}(\rho u_i) = 0 \tag{4-2}$$

Momentum equation:

$$\frac{\partial}{\partial t}(\rho u_i) + \frac{\partial}{\partial x_j}\left(\rho u_i u_j\right) = -\frac{\partial p}{\partial x_i} + \frac{\partial \tau_{ij}}{\partial x_j} \tag{4-3}$$

Energy equation:

$$\frac{\partial}{\partial t}\left[\rho\left(h + \frac{1}{2}u_i^2\right)\right] + \frac{\partial}{\partial x_j}\left[\rho u_j\left(h + \frac{1}{2}u_i^2\right)\right] = \frac{\partial p}{\partial t} + \frac{\partial}{\partial x_j}\left(u_i \tau_{ij} + \lambda \frac{\partial T}{\partial x_j}\right) \tag{4-4}$$

where the stress tensor τ_{ij} and enthalpy h are expressed in the following manner:

$$\tau_{ij} = \mu\left(\frac{\partial u_i}{\partial x_j} + \frac{\partial u_j}{\partial x_i}\right) - \frac{2}{3}\mu\frac{\partial u_i}{\partial x_i}\delta_{ij} \tag{4-5}$$

$$h = c_p T \tag{4-6}$$

The governing equations are a coupled system of non-linear partial differential equations containing five equations for six unknown flow-field variables, u, v, w, p, ρ and T. In aerodynamics, it is generally reasonable to assume that the gas is a perfect gas. For a perfect gas, the equation of state

$$p = \rho RT \tag{4-7}$$

gives the sixth equation.

In equation (4-7), *R* is the gas constant.

4.3.3 Turbulence

Most of the flows in nature and in industrial systems can be considered as turbulent flows. Turbulence describes the random and chaotic motion of viscous fluid flow. Turbulent flows are characterized by fluctuating velocity, pressure and temperature fields. These fluctuations result in fluctuation of transport quantities namely the momentum, energy, and species concentration.

Since these fluctuations are of small scale and high frequency, they are computationally too difficult and expensive to simulate directly in practical engineering applications. Therefore, the instantaneous (exact) governing equations are generally time-averaged, ensemble-averaged, or otherwise manipulated to remove the resolution of small scales, thereby resulting in a modified set of equations that are computationally less intensive to solve. However, the modified equations contain additional unknown variables which need to be modeled. Therefore turbulence models are needed to determine these variables in terms of known quantities [85].

The turbulence modes can be classified into the following categories:

(1) Reynolds-Averaged Navier-Stokes (RANS) equations-based models

(a) Linear eddy-viscosity models
    i. Algebraic models
    ii. One and two equation models
(b) Non-linear eddy viscosity models and algebraic stress models
(c) Reynolds stress transport models

(2) Large eddy simulation (LES)
(3) Detached eddy simulation (DES) and other hybrid models
(4) Direct numerical simulation (DNS)

The RANS-based modeling approach employs RANS equations in conjunction with a turbulence model for the unknown "Reynolds Stress". The RANS equations govern the transport of the averaged flow quantities, thus greatly reducing the computational effort. They are widely adopted for practical engineering applications.

An alternative approach, the LES computes the large eddies explicitly in a time-dependent simulation using the "filtered" Navier-Stokes equations. Filtering is required to manipulate the exact Navier-Stokes equations so that the eddies smaller than the filter size, which is usually chosen as the mesh size, are removed. Like Reynolds-averaging, the filtering process creates additional unknown terms that must be modeled to achieve closure. Smagorinsky model is generally employed to model the small scale eddies.

4.3.4 Turbulence Modeling for RANS Equations

All calculations presented in this dissertation employ Reynolds-average Navier-Stokes equations (RANS) equations as the governing turbulent fluid flow equations.

In Reynolds-averaging, the flow variables in the unsteady Navier-Stokes equations are decomposed into the mean and fluctuating components. That is to say, $u_i = \overline{u_i} + u_i^{'}$, there $\overline{u_i}$ is the mean component and $u_i^{'}$ is the fluctuating component. Similarly, $\phi = \bar{\phi} + \phi'$ for pressure and other scalar quantities. Substituting for flow variables in the governing equations and averaging the equations over a time-period, the time (or ensemble) average equations are

obtained. Dropping the overbar on the mean variables, the time-averaged RANS equations are obtained as:

$$\frac{\partial \rho}{\partial t} + \frac{\partial}{\partial x_i}(\rho u_i) = 0 \tag{4-8}$$

$$\frac{\partial}{\partial t}(\rho u_i) + \frac{\partial}{\partial x_j}\left(\rho u_i u_j\right) = -\frac{\partial p}{\partial x_i} + \frac{\partial}{\partial x_j}\left[\mu\left(\frac{\partial u_i}{\partial x_j} + \frac{\partial u_j}{\partial x_i} - \frac{2}{3}\delta_{ij}\frac{\partial u_l}{\partial x_l}\right)\right] + \frac{\partial}{\partial x_j}(-\rho\overline{u_i' u_j'}) \tag{4-9}$$

$$\frac{\partial}{\partial t}(\bar{\rho}\widetilde{H}) + \frac{\partial}{\partial x_j}(\rho u_j H) = \frac{\partial p}{\partial t} + \frac{\partial}{\partial x_j}\left[(\lambda + \frac{\mu_t c_p}{\sigma_T})\frac{\partial T}{\partial x_j} - u_i(\tau_{ij} - \rho\overline{u_i' u_j'})\right] \tag{4-10}$$

where

$$H = h + \frac{1}{2}u_i^2 \tag{4-11}$$

The RANS equations have the same general form as the unsteady Navier-Stokes equations. The velocities and other flow variables represent the ensemble-averaged (or time-averaged) values. In equations (4-9) and (4-10), an additional term $-\rho\overline{u_i' u_j'}$ called the "Reynolds Stress" appears which needs to be modeled for a given flow. The models that are used to model the "Reynolds Stress" term are called the "Turbulence Models". Using the Boussiness hypothesis, the Reynolds stresses are modeled in the following manner:

$$-\rho\overline{u_i' u_j'} = \mu_t\left(\frac{\partial u_i}{\partial x_j} + \frac{\partial u_j}{\partial x_i}\right) - \frac{2}{3}\left(\rho k + \frac{\partial u_l}{\partial x_l}\right)\delta_{ij} \tag{4-12}$$

In equation (4-12), the eddy viscosity μ_t appears which is obtained by using a turbulence model. For more than a century, a large number of turbulence models have been developed, some of the most widely used are described in the next section.

4.3.5 Turbulence Models

Several commonly used turbulence models used in this dissertation are described below.

(a) Spalart-Allmaras Model

The Spalart-Allmaras model is a simple one-equation model. It solves a transport equation for the kinematic eddy (turbulent) viscosity. It was specifically designed for aerospace applications

involving wall-bounded flows and has been shown give good results for boundary layers subjected to adverse pressure gradients [85].

In Spalart-Allmaras model, the turbulent viscosity μ_t is computed from

$$\mu_t = \rho\tilde{\nu} f_{v1} \tag{4-13}$$

where $\tilde{\nu}$ is identical to the turbulent kinematic viscosity except in the near-wall region (dominated by viscous effects), f_{v1} is viscous damping function given by $f_{v1} = \frac{\chi^3}{\chi^3 + C_{v1}^3}$ and $\chi = \frac{\tilde{\nu}}{\nu}$.

The transport equation for $\tilde{\nu}$ is given by:

$$\frac{\partial}{\partial t}(\rho\tilde{\nu}) + \frac{\partial}{\partial x_i}(\rho\tilde{\nu}u_i) = G_\nu + \frac{1}{\sigma_{\tilde{\nu}}}\left[\frac{\partial}{\partial x_j}\left\{(\mu + \rho\tilde{\nu})\frac{\partial\tilde{\nu}}{\partial x_j}\right\} + C_{b2}\rho\left(\frac{\partial\tilde{\nu}}{\partial x_j}\right)^2\right] - Y_\nu + S_{\tilde{\nu}} \tag{4-14}$$

where G_ν is the production of turbulent viscosity and Y_ν is the destruction of turbulent viscosity that occurs in the near-wall region due to wall blocking and viscous damping. $\sigma_{\tilde{\nu}}$ and C_{b2} are constants and ν is the molecular kinematic viscosity. $S_{\tilde{\nu}}$ is a user-defined source term. The turbulent kinetic energy k is not calculated and the last term in equation (4-12) is ignored when estimating the Reynolds stresses.

The following wall boundary conditions are used with Spalart-Allmaras model:

At walls, the modified turbulent kinematic viscosity $\tilde{\nu}$ is zero. If the mesh is fine enough to resolve the viscous sub-layer, the wall shear stress is calculated using the laminar stress-strain relationship:

$$\frac{u}{u_\tau} = \frac{\rho u_\tau y}{\mu} \tag{4-15}$$

If the mesh is too coarse and the viscous sub-layer cannot be resolved, it is assumed that the centroid of the wall-adjacent cell falls within the logarithmic region of the boundary layer, and the law-of-the-wall is employed:

$$\frac{u}{u_\tau} = \frac{1}{\kappa} lnE\left(\frac{\rho u_\tau y}{\mu}\right) \tag{4-16}$$

where u is the velocity parallel to the wall, u_τ is the shear velocity, y is the distance from the wall, κ is the von Karman constant (0.4187), and E is 9.793.

(b) Shear-stress Transport (SST) k-ω Model

For separated and transitional flows, we employ both the shear-stress transport (SST) k-ω model and the transitional k-kl-ω model. They both have advantages and disadvantages. Developed by Menter [85], the SST k-ω model is more accurate and reliable for a wider class of flows (e.g., adverse pressure gradient flows, transonic flows etc.) than the standard k-ω model.

The SST k-ω model effectively blends the robust and accurate formulation of k-ω model in the near-wall region with the k-ε model away from the wall region. To achieve this, the standard k-ω model and the k-ε model are both multiplied by a blending function and both models are then added together. The blending function is used to activate the standard k-ω model in the near-wall region and the k-ε model away from the surface.

The SST k-ω model consists of the following two transport equations for the turbulent kinetic energy (k) and the specific dissipation rate (ω).

$$\frac{\partial}{\partial t}(\rho k) + \frac{\partial}{\partial x_i}(\rho k u_i) = \frac{\partial}{\partial x_j}\left(\Gamma_k \frac{\partial k}{\partial x_j}\right) + \tilde{G}_k - Y_k + S_k \tag{4-17}$$

$$\frac{\partial}{\partial t}(\rho \omega) + \frac{\partial}{\partial x_i}(\rho \omega u_i) = \frac{\partial}{\partial x_j}\left(\Gamma_\omega \frac{\partial \omega}{\partial x_j}\right) + G_\omega - Y_\omega + D_\omega + S_\omega \tag{4-18}$$

where $\tilde{G}_k$ represents the generation of turbulent kinetic energy due to mean velocity gradients. G_ω represents the generation of ω. Γ_k and Γ_ω represent the effective diffusivity of k and ω. Y_k and Y_ω represent the dissipation of k and ω due to turbulence. D_ω represents the cross-diffusion term. S_k and S_ω are user-defined source terms.

The effective diffusivities are given by:

$$\Gamma_k = \mu + \frac{\mu_t}{\sigma_k} \tag{4-19}$$

$$\Gamma_\omega = \mu + \frac{\mu_t}{\sigma_\omega} \tag{4-20}$$

where σ_k and σ_ω are the turbulent Prandtl numbers for k and ω respectively. The turbulent viscosity μ_t is computed as follows:

$$\mu_t = \frac{\rho k}{\omega} \frac{1}{\max[\frac{1}{\alpha^*}, \frac{SF_2}{a_1 \omega}]} \tag{4-21}$$

where *S* is the strain rate magnitude and

$$\sigma_k = \frac{1}{F_1/\sigma_{k,1} + (1-F_1)/\sigma_{k,2}} \tag{4-22}$$

$$\sigma_\omega = \frac{1}{F_1/\sigma_{\omega,1} + (1-F_1)/\sigma_{\omega,2}} \tag{4-23}$$

α^* damps the turbulent viscosity causing a low-Reynolds-number correction. It's defined by:

$$\alpha^* = \alpha^*_\infty \left(\frac{\alpha^*_0 + Re_t/R_k}{1 + Re_t/R_k} \right) \tag{4-24}$$

where

$$Re_t = \frac{\rho k}{\mu \omega} \tag{4-25}$$

$$R_k = 6 \tag{4-26}$$

$$\alpha^*_0 = \frac{\beta_i}{3} \tag{4-27}$$

$$\beta_i = 0.072 \tag{4-28}$$

In the high-Reynolds-number form, $\alpha^* = \alpha^*_\infty = 1$. The blending function functions F_1 and F_2 are given by

$$F_1 = \tanh(\Phi_1^4) \tag{4-29}$$

$$\Phi_1 = \min\left[\max\left(\frac{\sqrt{k}}{0.09\omega y}, \frac{500\mu}{\rho y^2 \omega} \right), \frac{4\rho k}{\sigma_{\omega,2} D^+_\omega y^2} \right] \tag{4-30}$$

$$D^+_\omega = \max[2\rho \frac{1}{\sigma_{\omega,2}} \frac{1}{\omega} \frac{\partial k}{\partial x_j} \frac{\partial \omega}{\partial x_j}, 10^{-10}] \tag{4-31}$$

$$F_2 = \tanh(\Phi_2^2) \tag{4-32}$$

$$\Phi_2 = \max\left[2 \frac{\sqrt{k}}{0.09\omega y}, \frac{500\mu}{\rho y^2 \omega} \right] \tag{4-33}$$

where *y* is the distance next to the surface and D^+_ω is the positive portion of the cross-diffusion term.

(c) The k-kl-ω Transition Model

The k-kl-ω transition model is used to predict the onset transition in boundary layer flow. This model can be used effectively to predict the transition of boundary layer flow from laminar to turbulent regime. It is a three-equation eddy-viscosity type turbulence model. The three transport equations for turbulent kinetic energy (k_T), laminar kinetic energy (k_L) and inverse turbulence time scale (ω) are as follows:

$$\frac{Dk_T}{Dt} = P_{k_T} + R + R_{NAT} - \omega k_T - D_T + \frac{\partial}{\partial x_j}\left[(\nu + \frac{\alpha_T}{\alpha_k})\frac{\partial k_T}{\partial x_j}\right] \tag{4-34}$$

$$\frac{Dk_L}{Dt} = P_{k_L} - R - R_{NAT} - D_L + \frac{\partial}{\partial x_j}\left[\nu\frac{\partial k_L}{\partial x_j}\right] \tag{4-35}$$

$$\frac{D\omega}{Dt} = C_{\omega 1}\frac{\omega}{k_T}P_{k_T} + \left(\frac{C_{\omega R}}{f_W} - 1\right)\frac{\omega}{k_T}(R + R_{NAT}) - C_{\omega 2}\omega^2 + C_{\omega 3}f_\omega \alpha_T f_W^2 \frac{\sqrt{k_T}}{d^3} + \frac{\partial}{\partial x_j}\left[(\nu + \frac{\alpha_T}{\alpha_\omega})\frac{\partial \omega}{\partial x_j}\right] \tag{4-36}$$

The turbulent and laminar fluctuations are included in the momentum and energy equations via the eddy viscosity and total thermal diffusivity:

$$\overline{-u_\iota u_j} = \nu_{TOT}\left(\frac{\partial U_i}{\partial x_j} + \frac{\partial U_j}{\partial x_i}\right) - \frac{2}{3}k_{TOT}\delta_{ij} \tag{4-37}$$

$$\overline{-u_\iota \theta} = \alpha_{\theta,TOT}\frac{\partial \theta}{\partial x_i} \tag{4-38}$$

The effective length is defined as

$$\lambda_{eff} = MIN(C_\lambda d, \lambda_T) \tag{4-39}$$

where λ_T is the turbulent length scale and is defined by

$$\lambda_T = \frac{\sqrt{k}}{\omega} \tag{4-40}$$

and the small scale energy is defined by

$$k_{T,s} = f_{ss} f_W k_T \tag{4-41}$$

$$f_W = \frac{\lambda_{eff}}{\lambda_T} \tag{4-42}$$

$$f_{ss} = \exp\left[-(\frac{C_{ss}\nu\Omega}{k_T})^2\right] \tag{4-43}$$

The large scale energy is given by

$$k_{T,l} = k_T - k_{T,s} \tag{4-44}$$

The turbulence production term generated by turbulent fluctuations is given by:

$$P_{k_T} = \nu_{T,S} S^2 \tag{4-45}$$

where $\nu_{T,S}$ is the small-scale turbulent viscosity:

$$\nu_{T,S} = f_\nu f_{INT} C_\mu \sqrt{k_{T,s}} \lambda_{eff} \tag{4-46}$$

and

$$C_\mu = \frac{1}{A_0 + A_s(S/\omega)} \tag{4-47}$$

$$f_\nu = 1 - \exp(-\frac{\sqrt{Re_{T,S}}}{A_\nu}) \tag{4-48}$$

A damping function defining the turbulent production due to intermittency is given by

$$f_{INT} = MIN(\frac{k_L}{C_{INT} k_{TOT}}, 1) \tag{4-49}$$

$$Re_{T,S} = \frac{f_W^2 k_T}{\nu_\omega} \tag{4-50}$$

P_{k_L} is the production of laminar kinetic energy by large scale turbulent fluctuations:

$$P_{k_L} = \nu_{T,l} S^2 \tag{4-51}$$

The large-scale turbulent viscosity $\nu_{T,l}$ is modeled as:

$$\nu_{T,l} = MIN\left\{\nu_{T,l}^*, \frac{0.5(k_L + k_{T,l})}{S}\right\} \tag{4-52}$$

where

$$\nu_{T,l}^* = f_{\tau,1} C_{11} \left(\frac{\Omega \lambda_{eff}^2}{\nu}\right) \sqrt{f_{T,1}} \lambda_{eff} + \beta_{TS} C_{12} \phi_{NAT} d_\Omega^2 \tag{4-53}$$

4.3.6 Boundary Conditions and Initial Conditions

The governing equations can only be solved into unique solutions when the boundary conditions and initial conditions are assigned. Since the CFD application in this dissertation is the aerodynamic evaluation for airfoils, the domain of the flow field is such that the airfoils are

located in the center area of the flow field and the domain size is usually 15 to 50 times the length of the airfoil chord. On the airfoil surface, no-slip stationary wall boundary condition is used. For subsonic flow, at the far-field boundaries the velocity inlet boundary condition and the pressure outlet boundary condition are employed upstream and downstream of the airfoil respectively. For transonic flow where Mach number is close to 1, the pressure far-field boundary condition is used.

(a) Boundary Conditions:

(i) Velocity Inlet Boundary Condition:

Velocity inlet boundary condition defines the flow entering the computational domain. Once the inlet flow conditions are assigned, the inlet mass flow rate, momentum fluxes and fluxes of energy and chemical species are computed.

The mass flow rate entering a fluid cell adjacent to a velocity inlet boundary is computed by the relation:

$$\dot{m} = \int \rho \vec{v} \cdot d\vec{A} \tag{4-54}$$

The density is either constant or calculated as a function of temperature and pressure.

(ii) Pressure outlet boundary condition:

For subsonic flow, pressure outlet boundary condition uses a specified static pressure P_s at the outlet boundary and extrapolates all other conditions from the interior of the domain.

(iii) Pressure far-field boundary condition:

Pressure far-field boundary condition is used to model a free-stream condition at infinity with a specified free-stream Mach number. It is based on the introduction of Riemann invariants for a one-dimensional flow normal to the boundary. Two Riemann invariants are used in subsonic flow cases, each corresponds to an incoming and an outgoing wave:

$$R_\infty = v_{n_\infty} - \frac{2c_\infty}{\gamma - 1} \tag{4-55}$$

$$R_i = v_{n_i} + \frac{2c_i}{\gamma - 1} \tag{4-56}$$

where v_n is the velocity magnitude normal to the boundary, c is the local speed of sound and γ is ratio of specific heats . The subscript ∞ refers to conditions at infinity (actually at the far-field boundary), the subscript i refers to conditions in the interior of the domain. These two invariants can be used to calculated v_n and c:

$$v_n = \frac{1}{2}(R_i + R_\infty) \tag{4-57}$$

$$c = \frac{\gamma-1}{4}(R_i - R_\infty) \tag{4-58}$$

where v_n and c are the values of normal velocity and sound speed at the boundary. At a face through which flow exits, the tangential velocity components and entropy are extrapolated from the interior; at an inflow face, these are specified as having free-stream values. Using the values for v_n, c, tangential velocity components, and entropy, the values of density, velocity, temperature, and pressure at the boundary face can be calculated.

To more accurately approximate the true mathematical condition of "infinity", the far-field boundaries should be placed far enough from the object.

(iv) Wall boundary conditions:

The no-slip boundary condition in viscous flows is enforced at the walls. The shear stress at the wall is predicted using the properties of the flow adjacent to the wall/fluid boundary. For turbulent flows, the approaches for near-wall treatment described in "Turbulence Modeling" section are used for calculation of shear stress.

(b) Initial Conditions:

All the computation reported in this dissertation are for steady-state flows, the far-field conditions are applied to the whole flow field as initial conditions.

4.3.7 Discretization Methods

The governing equations together with boundary and initial conditions are sufficient to obtain a unique solution to the flow field problem. However, the governing equations are partial

differential equations with strong non-linearity. They cannot be solved analytically except for some trivial cases. CFD is used to solve the equations in discretized form on a computer

The approach is to discretize the PDEs into algebraic equations and use suitable iterative numerical methods on a mesh to calculate the solution of the algebraic equations for flow variables. The choice of a suitable numerical algorithm depends on the nature of the governing equation - whether it is hyperbolic, elliptic or parabolic.

In addition, the discretization methods can be classified as finite volume method (FEM), finite element method (FEM), finite difference method (FDM), spectral element method, boundary element method, etc. In our study, we employ the finite-volume method.

The finite volume method (FVM) is the mostly used approach in majority of CFD codes. It is good at handling issues of memory usage and solution speed, especially for large problems involving high Reynolds number turbulent flows, or source term dominated flows (like in combustion). In the FVM method, the governing partial differential equations - the Navier-Stokes equations, the mass and energy conservation equations, and the turbulence model equations are recast in a conservation form shown in Equation 4-59. Then they are solved over discrete control volumes (meshes). This guarantees the conservation of fluxes in every cell (control volume). Thus, every equation for a control volume can be written as:

$$\frac{\partial}{\partial t}\iiint Q dV + \iint F dA = 0 \tag{4-59}$$

where Q is the vector of conserved variables, F is the flux vector, dV is the volume of the cell, dA is the surface area of the cell.

4.3.8 Type of Flow Solvers

In this dissertation, we employ both the pressure-based solver and the density-based depending upon the nature of the flow – whether it is incompressible or compressible. Since most flow computed in this dissertation can be considered as incompressible e.g. at low speed, the pressure-based approach is applied. In some cases e.g. the transonic flow simulation, the density-based approach is used due to compressibility.

In both approaches, the velocity field is obtained from the momentum equations. However, in the pressure-based approach the pressure field is obtained by solving a pressure or pressure correction equation which is obtained by manipulating the continuity and momentum equations. In the density-based approach, the continuity equation is used to obtain the density field while the pressure field is determined from the equation of state.

The control volume technique used in FLUENT requires spatial discretization. Spatial discreticzation interpolates the discrete values of the scalar at cell centers into the values at cell faces needed by the convection terms in the discretized governing equation. Several spatial discretization schemes are available for each scalar equation including momentum equation, energy equation, turbulent kinetic energy equation, etc. Most of the computations in this dissertation use the second-order upwind scheme while a few have also used the first-order upwind scheme. The upwind scheme derives the cell-face values from quantities at cell center upstream relative to the direction of the normal velocity. The second-order scheme achieves more accuracy than the first-order scheme while the latter generally yields better convergence.

For discretization of the momentum equation, a pressure interpolation scheme is used to compute the values of pressure at cell faces between the two cells from the values of pressure stored at cell centers. We use the PRESTO! (PREssure STaggerting Option) scheme since it has good performance for flows with high swirl numbers, high Rayleigh number (natural convection), high-speed rotating flows, flows involving porous media, and flows in strongly curved domains.

The discretization of the continuity equation is done so that it results in pressure-velocity coupling by reformulating the continuity equation to derive an additional condition for pressure. The pressure-based solver allows user to solve the flow problems in either a segregated or coupled manner. Among the five pressure-velocity coupling algorithms: SIMPLE, SIMPLES, PISO, Coupled and Fractional Step (FSM) in FLUENT. We use the coupled algorithm. The advantage of the coupled algorithm is that one can obtain a robust and efficient single phase implementation for steady-state flows with superior performance compared to the segregated solution schemes.

For calculating gradients, we employ Green-Gauss Node-Based Gradient Evaluation. Gradients are not only used to construct values of a scalar at the cell faces, but are also used to compute secondary diffusion terms and velocity derivatives. The Green-Gauss Node-Based scheme reconstructs exact values of a linear function at a node from surrounding cell-centered values on arbitrary unstructured meshes by solving a constrained minimization problem, thereby preserving a second-order spatial accuracy. This scheme is well known for being more accurate than other gradient calculation schemes especially on irregular unstructured meshes. It is more computationally expensive than other gradients.

The density-based solver is applied to calculation of transonic flow fields since for transonic flow the flow compressibility cannot be neglected.

In contrast to the pressure-based solver, the density-based solver solves the governing equations of continuity, momentum and energy and species transport simultaneously as a coupled set. The fact that the coupled set of governing equations is discretized in time for both steady and unsteady simulations requires the assumption that for steady simulations the time marching proceeds until a steady-state solution is reached. Two algorithms are available for the temporal discretization: the coupled-explicit formulation and the coupled-implicit formulation. This thesis uses the implicit formulation.

For the steady simulations using the density-based implicit solver, the Full Multigrid (FMG) initialization method is embedded with the density-based solver to accelerate the solution convergence. The FMG initialization provides a better initial solution at the start of the calculation at a minimum cost to the overall computational expense. The FMG initialization is computationally inexpensive because it does most of the work on coarse grid levels. For large problems, a good initial solution can be obtained in fraction of the time compared to time it takes to obtain a final converged solution.

Another feature embedded in the density-based solver is the first-to-higher order blending. Since higher-order scheme results in greater accuracy although it may have difficulties in convergence at certain flow conditions, this approach employs a discretization blending factor to achieve improved accuracy while maintaining good stability. A blending factor of 0 reduces the

gradient reconstruction to a first-order discretization scheme, whereas 1 recovers the high-order discretization.

4.3.9 Description of CFD solver FLUENT

The Reynolds-averaged Navier Stokes (RANS) are solved using the commercial code ANSYS-FLUENT, a widely used commercial finite-volume method (FVM) based software in computational fluid dynamics (CFD). It is employed to compute the aerodynamic properties such as coefficient of lift and drag of airfoils and 3D wings. It is a general-purpose CFD code based on the finite volume method on a collocated grid [85], which is capable of solving steady and unsteady incompressible and compressible, Newtonian and Non-Newtonian flows. FLUENT also provides several zero-, one-, two- equation turbulence models.

GAMBIT [78] is a pre-processing software used to build geometric models and to generate grids around those models. It allows users either to create their own geometry or to import geometry from most CAD packages. It can also automatically mesh surfaces and volumes while allowing the user to control the mesh through the use of sizing functions and boundary layer meshing. It can generate structured, unstructured and hybrid meshes depending upon the application.

4.4 Shape Parameterization

Shape parameterization is a procedure that uses a set of parameters to construct 2D and 3D geometries. In this dissertation we employ shape parameterization to define the airfoil and wing shapes.

For this purpose, Bezier curves are used. A Bezier curve is a parametric curve widely used in computer graphics and related fields. It was originally developed by Dr. Pierre Bezier in the 1970's [86]. A Bezier curve is defined by a set of control points P_0, P_1, P_2, P_3, ..., P_n, which

uniquely determined the shape of a specific curve. Bezier curves of any degree can be defined. A degree *n* Bezier curve has *n+1* control points whose blending functions are denoted by $B_i^n(t)$

where

$$B_i^n(t) = \binom{n}{i}(1-t)^{n-i}t^i \text{ , } i = 0, 1, ..., n. \tag{4-60}$$

The equation of a Bezier curve is given by:

$$P(t) = \sum_{i=0}^{n}\binom{n}{i}(1-t)^{n-i}t^i P_i \tag{4-61}$$

Figure 4-8 shows sample Bezier curves of degree one through four [87].

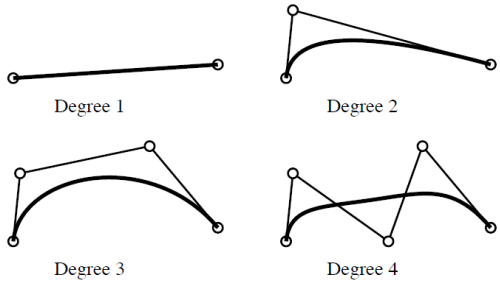

Figure 4-8 Bezier curves of various degrees

Chapter 5 Validation of Optimization Methodology

5.1 Overview

The goal of this chapter is to conduct shape optimization of both subsonic and transonic airfoils to validate the optimization methodology described in Chapter 4. We consider the optimization of RAE 2822 airfoil under subsonic flow condition and the optimization of RAE 2822 and NACA 0012 airfoils under transonic flow conditions to reduce their drag while maintaining (or even increasing) lift. MOGA is employed for optimization and the flow field is calculated using FLUENT.

The RAE 2822 airfoil has a maximum thickness of 12.1% chord length. Here, "RAE" stands for Royal Aircraft Establishment. It is a supercritical airfoil, which has become a standard test case for turbulence modeling validation [88]. Figures 5-1 and 5-2 show the airfoil shape and streamlines, and pressure distribution respectively for RAE 2822 at M = 0.75, Re = $6.2*10^6$, and α=2.8º [88].

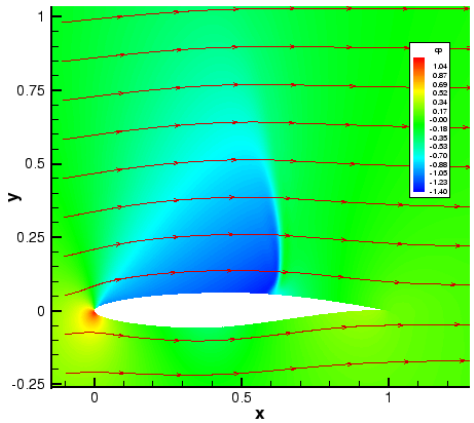

Figure 5-1 RAE 2822 airfoil: Pressure contours and streamlines at M = 0.75, Re = $6.2*10^6$, α = 2.8 º[88]

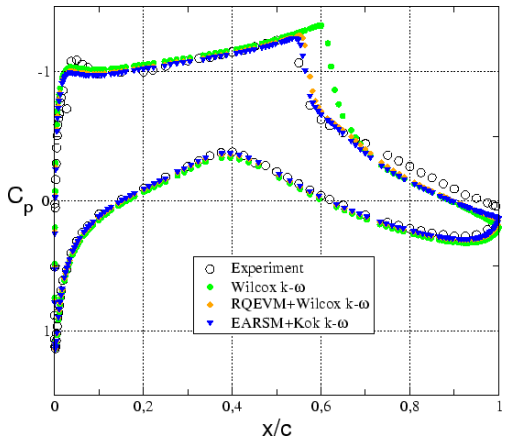

Figure 5-2 RAE 2822 airfoil: Pressure distribution at M = 0.75, Re = $6.2*10^6$, α = 2.8º [88]

The NACA 0012 is another widely used airfoil for CFD validation and shape optimization studies in transonic flow. The airfoil section shape of NACA 0012 is given by the following equation [77]:

$$y_t = \frac{t}{0.2} c \left[0.2969 \sqrt{\frac{x}{c}} - 0.1260 \left(\frac{x}{c}\right) - 0.3516 \left(\frac{x}{c}\right)^2 + 0.2843 \left(\frac{x}{c}\right)^3 - 0.1015 \left(\frac{x}{c}\right)^4 \right] \quad (5\text{-}1)$$

where *t* is the percentage of maximum thickness to chord which is 0.12 for NACA 0012. The airfoil shape given by equation (5-1) is shown in Figure 5-3:

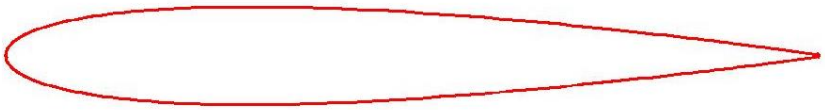

Figure 5-3 Geometry of the blade section of NACA 0012 airfoil

This study starts with the airfoils shown in Figures 5-1 and 5-3 as baseline airfoils and employs the multi-objective genetic algorithm (MOGA) to optimize their shapes to obtain shock-free shapes. The MOGA results are compared for the lift coefficient, the drag coefficient and lit to drag ratio with the values of these coefficients for the original airfoils given in References [89-91]. In all the optimization studies, the maximum thickness of the airfoils is allowed to vary within 2% of the chord from the baseline shapes.

5.2 Airfoil Parameterization

In all the optimization studies considered in this study, the maximum thickness is allowed to vary within 2% of the chord. Table 5-1 shows the maximum thickness constraints for the two airfoils.

The airfoil shapes are parameterized using Bezier curves. Bezier curves are parametric curves frequently used in computer graphics and relate fields. A Bezier curve is defined by a set of Bezier control points. Each curve can be expressed as math equations containing the information of Bezier control points. The number of points required to parameterize a curve depends on the shape of the curve.

Figure 5-4 is an example of Bezier curve and Bezier control points for one airfoil. Each airfoil is divided into top and bottom boundary curves by the chord, shown in different colors in Figure 5-4. Since the GA optimization involves fitness evaluation for a large number of airfoils with various shapes, five control points are used for both the top and bottom boundaries, thus the degree of the Bezier curve is four. For an airfoil curve, the first and the last point are fixed since they represent the leading and trailing edge of the airfoil. The intermediate points are allowed to move within the boundaries. At the top boundary, three control points (x_1, y_1), (x_2, y_2), and (x_3, y_3) are used. At the bottom boundary, three control points (m_1, n_1), (m_2, n_2), and (m_3, n_3) are employed. The constraints applied to the maximum thickness and the Bezier control points are shown in Table 5-1 and 5-2.

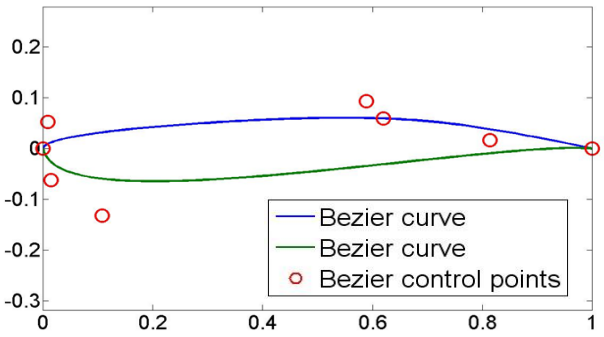

Figure 5-4 Example of Bezier curves and Bezier control points

Table 5-1 Maximum thickness constraints used for airfoil shape optimization in MOGA

	RAE 2822	**NACA 0012**
Top Boundary	0.11	0.11
Bottom Boundary	0.13	0.13
Baseline	0.121	0.12

Table 5-2 Parameters used for airfoil shape optimization in MOGA

Airfoil		**RAE 2822**	**NACA 0012**
Top Boundaries	x_1	0.03	0.03
	x_2	0.6	0.8
	x_3	0.9	1
	y_1	0.06	0.09
	y_2	0.11	0.11
	y_3	0.11	0.11
	m_1	0.04	0.04
	m_2	0.45	0.4
	m_3	0.9	1
	n_1	-0.02	-0.02
	n_2	-0.02	-0.02
	n_3	0.02	0.02
Airfoil		**RAE 2822**	**NACA 0012**
Bottom Boundaries	x_1	0	0
	x_2	0.03	0.03
	x_3	0.6	0.8
	y_1	0.02	0.02
	y_2	0.03	0.04
	y_3	0.04	0.04
	m_1	0	0
	m_2	0.04	0.04
	m_3	0.45	0.4
	n_1	-0.06	-0.09
	n_2	-0.2	-0.2
	n_3	-0.02	-0.04

5.3 Algorithm Implementation

This section describes the computational setup. Figure 5-5 schematically illustrates how the MOGA interfaces with the external mesh generator "GAMBIT" [78] and computational fluid dynamics (CFD) solver "FLUENT" [26].

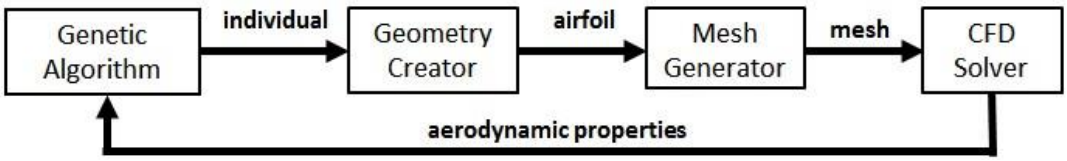

Figure 5-5 Illustration of information flow in MOGA process

5.3.1 Implementation of MOGA

The implementation of MOGA involves the following steps:

1) Initial generation creation: At the initial generation, the MOGA code generates a number of individuals according to the generation size. Since each individual represents one feasible airfoil, it contains the coordinates of the Bezier control points, which form the airfoil shapes using Bezier curves.

2) Mesh creation: Each individual is converted into real airfoil shape using the Bezier equations. Then their coordinates are written in a data file, which is passed on to the meshing program "GAMBIT". GAMBIT is used to create a two-dimensional structured or unstructured mesh. It first reads a previously written journal file and makes the mesh following the instructions from the journal file.

3) Flow-field computation: When a mesh is generated, it is then passed as input to the CFD flow solver FLUENT for computation of the flow field using a journal file. FLUENT is used iteratively to solve for the coefficient of lift C_l and the coefficient of drag C_d. Some combination of these values (either C_l and/or C_l/C_d) is taken as the quantities of interest (single or multiple objective values) to determine the objectives of the individual airfoil.

4) Optimization and new generation creation: When the objectives of all the individuals in the current generation are computed, the MOGA code collects them and uses them to determine the quality of each individual. After going through all the procedures for GA optimization described in the previous section, a new generation is created and all the steps of the GA are repeated for the new generation. The MOGA algorithm continues until the convergence in the objective value/s is achieved.

Employing the NSGA-II and the jMetal multi-objective GA software package mentioned in the previous section, this study employs a generation size of 20 individuals with the total number of generation of approximately 100. The crossover rate is 0.9. The mutation rate is determined by 1/(variable number). There are number of operators included in the jMetal framework for crossover, mutation and selection. In this study, the crossover section uses the simulated binary crossover (SBX) operator. The mutations section uses the polynomial mutation operator. The selection section uses the binary tournament operator.

There are two objectives in the calculation: objective 1 is to minimize ($100*C_d$) and objective 2 is to minimize ($1000*C_d/C_l$). Figure 5-6 shows an example of the Pareto solutions of the optimized RAE2822 airfoil. The x axis is objective 1 and the y axis is objective 2; they are both normalized to unity. Since this study focuses on minimizing C_d while maintaining C_l, we are more interested in objective 2. Therefore, the rightmost point in the Pareto front is chosen as the solution to the optimization problem. Then the convergence is determined in the following way: when the rightmost point in the Pareto front of each generation stops moving for a number of generations, which means the solution with the best performance of C_l/C_d after each generation is not getting better, it is considered that the convergence criteria is met. Usually the convergence happens in 100 generations or less.

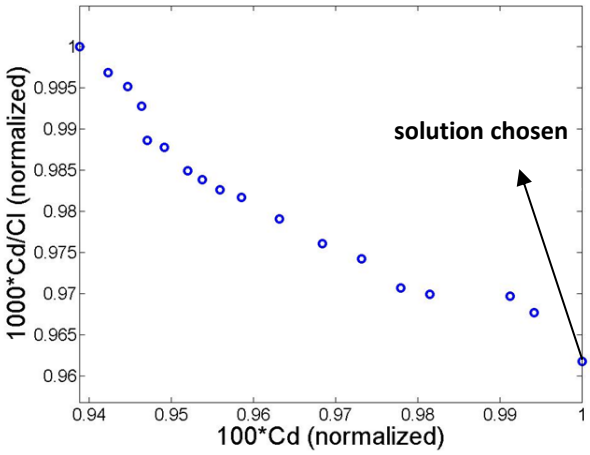

Figure 5-6 Pareto solutions for RAE 2822 airfoil

5.3.2 Mesh Generation

The commercially available software "GAMBIT" is used to generate a structured C-mesh or O-mesh for both the airfoils. Considering that NACA 0012 airfoil has a finite thickness at the trailing edge, a different shape of the domain is employed compared to that for the RAE 2822 airfoil which has a zero thickness trailing edge. A journal file is used to automatically produce a mesh that FLUENT can use to evaluate the objective functions of an airfoil.

The journal must be robust enough to create a usable mesh around any arbitrary airfoil. Therefore, the far-field boundary geometry of every mesh is held identical, but the airfoil in the center of the mesh changes every time. Faces of the grid are meshed using quadrilateral cells, and the numbers of nodes on opposite faces are required to be identical. To ensure this distribution, a set number of nodes (and not relative node spacing) is defined along each edge. Otherwise, thicker or more cambered airfoil edges would have more nodes than thinner ones if a relative distribution was used. Figures 5-7 and 5-8 show a typical C-mesh and O-mesh around the airfoil respectively. The interior of the boundary is meshed with a quadrilateral cell scheme. The resulting grid for Figure 5-7 has a node/cell/face count of 29,005/28,600/57,605 and for Figure 5-8 has a node/cell/face count of 40,950/40,500/81,450. When meshing is completed, the boundaries are defined and a 2D mesh is written to the file.

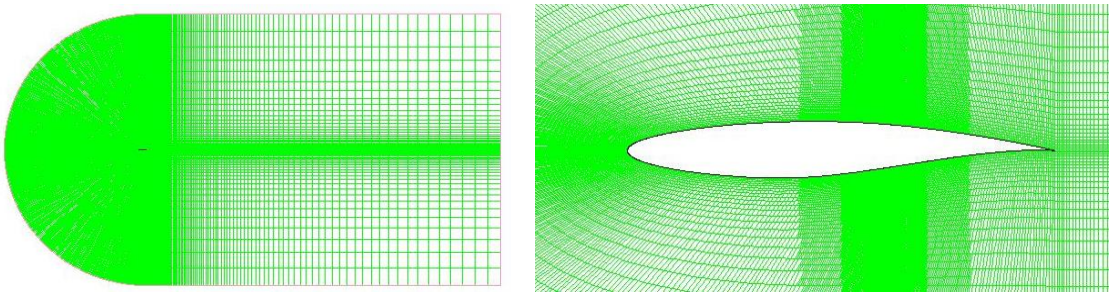

(a) Entire grid (b) Zoomed-in-view of the grid

Figure 5-7 C-Grid around the RAE 2822 airfoil

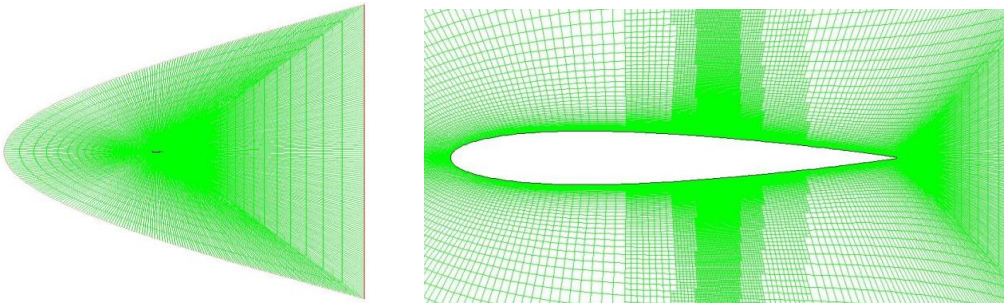

(a) Entire grid (b) Zoomed-in-view of the grid

Figure 5-8 O-Grid around the NACA 0012 airfoil

5.3.3 Flow Field Computation

FLUENT is used to solve for the coefficients of lift and drag for a given airfoil. A journal file is used to automatically initialize and evaluate each airfoil while saving a record of the relevant coefficients, C_l and C_d. The FLUENT journal initializes the calculations for a specific Mach number for each different case. In this study, a one equation S-A Turbulence Model is used. The air density is calculated from upstream pressure and temperature conditions using the ideal gas law and the laminar viscosity is calculated from the Sutherland's law:

$$\mu = \mu_0 \left(\frac{T}{T_0} \right)^{3/2} \left(\frac{T_0 + S}{T + S} \right) \tag{5-2}$$

with $\mu_o = 1.716 \times 10^{-5}$ kg/m*s, $T_o = 273$ K, and S=111 K.

Since both subsonic and transonic cases are optimized in this study, various Mach numbers are used in the flow calculations and optimization. For cases with Mach number of 0.73 and 0.75, the temperature is defined at the room temperature considering that the experimental data came from the wind tunnel tests; the static pressure is 101325 Pa. The solver type is Pressure-based and the solution method is explicit. For the case of Mach number 0.8, the solver type is density-based and the solution method is implicit; the temperature is 275.709K and the static pressure is 66470 Pa determined using the compressible flow equations:

$$\frac{p}{p_0} = [1 + (\frac{\gamma - 1}{2})M^2]^{\frac{\gamma}{\gamma - 1}} \tag{5-3}$$

where p_0 = total pressure = 101325 Pa and γ = 1.4 for air

$$\frac{T}{T_0} = 1 + (\frac{\gamma - 1}{2})M^2 \tag{5-4}$$

where T_0 = total temperature = 311 K and γ = 1.4 for air

5.4 Results and Discussion

5.4.1 Optimization Results

In this study, our primary objective has been to generate optimized NACA 0012 and RAE 2822 airfoils that minimize the shock strength in subsonic and transonic flow without reducing the lift. Four flow cases for the original NACA 0012 and RAE 2822 airfoils are used as baseline cases for optimization. Table 5-3 shows the flow conditions, angles of attack, wind tunnel experimental results and computational validation results using FLUENT. Before performing the optimization, CFD solutions were validated using the wind tunnel data for the baseline airfoils. The same mesh and computational settings were then applied to the new optimized airfoils created by the MOGA process.

Table 5-3 Baseline airfoils test cases with experimental and computational results

Airfoil	Mach Number	Angle of Attack	C_l / C_d		C_l		C_d	
			Test	CFD	Test	CFD	Test	CFD
RAE 2822 I	0.73	2.0	39.41	54.17	0.67	0.65	0.017	0.012
RAE 2822 II	0.75	2.8	30.7	28.9	0.74	0.74	0.024	0.0255
NACA0012 I	0.75	2.0	19.29	19.34	0.328	0.3206	0.017	0.0166
NACA0012 II	0.80	1.5	7.16	6.18	0.27	0.27	0.037	0.0429

Figure 5-9 shows the typical "evolution" of an optimized airfoil using the genetic algorithm. This figure plots the best objective 1 (100*C_d) in each generation against the generation number. It illustrates the convergence history for NACA 0012 II case. It should be noted that the solution is nearly optimal after about 80 generations. In Figure 5-9, the C_l, C_d and C_l / C_d of various airfoils at different generations are shown. They converge to a value of C_l = 0.26522, C_d = 0.026227 and C_l / C_d = 10.11 after about 80 generations. Table 5-4 shows various airfoil coefficients during the convergence process.

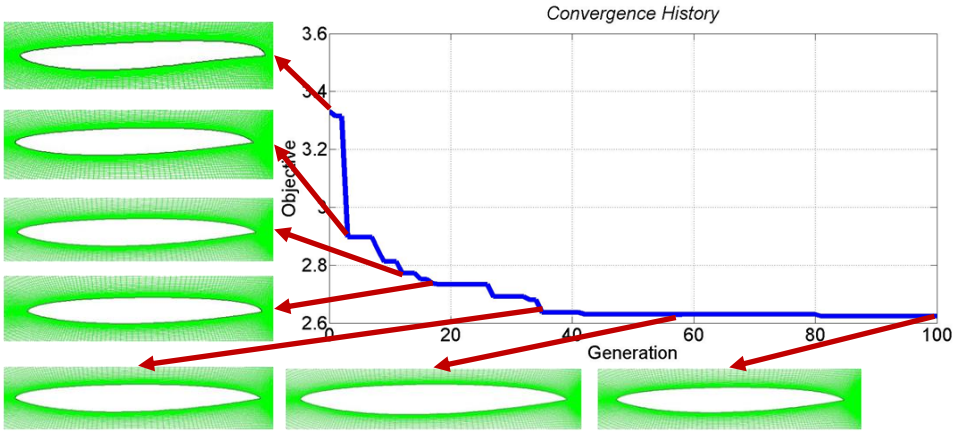

Figure 5-9 Convergence history of shape optimization of NACA 0012 II airfoil using the GA algorithm

Table 5-4 Airfoils aerodynamic properties at different generations

Generation Number	Objective 1 100*Cd	Cl	Cd	Cl/Cd
0	3.331022	0.24673	0.03331	7.407023
3	2.896753	0.289217	0.028968	9.984172
9	2.812022	0.279371	0.02812	9.93489
18	2.733454	0.265976	0.027335	9.730389

36	2.63671	0.267701	0.026367	10.15285
58	2.629238	0.26618	0.026292	10.12385
100	2.622685	0.26522	0.026227	10.11248

Table 5-5 shows the comparison of results between the original airfoils (Figure 5-1, 5-3) and the optimized airfoils at various Mach numbers and angles-of-attack. For all the four test cases, the optimized airfoils have larger C_l / C_d and smaller C_d, C_l is either slightly reduced or increased. The maximum thickness is also close to that of the original airfoils (within 8%). Figures 5-10, 5-11, 5-12 and 5-13 shows (a) the optimized shape, (b) the pressure distribution, and (c) the velocity contours for the optimized RAE 2822 airfoil (case I and II) and NACA 0012 airfoil (case III and IV) at various Mach numbers and angle of attack respectively. All the four test cases have achieved shock-free airfoils. These results clearly demonstrate the superior performance of the optimized airfoils obtained using MOGA.

Table 5-5 Comparison of results for original and optimized RAE 2822 and NACA 0012 airfoils

Airfoil	Ma	Angle of Attack	Optimized Maximum Thickness	C_l / C_d		C_l		C_d	
				optimized	original	optimized	original	optimized	original
RAE 2822 I	0.73	2.0	0.11c	57	39.41	0.65	0.67	0.0114	0.017
RAE 2822 II	0.75	2.8	0.11c	48.32	30.7	0.72	0.743	0.0149	0.0242
NACA0 012 I	0.75	2.0	0.112c	33.425	19.29	0.3767	0.328	0.01127	0.017
NACA0 012 II	0.8	1.5	0.11c	10.11	7.16	0.2652	0.265	0.02622	0.037

(a) Airfoil Shape

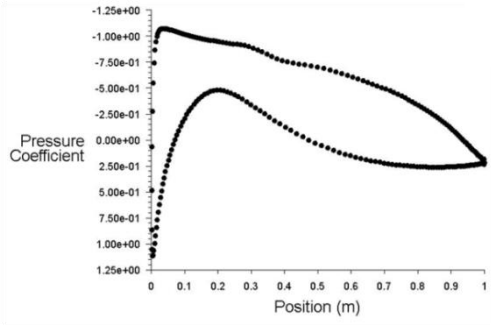

(b) Pressure Distribution

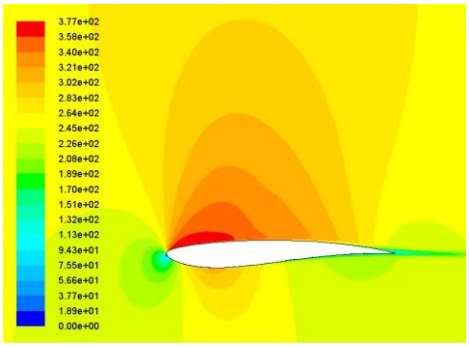

(c) Velocity contours (Zoomed-in view)

Figure 5-10 Results for optimized RAE 2822 airfoil, M = 0.73, α = 2 degree

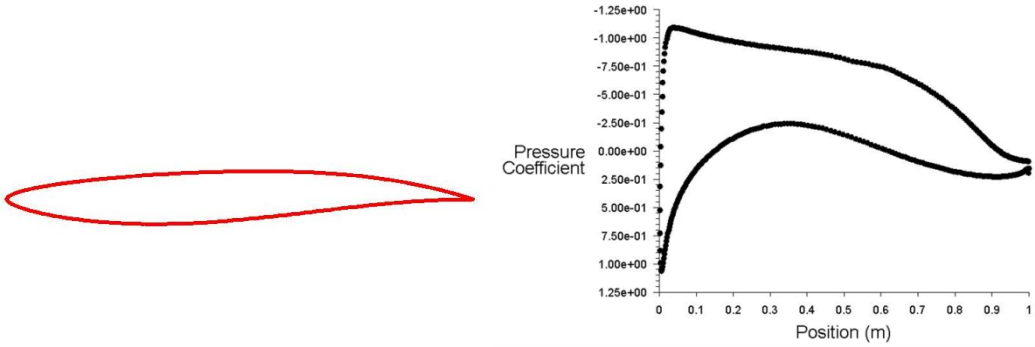

(a) Airfoil Shape (b) Pressure Distribution

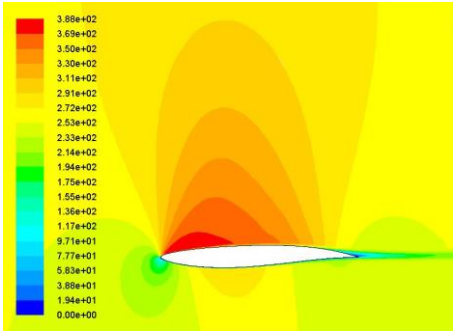

(c) Velocity Contours (Zoomed-in view)

Figure 5-11 Results for optimized RAE 2822 airfoil, M = 0.75, α = 2.8 degree

(a) Airfoil Shape (b) Pressure Distribution

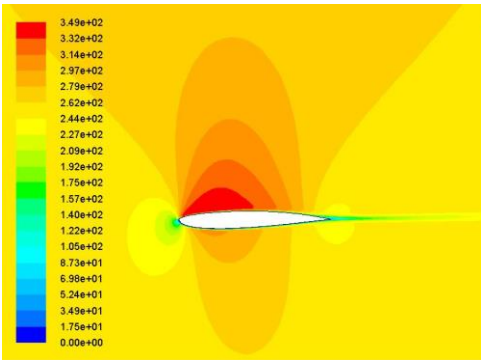

(c) Velocity Contours (Zoomed-in view)

Figure 5-12 Results for optimized NACA 0012 airfoil, M = 0.75, α = 2 degree

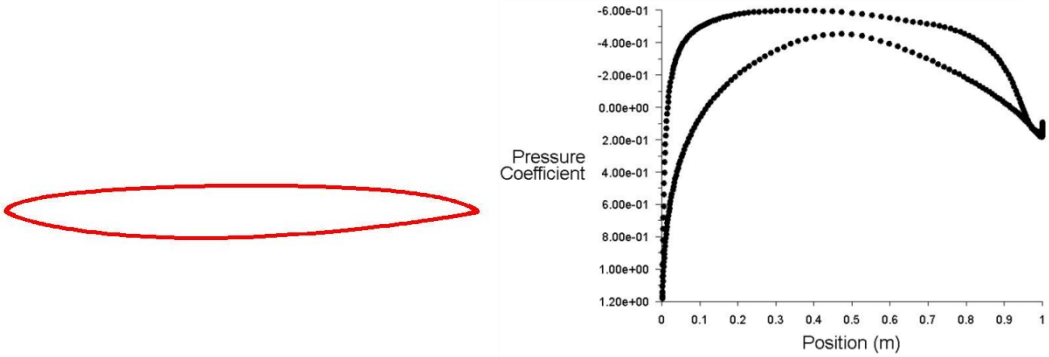

(a) Airfoil shape (b) Pressure distribution

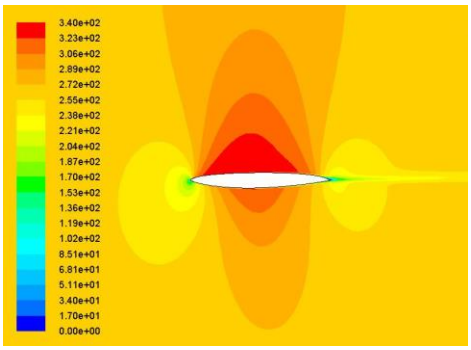

(c) Velocity contours (zoomed-in view)

Figure 5-13 Results for optimized NACA 0012 airfoil, M = 0.85, α = 1.5 degree

5.4.2 Discussion

Figures 5-14, 5-15, 5-16 and 5-17 show the comparison of optimized and original airfoil shapes and pressure distributions for RAE 2822 and NACA 0012 airfoils at different flow conditions obtained using MOGA.

Compared to the original airfoils, the optimized airfoils have superior performance in reducing shock drag. Table 5-6 shows that the drag coefficients are all reduced by about 30% to 40% compared to the baseline airfoils while their maximum thicknesses are altered by less than 10%. Their lift coefficients either increase or are the same for NACA 0012 test cases and decrease by only about 3% for both RAE 2822 test cases, which is within the acceptable range. All the optimized airfoils have much improved C_l/C_d increasing from 40% to 70%.

The reason for a small reduction in C_l for RAE airfoils is as follows. The original RAE 2822 airfoil is already a supercritical airfoil. It had been improved before based on the conventional airfoil so that the supercritical airfoil shape can minimize the strength of the shock wave and create the shock wave as far as possible downstream, thus reducing drag in the transonic speed range. In order to further improve the airfoil shape so that the shock is completely eliminated, a small reduction in the maximum thickness of the airfoil within the

acceptable range is needed, which consequently reduces the lift by a small amount. In this study, the lift reduction and shape change are both within the acceptable range.

Table 5-6 Relative improvement in the properties of optimized airfoils compared to the original airfoils

Airfoil	Maximum Thickness (%)	C_l / C_d (%)	C_l (%)	C_d (%)
RAE 2822 I	-9	44.6333	-2.985	-32.941
RAE 2822 II	-9	57.3941	-3.096	-38.43
NACA0012 I	-7.8	73.2763	14.8476	-33.706
NACA0012 II	-8.3	41.2011	0.0755	-29.135

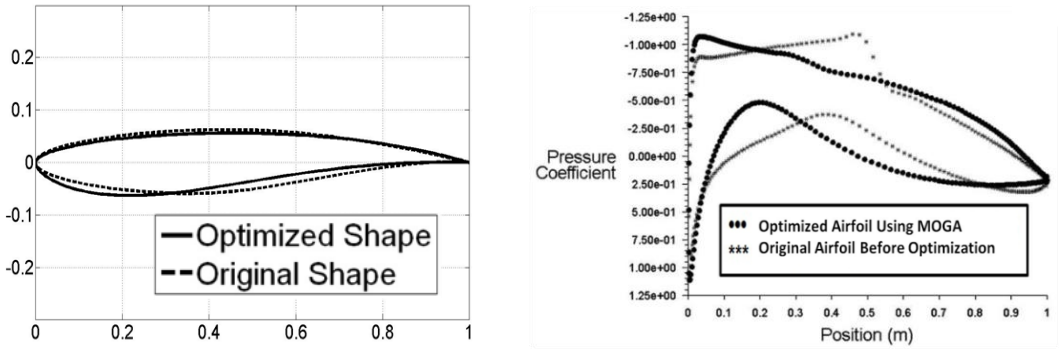

(a) Airfoil shapes comparison (b) Pressure distributions comparison

Figure 5-14 Comparison of original and optimized RAE 2822 airfoil shapes and pressure distributions; M = 0.73, α = 2 degree

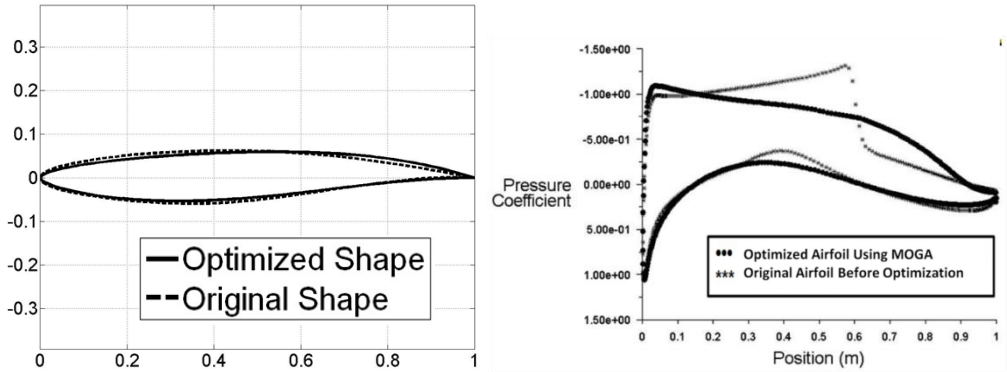

(a) Airfoil shapes comparison (b) Pressure distributions comparison

Figure 5-15 Comparison of original and optimized RAE 2822 airfoil shapes and pressure distributions; M = 0.75, α = 2.8 degree

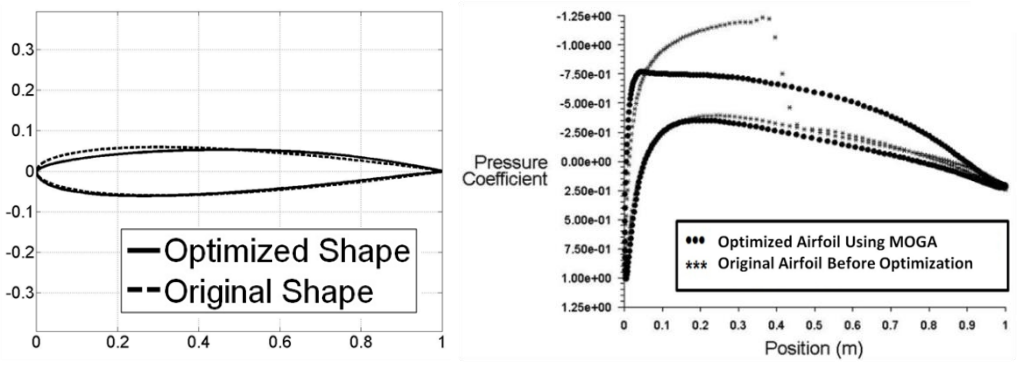

(a) Airfoil shapes comparison (b) Pressure distributions comparison

Figure 5-16 Comparison of original and optimized NACA 0012 airfoil shapes and pressure distribution; M = 0.75, α = 2 degree

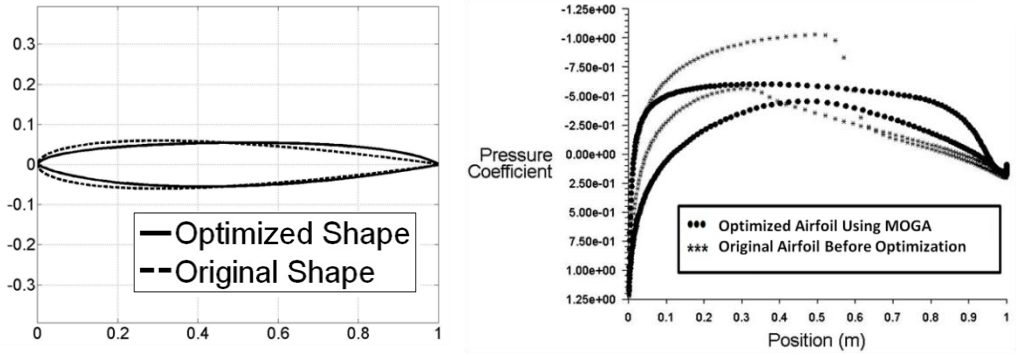

(a) Airfoil shapes comparison (b) Pressure distributions comparison

Figure 5-17 Comparison of original and optimized NACA 0012 airfoil shapes and pressure distributions; M = 0.8, α = 1.5 degree

Chapter 6 Optimization of Wind Turbine Airfoils

6.1 Overview

The focus of this chapter is on the optimization of wind turbine airfoils using the methodology presented in Chapter 4. We first consider the optimization of Flatback Airfoils will be optimized which have been recently proposed for wind-turbine applications. Next we consider the more commonly used wind turbine airfoils FX 66-S196-V1, DU 91-W2-250, NACA 64418 and NACA 64421. The Flatback airfoils are optimized using both SOGA and MOGA, showing that MOGA has more advantages since it can address multiple optimization objectives. The MOGA is also applied to the optimization of FX 66-S196-V1, DU 91-W2-250, NACA 64418 and NACA 64421 airfoils. CFD tools are employed to compute the flow field and the aerodynamic properties.

As described by Baker et al. [73], the flatback (FB) series of airfoils was generated by combining a low pressure-side shape drawn from the thick, high lift inboard NREL airfoils, and a structurally efficient high-pressure side drawn from the LS-1 series airfoils. Figure 6-1 shows the family of FB airfoils developed by Sandia National Laboratory in collaboration with University of California – Davis as part of the Blade System Design Study (BSDS) [69].

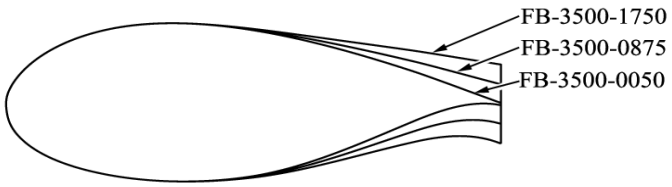

Figure 6-1 Geometries of blade sections of three flatback FB series of airfoils given in Baker et al. [73]

The baseline airfoil FB-3500-0050 has a nominally sharp trailing edge. The actual trailing edge thickness-to-chord ratio of this airfoil is not zero but 0.5%. The FB-3500-0875 airfoil has the identical maximum thickness as the FB-3500-0050 airfoil but has a trailing edge thickness of 8.75% of chord length. The blunt trailing edge is created by symmetrically adding the thickness to either side of the camber line of FB-355-0050 airfoil, aft of the maximum thickness, using an exponential blending function to smoothly distribute the increased thickness along the chord [71]. The FB-3500-1750 airfoil has the identical maximum thickness as the FB-3500-0050 and the FB-3500-0875 airfoils but has a trailing edge thickness of 17.5% of chord length. According to Tangler and Somers [92], sharp trailing-edge airfoils with $t/c < 0.25$ can be designed to have lift characteristics that are largely insensitive to surface soiling. Hence a simple guideline for blunt trailing edge airfoils is to limit the difference between the maximum thickness to trailing edge thickness to ~ 20% of chord length. In doing so, the adverse pressure gradient on aft portion of the suction surface is reduced, which in turn improves the achievable lift characteristics under soiled conditions. Based on this rule of thumb, one would expect to see significant sensitivity to surface soiling for the FB-3500-0050 and FB-3500-0875 airfoils, and little or no sensitivity for the FB-3500-1750 airfoil. In this study, we start with the three airfoils shown in Figure 6-1 as baseline airfoils and use the multi-objective GA to optimize their shapes for maximum lift as well as maximum lift to drag ratio. The multi-objective GA results are compared with single objective GA results of Chen and Agarwal [93]. In all optimization studies, the thickness of the blunt trailing edge is kept fixed to the same value as the thickness of the baseline airfoil. As to the maximum thickness as constraint, we consider allowing the maximum thickness to vary between 30% to 35% of chord length.

We also conduct shape optimization of four commonly used wind turbine airfoils to increase their lift as well the lift to drag ratio. They are FX 66-S196-V1, DU 91-W2-250, NACA 64418 and NACA 64421 airfoils. As shown in Figure 6-2, the FX 66-S196-V1 airfoil has a maximum thickness of 19.6% of chord length. It is a typical laminar airfoil where transitional effects can be large since laminar flow is present over majority of the airfoil surface [94].

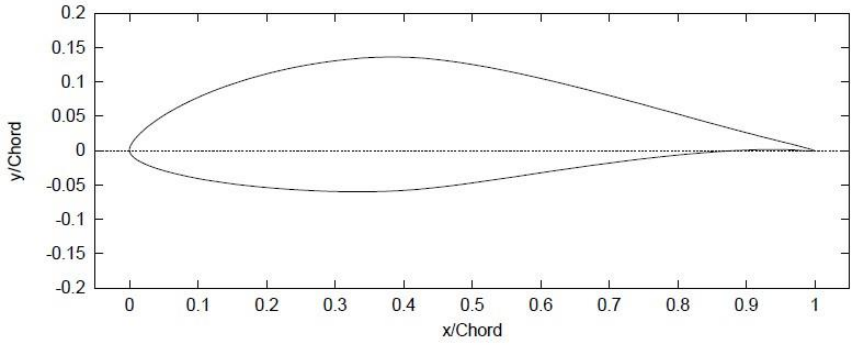

Figure 6-2 Geometry of the blade section of FX 66-S196-V1 airfoil [94]

Figure 6-3 shows the shape of DU 91-W2-250 airfoil. The 25% thick airfoil was designed by Professor W.A. Timmer of the Delft University of Technology. Its design goals for laminar flow conditions were a peak lift coefficient of about 1.5, relatively smooth stall and insensitivity to roughness [75]. In the designation of the airfoil, DU stands for Delft University. The following two digits 91 imply that the airfoil was designed in year 1991. The W denotes the wind energy application, to distinguish the airfoil from the ones designed for sail-planes and general aviation. The following number 2 denotes that there has been more than one design with a thickness of about 25% that year. The last three digits give 10 times the airfoil maximum thickness in percentage of the chord [94].

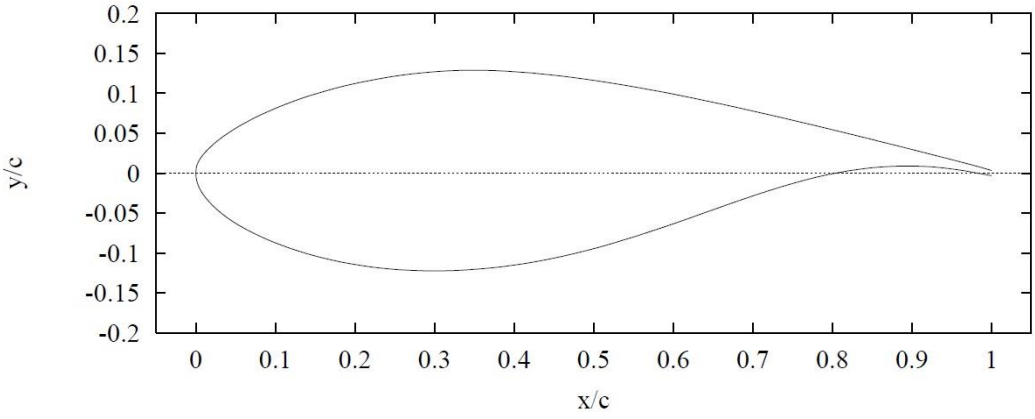

Figure 6-3 Geometry of the blade section of DU 91-W2-250 airfoil [94]

The NACA 64418 and NACA 64421 airfoils belong to the NACA 64 series airfoils. The first digit 6 denotes the series and indicates that this family is designed for greater laminar flow on the surface than the airfoil series beginning with digit 4 or 5. The second digit 4 denotes the location of the minimum pressure in tenths of chord (0.4c). The following digit 4 specifies the

design lift coefficient (0.4). The final two digits specify the thickness in percentage of chord. The NACA 66418 airfoil has maximum thickness of 18% of the chord and the NACA 66421 airfoil has maximum thickness of 21% of the chord [77]. Figure 6-4 shows the shape of NACA 64418 and 64421 airfoils.

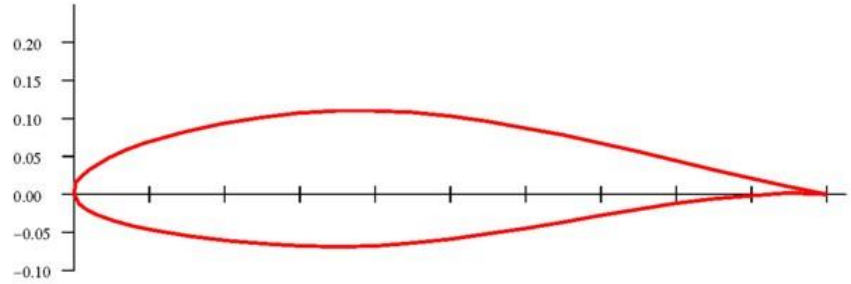

(a)

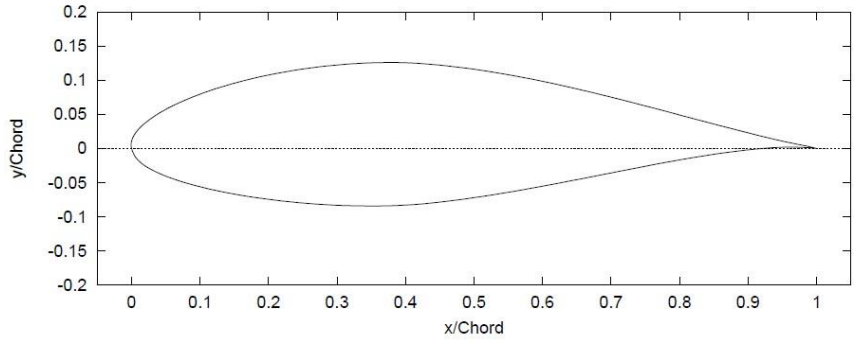

(b)

Figure 6-4 Geometries of blade sections of (a) NACA 64418 and (b) 64421 airfoils [77]

In this study, we start with the airfoils shown in Figures 6-2, 6-3 and 6-4 as baseline airfoils and employ the multi-objective genetic algorithm (MOGA) to optimize their shapes for maximum lift as well as maximum lift to drag ratio. The MOGA results are compared with the lift coefficient and lit to drag ratio results for the original airfoils reported in References [76, 94]. In all the optimization studies, the maximum thickness of the airfoils is allowed to vary within 2% of the chord from the baseline shape.

6.2 Airfoil Parameterization

For all the cases of Flatback airfoils optimization, the thickness of the blunt trailing edge is kept fixed at the same value as the thickness of the baseline airfoil. As to the maximum thickness as a constraint, it is allowed to vary between the thickness of 0.3c to 0.35c. The airfoil shapes are parameterized using Bezier curves. Bezier curves are parametric curves frequently used in computer graphics and relate fields. A Bezier curve is defined by a set of Bezier control points. Each curve can be expressed as math equations containing the information of Bezier control points. The number of points required to parameterize a curve depends on the shape of the curve. Figure 6-5 is an example of Bezier curve and Bezier control points for one Flatback airfoil.

Each Flatback airfoil is divided into top and bottom boundary curves by the chord, shown in Figure 6-5. Since the GA optimization involves fitness evaluation for a huge number of airfoils with various shapes, 5 control points are used for both the top and bottom boundaries, that is to say the degree of the Bezier curve is 4. For an airfoil curve, the first and the last point are fixed since they represent the leading and trailing edge of the airfoil. The intermediate points are allowed to move within the boundaries. The constraints applied to the Bezier control points of Flatbak airfoils are shown in Table 6-1 and Table 6-2.

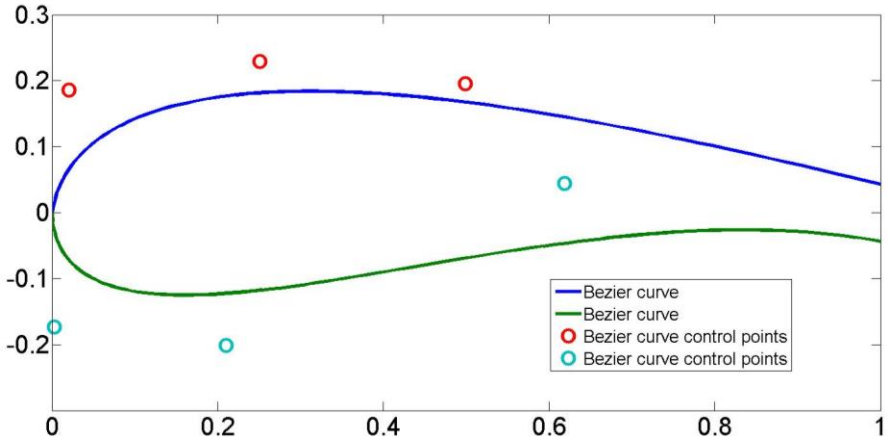

Figure 6-5 Example of Bezier curves and Bezier control points

Table 6-1 Parameters used for Flatback airfoil shape optimization in SOGA

Airfoil		**FB-0050**	**FB-0875**	**FB-1750**
Top Boundaries	***x1***	0.2	0.3	0.3
	x2	0.6	0.6	0.6
	x3	0.9	0.9	0.9
	y1	0.265	0.23	0.23
	y2	0.23	0.23	0.23
	y3	0.23	0.23	0.23
	m1	0.1	0.3	0.3
	m2	0.25	0.6	0.6
	m3	0.9	0.9	0.9
	n1	-0.14	-0.16	-0.16
	n2	-0.15	-0.16	-0.16
	n3	0.02	0	0
Airfoil		**FB-0050**	**FB-0875**	**FB-1750**
Bottom Boundaries	***x1***	0	0	0
	x2	0.2	0.3	0.3
	x3	0.6	0.6	0.6
	y1	0.16	0.16	0.16
	y2	0.16	0.16	0.16
	y3	0.12	0.16	0.16
	m1	0	0	0
	m2	0.1	0.3	0.3
	m3	0.25	0.6	0.6
	n1	-0.23	-0.23	-0.23
	n2	-0.23	-0.23	-0.23
	n3	-0.1	-0.23	-0.23

Table 6-2 Parameters used for Flatback airfoil shape optimization in MOGA

Airfoil		**FB-0050**	**FB-0875**	**FB-1750**
Top Boundaries	***x1***	0.2	0.1	0.3
	x2	0.6	0.3	0.6
	x3	0.9	0.9	0.9
	y1	0.265	0.23	0.23
	y2	0.23	0.23	0.23
	y3	0.23	0.23	0.23
	m1	0.03	0.2	0.3
	m2	0.23	0.6	0.6
	m3	0.9	0.9	0.9

	n1	-0.14	-0.14	-0.16
	n2	-0.15	-0.16	-0.12
	n3	0.1	0.05	0
Airfoil		**FB-0050**	**FB-0875**	**FB-1750**
Bottom Boundaries	***x1***	0	0	0
	x2	0.2	0.1	0.3
	x3	0.6	0.3	0.6
	y1	0.16	0.16	0.16
	y2	0.16	0.16	0.16
	y3	0.12	0.14	0.16
	m1	0	0	0
	m2	0.03	0.2	0.3
	m3	0.23	0.6	0.6
	n1	-0.23	-0.23	-0.23
	n2	-0.23	-0.23	-0.16
	n3	-0.1	-0.2	-0.23

In all the optimization cases of FX 66-S196-V1, DU 91-W2-250, NACA 64418 and NACA 64421 airfoils, the maximum thickness is allowed to vary within 2% of the chord. Table 6-3 shows the maximum thickness constraints for each of the four airfoils.

The airfoil shapes are also parameterized using Bezier curves as discussed above. Figure 6-6 is an example of Bezier curve and Bezier control points for one typical airfoil. Each airfoil is divided into top and bottom boundary curves by the chord, shown in Figure 6-6. 5 control points are used for both the top and bottom boundaries, that is to say that the degree of the Bezier curve is 4. For an airfoil curve, the first and the last point are fixed since they represent the leading and trailing edge of the airfoil. The intermediate points are allowed to move within the boundaries. The constraints applied to Bezier control points are shown in Table 6-4.

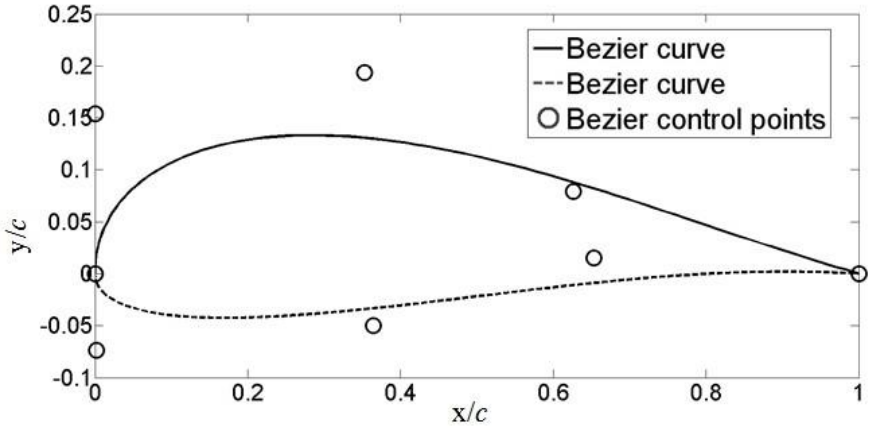

Figure 6-6 Example of Bezier curves and Bezier control points

Table 6-3 Maximum thickness constraints used for airfoil shape optimization in MOGA

	FX 66-S-196 V1	**DU 91-W2-250**	**NACA 64418**	**NACA 64421**
Top Boundary	0.21	0.27	0.20	0.23
Bottom Boundary	0.17	0.23	0.16	0.19
Baseline	0.196	0.25	0.18	0.21

Table 6-4 Parameters used for airfoil shape optimization in MOGA

Airfoil		**FX 66-S-196 V1**	**DU 91-W2-250**	**NACA 64418**	**NACA 64421**
Top Boundaries	x_1	0.3	0.02	0.02	0.02
	x_2	0.6	0.4	0.65	0.65
	x_3	1	1	1	1
	y_1	0.18	0.15	0.12	0.12
	y_2	0.2	0.25	0.23	0.25
	y_3	0.15	0.18	0.08	0.11
	m_1	0.3	0.02	0.03	0.03
	m_2	0.6	0.27	0.66	0.65
	m_3	1	1	0.85	0.85
	n_1	-0.07	-0.07	-0.05	-0.05
	n_2	-0.05	-0.13	-0.06	-0.15
	n_3	0.15	0.04	0.015	0.045
Airfoil		**FX 66-S-196 V1**	**DU 91-W2-250**	**NACA 64418**	**NACA 64421**
Bottom Boundaries	x_1	0	0	0	0
	x_2	0.3	0.02	0.02	0.02
	x_3	0.6	0.04	0.65	0.65
	y_1	0.08	0.1	0.07	0.07

	y_2	0.1	0.2	0.17	0.2
	y_3	0.05	0.13	0.03	0.06
	m_1	0	0	0	0
	m_2	0.3	0.02	0.03	0.03
	m_3	0.6	0.27	0.66	0.65
	n_1	-0.17	-0.12	-0.1	-0.1
	n_2	-0.15	-0.18	-0.12	-0.2
	n_3	-0.05	0	0	0

6.3 Algorithm Implementation

In this section we describe the computational setup. Figure 6-7 schematically illustrates how the GA interfaces with the external mesh generation and flow solver software.

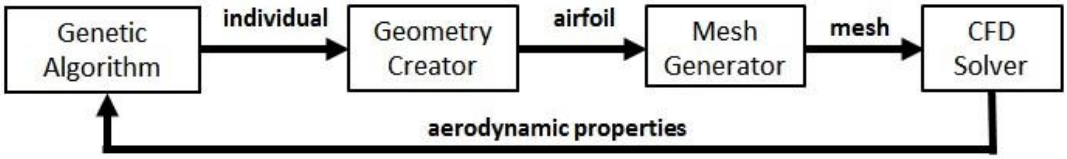

Figure 6-7 Illustration of information flow in GA process

A GA individual is represented by an airfoil geometry data file, which is passed to the meshing program *Gambit*. Gambit is used to create a two-dimensional structured or unstructured mesh, which is then passed as input to the CFD flow solver FLUENT for computation of the flow field. FLUENT is used iteratively to solve for the coefficient of lift C_l and the coefficient of drag C_d. Some combination of these values (either C_l and/or C_l/C_d) are taken as the quantities of interest (single or multiple objective values) to determine the fitness of the airfoil. The algorithm shown in Figure 6-7 continues until the convergence in the objective values is achieved.

6.3.1 Implementation of SOGA

The SOGA algorithm is applied to optimization of Flatback airfoils. The airfoil parameterization is used to parameterize an airfoil. All airfoils are scaled to have a chord length of unity; the other parameters are constrained such that the blunt trailing edge is of fixed thickness (same as in baseline airfoil) and the specified maximum thickness of the airfoil is distributed evenly about

the camber line. Employing the NSGA-II and the jMetal single- and multi-objective GA software packages mentioned in the previous sections, this study employs a generation size of 20 individuals with a crossover probability of 1. The mutation rate is determined as 1/(the number of variables). There are a number of operators included in the jMetal framework. In this study, the crossover section uses the simulated binary crossover (SBX) operator; the mutations section uses the polynomial mutation operator; and the selection section uses the binary tournament operator.

For SOGA, the only objective considered is maximization of C_l / C_d. Convergence is achieved when the fitness of all individuals in a generation is very close to each other or when 250 generations have passed. The second constraint on convergence is applied to prevent the algorithm from running for unreasonable amount of time; generally the convergence is achieved in less than hundred generations.

6.3.2 Implementation of MOGA

MOGA is applied to all the airfoil optimization cases. The implementation of MOGA follows the following steps:

(1) Initial generation creation: At the initial generation, the MOGA code generates a number of individuals according to the selected generation size. Since each individual represents one feasible airfoil, it contains the coordinates of the Bezier control points, which form the airfoils shapes using Bezier curves.

(2) Mesh generation: Each individual is converted into real airfoil shape using Bezier equations. Then their coordinates are written in a data file, which is passed to the meshing program "GAMBIT". GAMBIT is used to create a two-dimensional structured or unstructured mesh. It first reads a previously written journal file and makes the mesh following the instructions from the journal file.

(3) Computation of objective values: When a mesh is made, it is then passed as input to the CFD flow solver FLUENT for computation of the flow field using a journal file. FLUENT is

used to solve for the coefficient of lift C_l and the coefficient of drag C_d. Some combination of these values (either C_l and/or C_l/C_d) are taken as the quantities of interest (single or multiple objective values) to determine the objective (fitness) values for the individuals.

(4) Optimization and new generation creation: When the objective values of all the individuals in the current generation get computed, the MOGA code collects them and uses them to determine the quality of each individual. After going through all the procedures for GA optimization described Chapter 4, a new generation is created and all the steps are repeated beginning from step 1 above. The MOGA algorithm shown in Figure 6-7 continues until the convergence in the objective value/s is achieved.

Employing the NSGA-II and the jMetal multi-objective GA software package mentioned in Chapter 4, this study employs a generation size of 20 individuals with the total generation number of 100. The crossover rate is 0.9. The mutation rate is determined by 1/ (variable number). There are a number of operators included in the jMetal framework. In this study, the crossover section uses the simulated binary crossover (SBX) operator. The mutations section uses the polynomial mutation operator. The selection section uses the binary tournament operator.

There are two objectives in the calculation: objective 1 is to minimize ($10/C_l$) and objective 2 is to minimize ($100C_d/C_l$). Figure 6-8 is one example of the Pareto solutions of the optimized FX airfoil. The x axis is objective 1 and the y axis is objective 2, they are both normalized to unity. Since this study has greater emphasis on objective 2, the rightmost point in the Pareto front is chosen as the solution to the optimization problem. Then the convergence is determined in this manner: when the rightmost point in the Pareto front of each generation has stopped moving for a number of generations, which means that the solution with the best performance of C_l/C_d of each generation is not improving further, it is considered that the convergence criteria has been achieved. Usually the convergence is obtained after 80 generations.

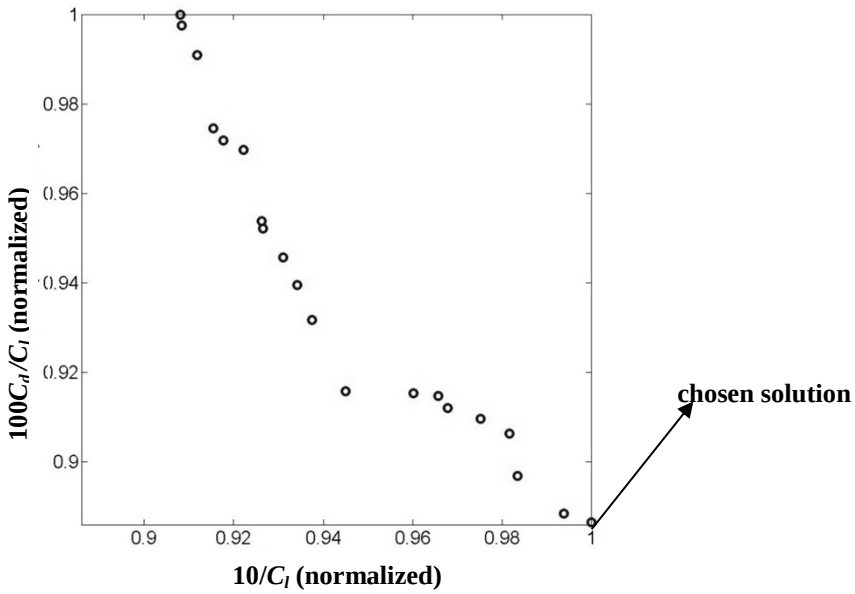

Figure 6-8 Pareto solutions for FX 66-S-196 V1 airfoil

6.3.3 Mesh Generation

The commercially available software "GAMBIT" is used to generate a structured C-mesh for FX and NACA 64 series airfoils and O-mesh for Flatback and DU airfoils considering that they have a finite thickness at the trailing edge. We use a journal file to automatically produce a mesh that FLUENT can use to evaluate an airfoil. The journal must be robust enough to create a usable mesh around any arbitrary airfoil. Therefore, the far-field boundary geometry of every mesh is held identical, but the airfoil in the center of the mesh changes every time. Faces of the grid are meshed using quadrilateral cells, and we require that the number of nodes on opposite faces be identical. To ensure this distribution, we define a set number of nodes (and not relative node spacing) along each edge. Otherwise, thicker or more cambered airfoil edges would have more nodes than thinner ones if a relative distribution were used.

Figure 6-9, 6-10 and 6-11 show a typical C-mesh and O-mesh around the airfoil respectively. The interior of the boundary is meshed with a structured quadrilateral cell scheme. The meshes around the airfoil are very dense and are carefully refined so that they can have a

very good prediction of the boundary layer characteristics especially when there is boundary layer separation on the suction surface. In Figure 6-9, most of the grids have an approximate node/cell/face count of 13,006/12,600/25,606. Figure 6-10 has a node/cell/face count of 39,422/38,880/78,302 and Figure 6-11 has a node/cell/face count of 29,160,422/28,800/57,960. To test whether the grid used is fine enough, calculations were also performed on a coarser grid with one-fourth the numbers of cells. When meshing is completed, the boundaries are defined and a 2D mesh is written to the file.

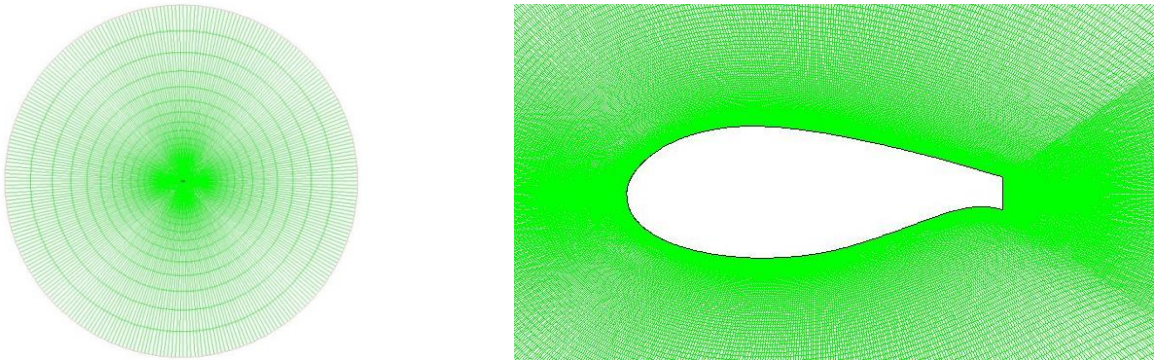

Figure 6-9 O-Grid around the FB-3500-0875 airfoil

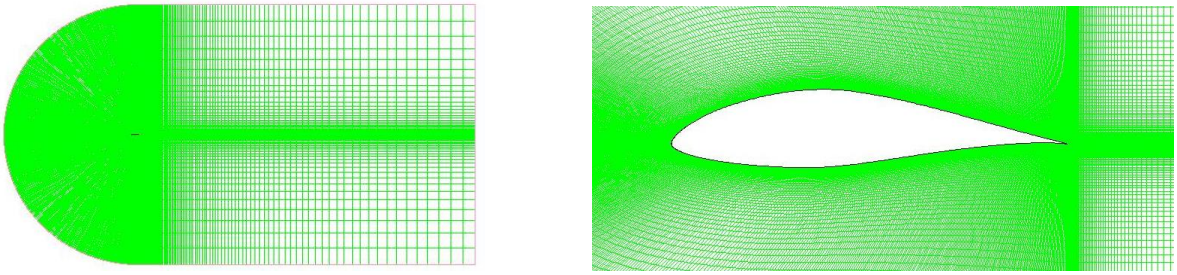

Figure 6-10 C-Grid around the FX 66-S-196 V1 airfoil

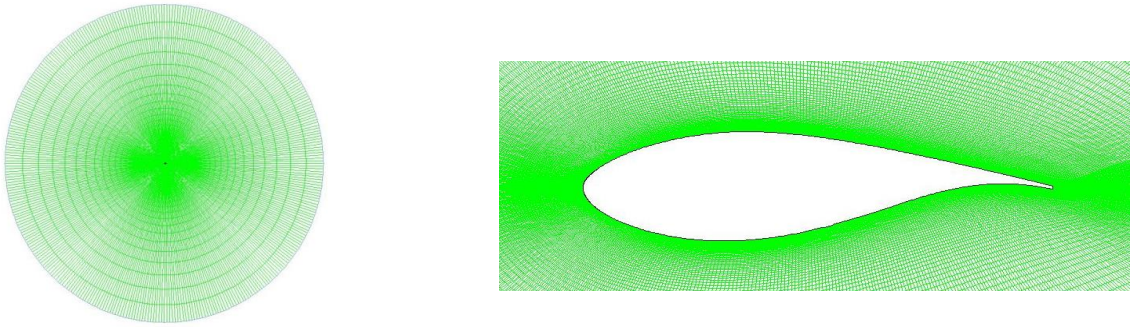

Figure 6-11 O-Grid around the DU 91-W2-250 airfoil

6.3.4 Flow Field Computation

FLUENT is used to solve for the coefficients of lift and drag for a given airfoil. A journal file is used to automatically initialize and evaluate each airfoil while saving a record of the relevant coefficients, C_l and C_d. Temperature and static pressure are defined to be at sea level conditions, 288.16 K and 101325 Pa respectively. These values are quite reasonable for a wind turbine whose maximum altitude does not exceed a few hundred meters. At this temperature and pressure, density is taken to be ρ = 1.225 kg/m^3 and laminar viscosity is taken as μ =1.7894x10^{-5} kg/m*s.

For Flatback airfoils, the flow is assumed to be turbulent with a fixed or free transition point at Reynolds numbers of 666,000 and angle of attack α 10 degree. The FLUENT journal initializes the calculations for a specified Reynolds number of 666,000. The two equation k-ω shear stress transport (SST) is employed in the SOGA while two turbulence models are employed in the MOGA: in addition to the SST model, a three equation transition k-kl-ω model in FLUENT 12.1 is employed. The optimized airfoils results using the two turbulence models are compared with the results for the original non-optimized airfoils. SST model gives good results for flow with "fixed transition" while the k-kl-ω model is more suitable for flow with "free transition".

For DU, FX and NACA airfoils, the angle of attack α is 7.5 degree. The angle of attack, the Reynolds number and all other flow conditions are taken to be exactly the same as given in References [76, 94] from the open literature so that the results for the optimized airfoils could be compared with the existing experimental data available for the baseline airfoils. Since the flow is at low Reynolds number and the airfoils are all thick airfoils with a thickness of at least 16% chord, transitional flow may occur around the airfoils. Therefore, the three equation transition k-kl-ω model is employed in the calculations. The laminar viscosity is calculated from the Sutherland's law:

$$\mu = \mu_0 \left(\frac{T}{T_0} \right)^{3/2} \left(\frac{T_0 + S}{T + S} \right) \tag{6-1}$$

with μ_o = 1.716x10^{-5} kg/m*s, T_o= 273 K, and S=111 K.

6.4 Results and Discussion

In this section, the optimized airfoils using GA are shown and their performance is compared with the original baseline airfoils.

6.4.1 Optimization of Flatback Airfoils

(a) SOGA Results

In this study, our primary objective was to generate optimized flatback airfoils that maximize C_l / C_d at moderate angles-of-attack. We employ a second-order accurate Navier-Stokes solver on an adaptive mesh with a standard pressure solver in FLUENT 12.1.

Figure 6-12 shows the typical "evolution" of an optimized airfoil using the genetic algorithm. In this figure, we plot the best individual objective (C_l /C_d) at each generation against the number of generations. It illustrates the convergence history for C_l /C_d in optimization of FB 3500-0050 airfoil at Re = 666,000 and angle of attack α=10.

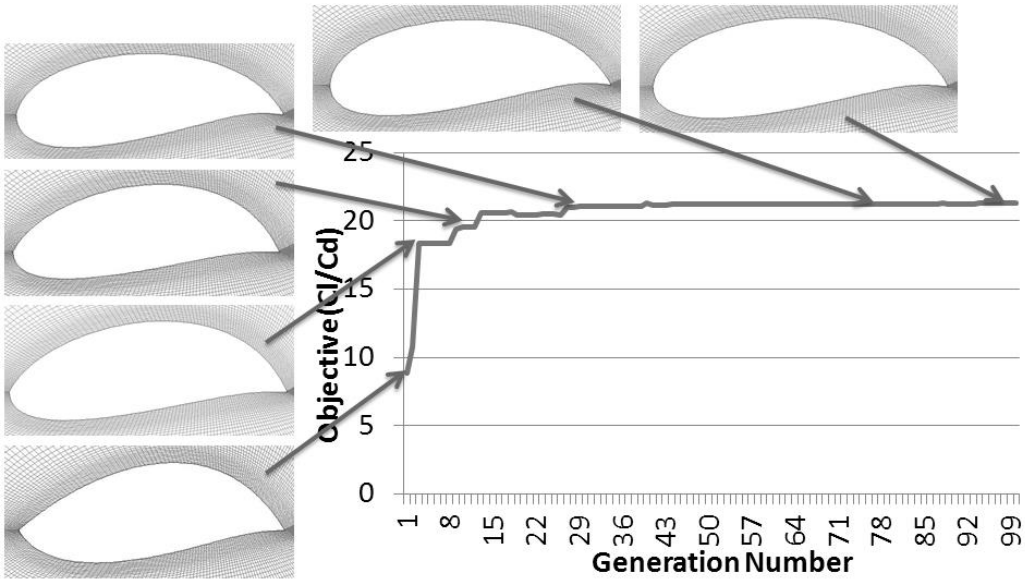

Figure 6-12 Convergence history of optimization for a typical airfoil using the SOGA algorithm

In Figure 6-12, the C_l and C_l / C_d of various airfoils at different generations are as follows. They converge to a value of C_l =1.561 and C_l / C_d = 21.33 in about 100 generations.

Generation 1: C_l =1.041, C_l /C_d = 8.891; Generation 3: C_l =1.469, C_l/ C_d =18.38

Generation 10: C_l = 1.524, C_l/C_d = 19.865; Generation 30: C_l =1.557, C_l/C_d =21.133

Generation 80: C_l =1.558, C_l/C_d =21.238; Generation 98: C_l =1.558, C_l/C_d =21.275

It can be observed from Figure 6-12 that SOGA generates a group of randomly shaped airfoils at the initial generation with a low range of objective values (the best airfoil at 0th generation shown in Figure 6-12 has an objective value (C_l / C_d) below 10). However, the objective of the best airfoil at each generation quickly jumps to a higher value, more than doubling just after two generations. At this stage, the SOGA sorts out the candidate airfoils from the initial generation which either violate the constraints or contribute negatively to the improvement of the objective. As a result, an improved pool of airfoils that makes positive contribution for further improvement of the objective is retained. From generation 3 to generation 30, the best airfoil of each generation further improves the objective value (C_l / C_d); both the objective value and the airfoil shape move towards the final optimized result. It should be noted that there are some fluctuations due to mutation, but they have very minor influence on the general trend. The GA optimization process becomes stable after generation 30 and converges to a value of C_l /C_d = 21.275 after 100 generations. The airfoil shape also converges to a more reasonable shape than the one seen in the initial 0th generation. The convergence at this stage shows that the solution is very likely a global optimal solution. Figure 6-12 together with all other optimization cases studied reveals that SOGA always converges to a value close to the optimization results in only a few generations although the individuals in the 0^{th} generation are randomly created. Although each optimization case may take up to 100 generations to reach convergence, however the results indicate that only a few generations are enough to suggest the final optimized shape and objective value.

Table 6-5 shows the comparison of results between the original baseline Flatback airfoils (shown in Figure 6-1) and the optimized airfoils at Re = 666, 000 and α = 10 degrees. Compared to the original baseline airfoils with fixed transition, the optimized airfoils have larger C_l /C_d, larger C_l and lower C_d. Compared to the original baseline airfoils with free transition, the optimized airfoils have larger C_l and the FB-3500-1750 airfoil also has larger C_l /C_d and lower C_d. The trailing edge thickness of all the optimized airfoils is the same as those of the original baseline airfoils and the maximum thickness is also close to the original airfoils (~ 15%). Figures

6-13, 6-14 and 6-15 show (a) the shape of the optimized airfoil, (b) the pressure distribution on the optimized airfoil, and (c) the velocity contours for the FB-0050, FB-0875, and FB-1750 optimized airfoils respectively.

Table 6-5 Comparison of the performance of the original and optimized flatback airfoils using SOGA

Airfoil	C_l / C_d		
	Optimized (fixed Transition)	**Original(with free transition)**	**Original(with fixed transition)**
FB-0050	23.867	30	4.231
FB-0875	23.750	36	6.129
FB-1750	20.132	14.545	14.545
Airfoil	C_l		
	Optimized(fixed transition)	**Original(with free transition)**	**Original(with fixed transition)**
FB-0050	1.536	1.050	0.550
FB-0875	1.724	1.440	0.760
FB-1750	1.878	1.600	1.600
Airfoil	C_d		
	Optimized(fixed transition)	**Original(with free transition)**	**Original(with fixed transition)**
FB-0050	0.064	0.035	0.130
FB-0875	0.073	0.040	0.124
FB-1750	0.093	0.110	0.110

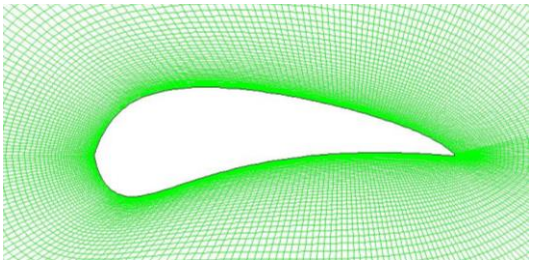

(a) Airfoil Shape

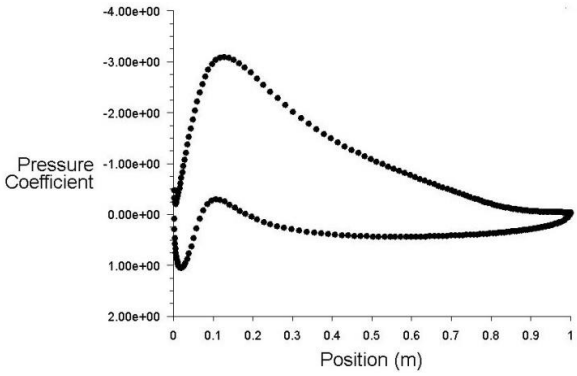

(b) Pressure Distribution

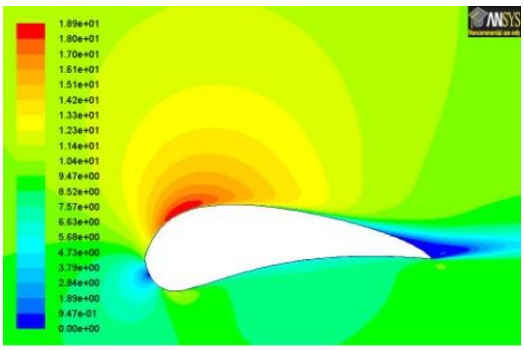

(c) Velocity Contours

Figure 6-13 Results for optimized FB 3500-0050 airfoil, Re = 666,000, α = 10 (free transition)
(a) Airfoil shape (b) Pressure distribution (c) Velocity contours

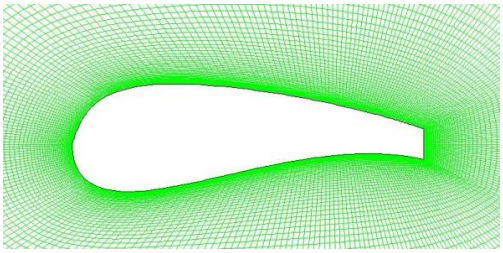

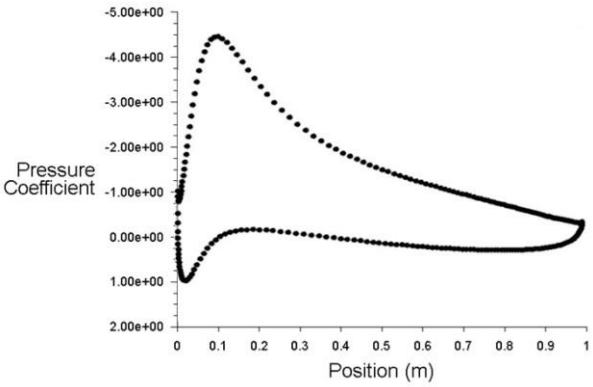

(a) Airfoil Shape (b) Pressure Distribution

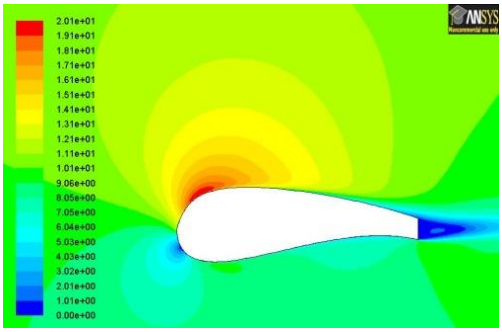

(c) Velocity Contours

Figure 6-14 Results for Optimized FB 3500-0875 Airfoil, Re = 666,000, α = 10 (free transition)
(a) Airfoil shape (b) Pressure distribution (c) Velocity contours

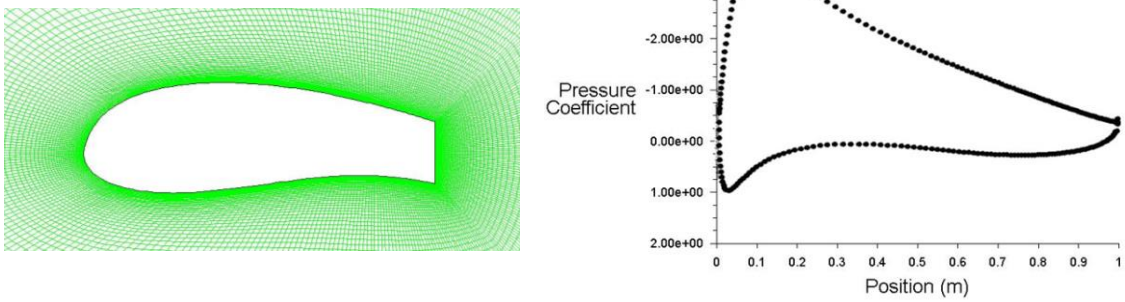

(a) Airfoil Shape (b) Pressure Distribution

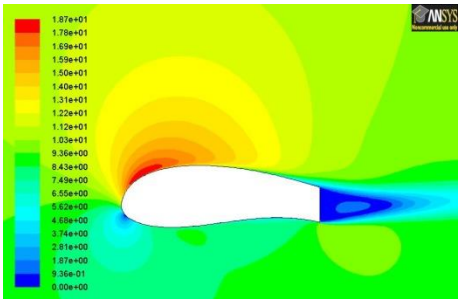

(c) Velocity Contours

Figure 6-15 Results for Optimized FB 3500-1750 Airfoil, Re = 666,000, α = 10 (free transition) (a) Airfoil shape (b) Pressure distribution (c) Velocity contours

Figures 6-16, 6-17 and 6-18 respectively show the comparison of computed C_l and C_d (shown by arrows) for the three original airfoils (with free transition) and optimized airfoils (with fixed transition) at Re = 666,000 and α = 10 with experimental data given for both fixed and free transition in Ref. [73] for (a) lift curves and (b) drag polars. The optimized airfoils have a higher lift coefficient, and for FB-1750 airfoil a lower drag coefficient also (already shown in Table 6-5). These results clearly demonstrate the superior performance of optimized airfoils. However, it is important to note that these airfoils have been optimized for one operating condition. Multipoint optimization is needed to design the best airfoils for practical applications.

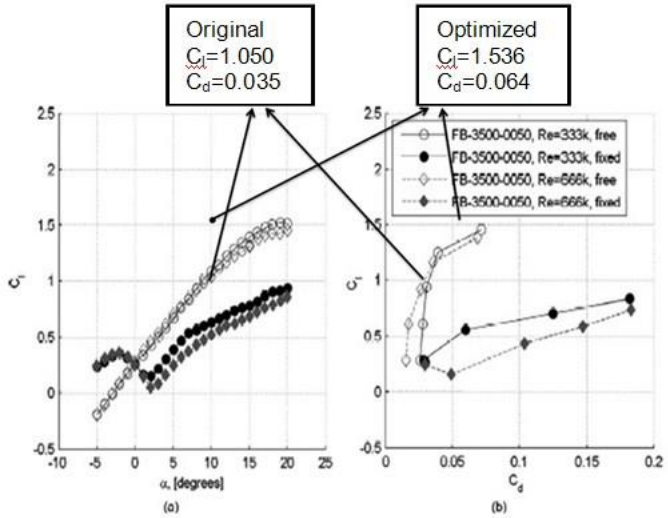

Figure 6-16 Comparison of computed C_l and C_d (shown by arrows) for original FB-3500-0050 airfoil (with free transition) and SOGA-optimized airfoil (with fixed transition) at Re = 666,000 and α = 10 with experimental data reported by Baker et al. [73] for both fixed and free transition for (a) Lift curves and (b) Drag polars

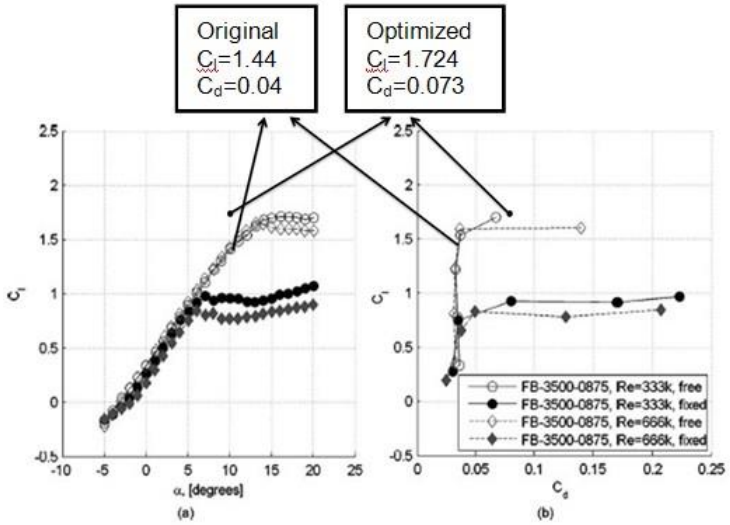

Figure 6-17 Comparison of computed C_l and C_d (shown by arrows) for original FB-3500-0875 airfoil (with free transition) and SOGA-optimized airfoil (with fixed transition) at Re = 666,000 and α = 10 with experimental data reported by Baker et al. [73] for both fixed and free transition for (a) Lift curves and (b) Drag polars

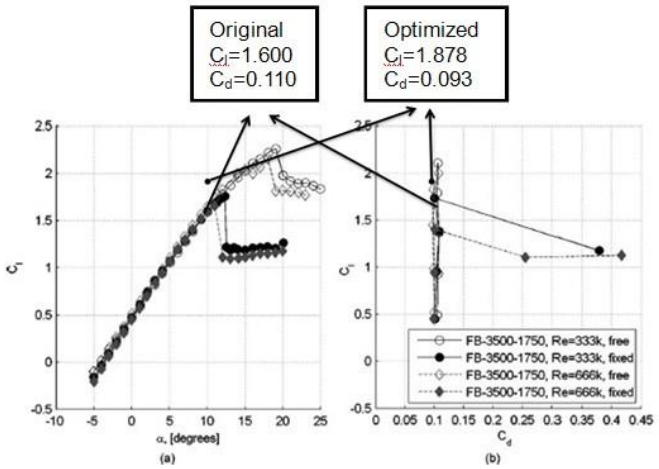

Figure 6-18 Comparison of computed C_l and C_d (shown by arrows) for original FB-3500-1750 airfoil (with free transition) and SOGA-optimized airfoil (with fixed transition) at Re = 666,000 and α = 10 with experimental data reported by Baker et al. [73] for both fixed and free transition for (a) Lift curves and (b) Drag polars

(b) MOGA Results

In this section, results for airfoil shape optimization are presented using the multi-objective genetic algorithm which aims at maximizing both C_l and C_l/C_d. Figure 6-19 shows the comparison of original and optimized FB-0050 airfoil shapes and pressure distributions obtained using MOGA algorithm. Figure 6-20 shows the comparison of original and optimized FB-0875 airfoil shapes and pressure distributions obtained using MOGA algorithm. Figure 6-21 shows the comparison of original and optimized FB-1750 airfoil shapes and pressure distributions obtained using MOGA algorithm. Table 6-6 gives the computed values of C_l, C_d and C_l/C_d for three optimized Flatback airfoils obtained using the SOGA and MOGA with both free and fixed transition.

As shown in Table 6-6, MOGA optimized airfoils with fixed transition further improve the C_l compared to SOGA optimized airfoils with fixed transition. MOGA optimized airfoils using the three-equation k-kl-ω turbulence model in FLUENT 12.1 which can account for the free transition and predicts more accurately the value of C_d; it gives higher value of C_l/C_d and C_l compared to the original FB airfoils with free transition using the k-kl-ω turbulence model. MOGA optimized airfoils also give a lower value of C_d for FB1750 airfoil while maintaining C_d for FB0050 and FB0875 airfoils when compared to the original airfoils. Since the optimization goals for this study are to improve both the C_l/C_d and C_l, small increase in C_d is considered

acceptable. The MOGA results with k-kl-ω turbulence model increase both the C_l /C_d and C_l while decreasing the C_d significantly compared to SOGA results for FB0050 and FB0875 airfoils.

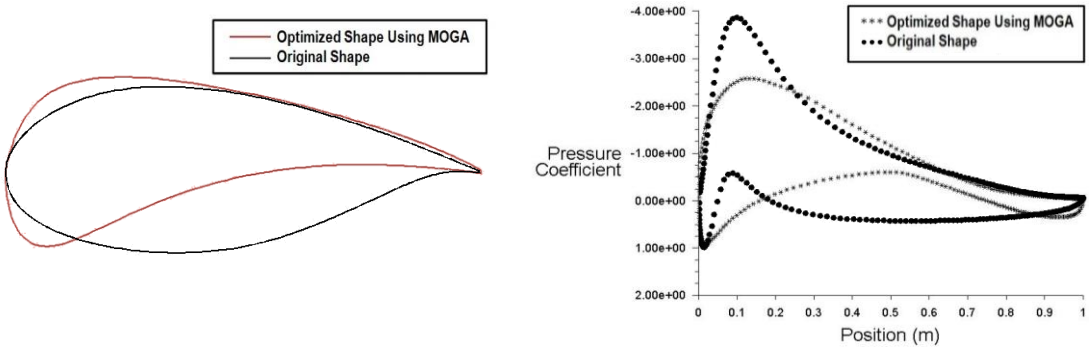

(a) Shape comparison (b) Pressure distribution comparison

Figure 6-19 Comparison of original and optimized FB-0050 (a) Airfoil shapes and (b) Pressure distributions obtained using MOGA algorithm

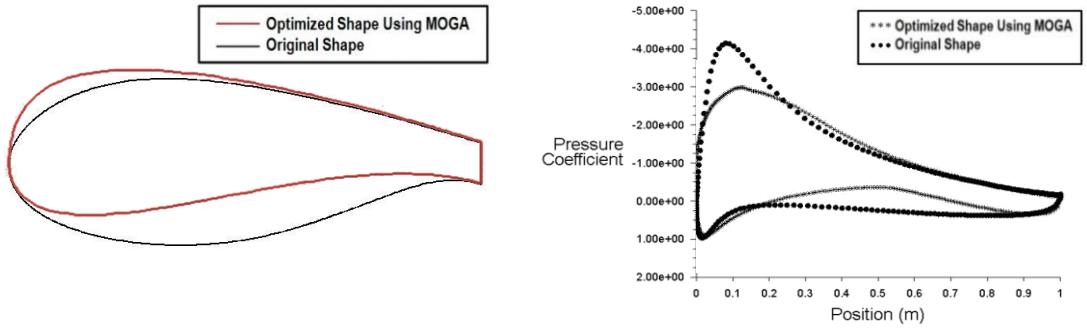

(a) Shape comparison (b) Pressure distribution comparison

Figure 6-20 Comparison of original and optimized FB-0875 (a) Airfoil shapes and (b) Pressure distributions obtained using MOGA algorithm

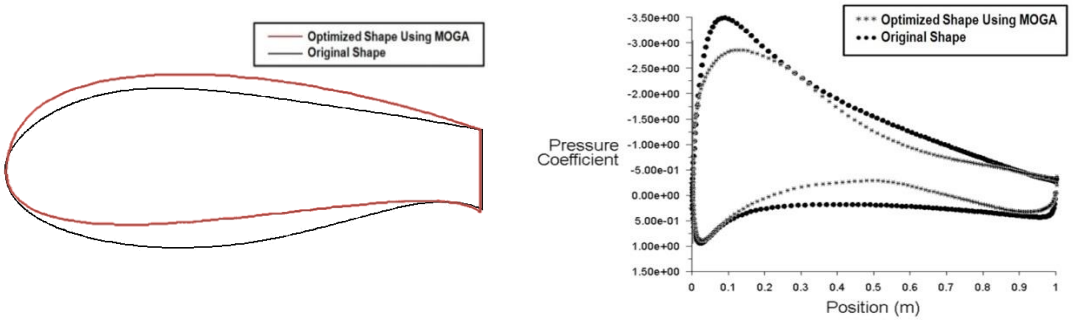

(a) Shape comparison (b) Pressure distribution comparison

Figure 6-21 Comparison of original and optimized FB-1750 (a) Airfoil shapes and (b) Pressure distributions obtained using MOGA algorithm

Table 6-6 Comparison of the performance of optimized and the original flatback airfoils obtained using the SOGA and MOGA

Airfoil		FB-0050	FB-0875	FB-1750
C_l / C_d	**MOGA(k-ω)***	25.052	23.331	19.670
	MOGA(k-kl-ω)**	43.090	37.232	15.879
	SOGA*	23.867	23.750	20.132
	Original**	30	36	14.545
C_l	**MOGA(k-ω)***	1.576	1.848	2.012
	MOGA(k-kl-ω)**	1.862	2.085	2.135
	SOGA*	1.536	1.724	1.878
	Original**	1.05	1.44	1.8
C_d	**MOGA(k-ω)***	0.063	0.079	0.102
	MOGA(k-kl-ω)**	0.043	0.056	0.134
	SOGA*	0.064	0.073	0.093
	Original**	0.035	0.04	0.2

* fixed transition ** free transition

Figure 6-22 shows the convergence history of MOGA for two separate objectives.

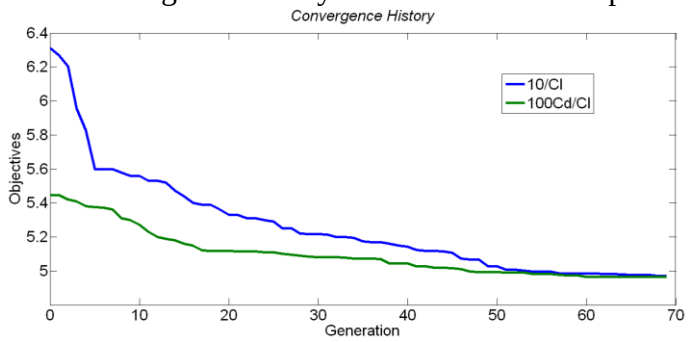

Figure 6-22 Convergence history of MOGA for two separate objectives for FB 1750 airfoil

It should be noted that all the airfoil optimization cases considered in this study are for the attached flow. The GA optimization is stable for attached flows. It is surmised that the optimization will be stable for steady state separated flows. For unsteady flows, it will require a modified strategy for optimization within GA framework which will be investigated in the future work.

As discussed in the previous sections, GA based optimization is quite efficient. It takes less than 100 generations with 20 individuals in each generation to achieve convergence towards an optimized shape. In terms of total computational time required, it is competitive with the adjoint-

based shape optimization approach in computational efficiency; however, it is much simpler to implement especially with multiple-objectives.

6.4.2 Optimization of DU, FX and NACA 64 Airfoils

In this section, our primary objective has been to generate optimized airfoils that maximize both C_l and C_l / C_d at moderate angles-of-attack. We employ a second-order accurate Navier-Stokes solver with a PRESTO! pressure solver in FLUENT. The coupled scheme is applied for pressure-velocity coupling. The solution dependence on mesh size is investigated to make sure that the solution is meshing independent.

Figure 6-23 shows the typical "evolution" of an optimized airfoil using the genetic algorithm. In this figure, we plot the best objective 2 ($100C_d/C_l$) in each generation against the generation number. It illustrates the convergence history for a C_l / C_d - optimized DU 91-W2-250 airfoil at Re = 1e6 and α = 7.5. It should be noted that the solution is nearly optimal after about 80 evaluations.

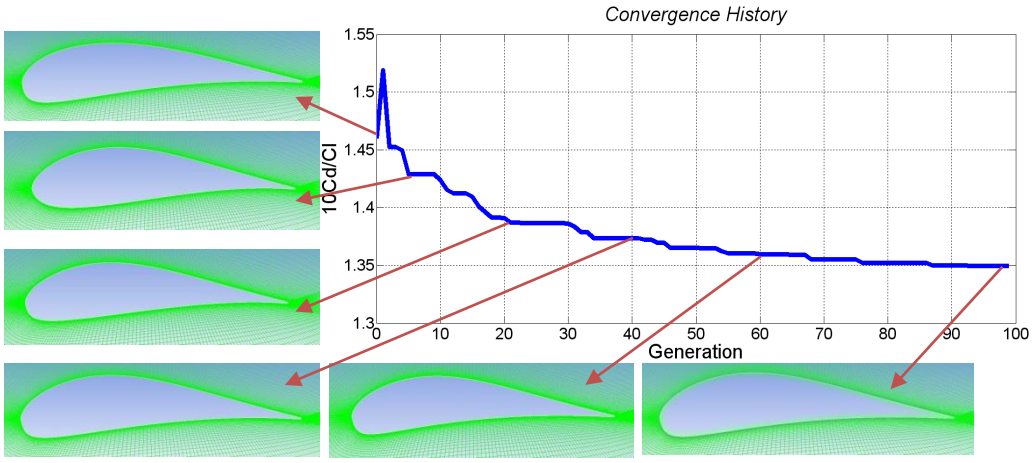

Figure 6-23 Convergence history of a typical optimized airfoil using GA algorithm

In Figure 6-23, the C_l and C_l / C_d of various airfoils at different generations are as follows. They converge to a value of C_l = 1.5569 and C_l / C_d =74.0676 after about 90 generations.

Generation 0: C_l =1.4616, C_l/C_d =68.5041, Generation 6: C_l =1.5291, C_l/C_d =69.9895, Generation 21: C_l =1.5486, C_l/C_d =72.1038, Generation 40: C_l =1.5593, C_l/C_d =72.8106,

Generation 60: C_l =1.5541, C_l/C_d =73.5484, and Generation 99: C_l =1.5569, C_l/C_d =74.0676

Table 6-7 shows the comparison of results between the original airfoils (Figure 6-2, 6-3, 6-4) and the optimized airfoils at specified Re as shown and α = 7.5 degrees. For all the four airfoils, the optimized airfoils have larger C_l / C_d and larger C_l . The maximum thickness is also close to the original airfoils (~ 20%). These results clearly demonstrate the superior performance of optimized airfoils.

Table 6-7 Comparison of results for original and optimized FX DU and NACA airfoils

Airfoil	**Maximum Thickness**	C_l / C_d		C_l		C_d		**Re**
		optimized	**original**	**optimized**	**original**	**optimized**	**original**	
FX 66-S-196 V1	0.173	95.3392	94.286	1.4053	1.32	0.01474	0.0147	1.5e6
DU 91-W2-250	0.233	74.0676	68.333	1.5569	1.23	0.02102	0.018	1e6
NACA 64418	0.163	95.4725	90.77	1.3285	1.18	0.01392	0.013	6e6
NACA 64421	0.194	94.5107	85	1.4428	1.19	0.01527	0.014	3e6

Figures 6-24, 6-25, 6-26 and 6-27 shows (a) the optimized shape, (b) the pressure distribution, and (c) the velocity contours for the optimized FX 66-S-196 V1, DU 91-W2-250, NACA 64418 and NACA 64421 airfoils respectively.

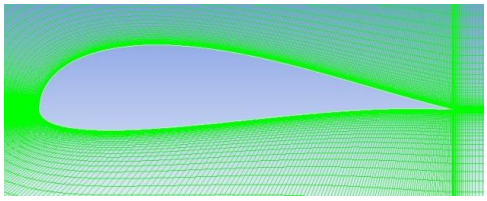

(a) Airfoil Shape

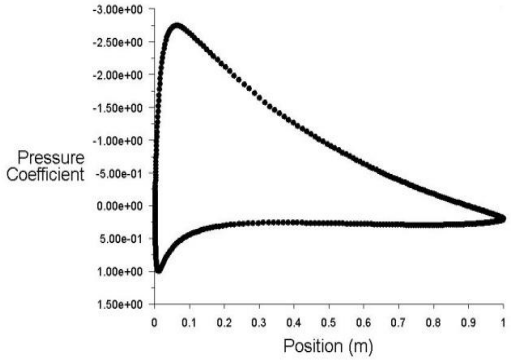

(b) Pressure Distribution

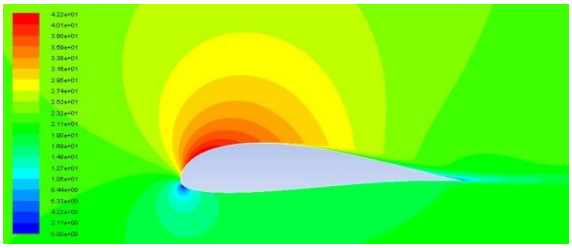

(c) Velocity Contours (Zoomed-in View)

Figure 6-24 Results for optimized FX 66-S-196 V1 airfoil, Re = 1.5e6, α = 7.5 degree

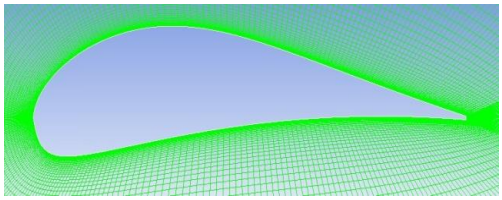

(a) Airfoil Shape

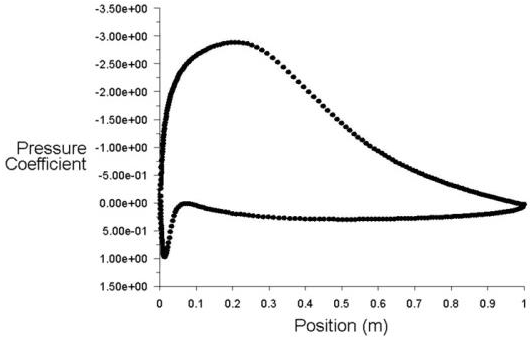

(b) Pressure Distribution

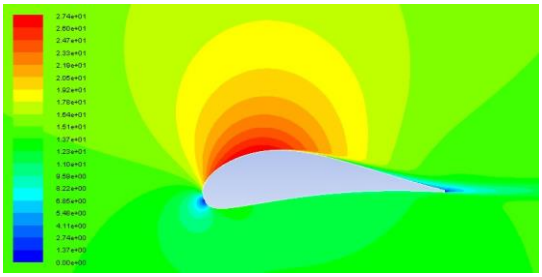

(c) Velocity Contours (Zoomed-in View)

Figure 6-25 Results for optimized DU 91-W2-250 airfoil, Re = 3e6, α = 7.5 degree

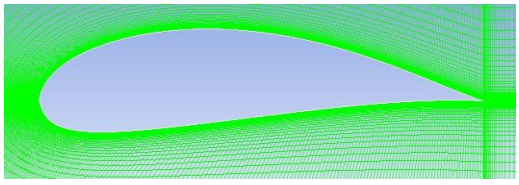

(a) Airfoil Shape

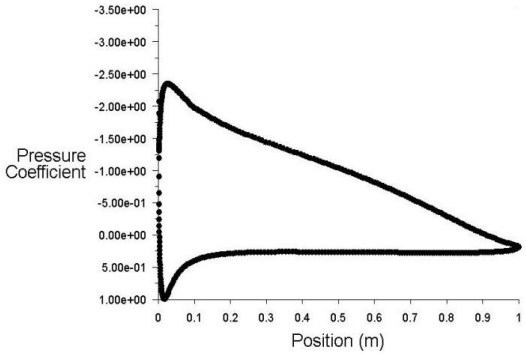

(b) Pressure Distribution

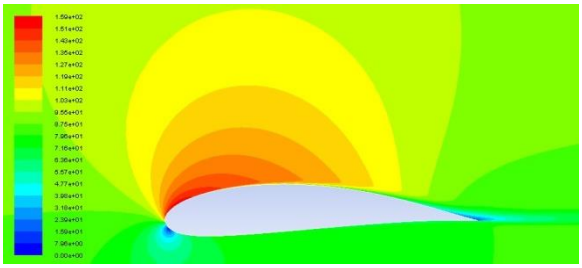

(c) Velocity Contours (Zoomed-in View)

Figure 6-26 Results for optimized NACA 64418 airfoil, Re = 3e6, α = 7.5 degree

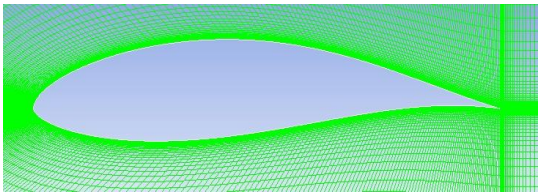

(a) Airfoil Shape

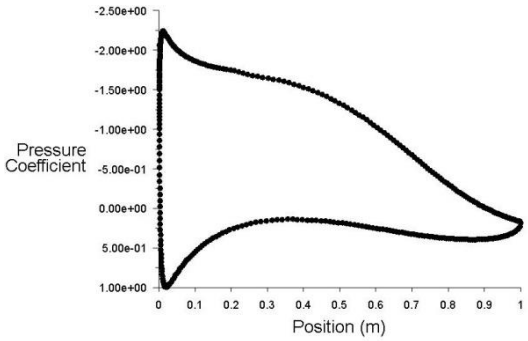

(b) Pressure Distribution

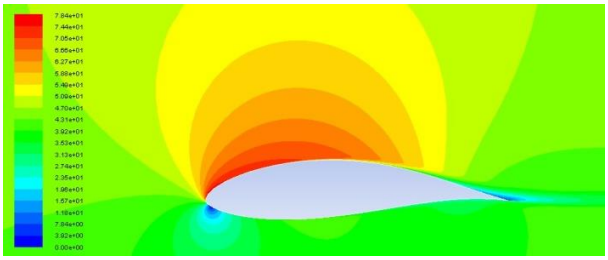

(c) Velocity Contours (Zoomed-in View)

Figure 6-27 Results for optimized NACA 64421 airfoil, Re = 3e6, α = 7.5 degree

Figures 6-28, 6-29, 6-30 and 6-31 shows the comparison of optimized and original airfoil shapes and pressure distributions for FX 66-S-196 V1, DU 91-W2-250, NACA 64418 and NACA 64421 airfoils obtained using MOGA respectively.

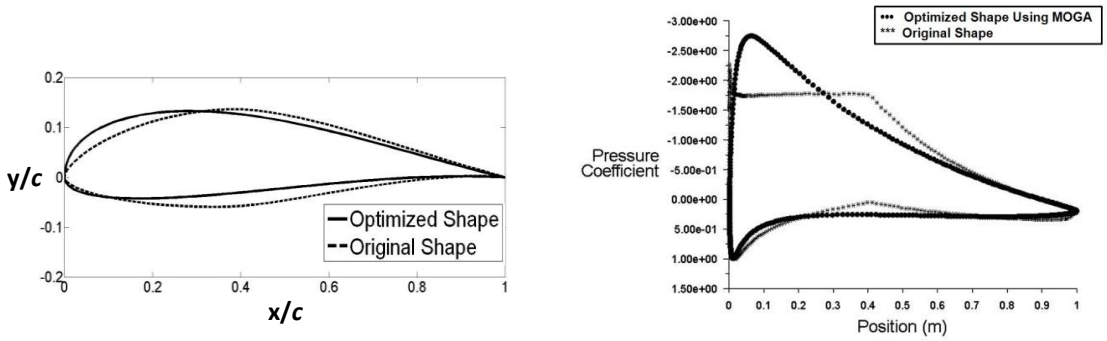

(a) Airfoil Shape Comparison (b) Pressure Distribution Comparison

Figure 6-28 Comparison of original and optimized FX 66-S-196 V1 airfoil shapes and pressure distributions obtained using MOGA algorithm

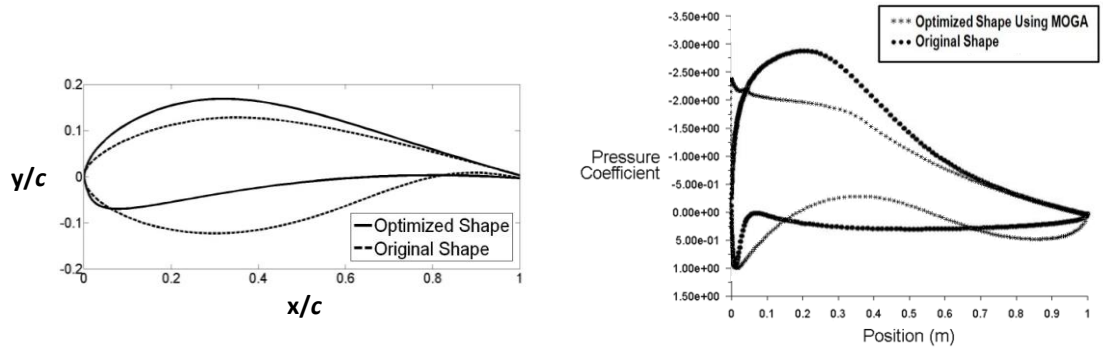

(a) Airfoil Shape Comparison (b) Pressure Distribution Comparison

Figure 6-29 Comparison of original and optimized DU 91-W2-250 airfoil shapes and pressure distributions obtained using MOGA algorithm

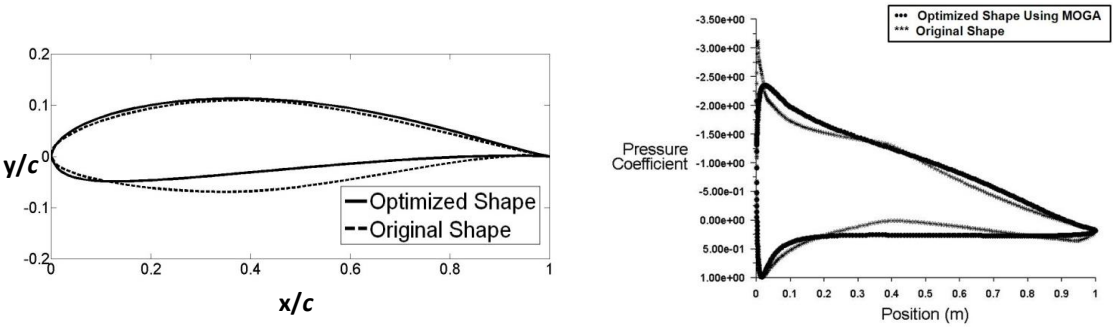

(a)Airfoil Shape Comparison (b) Pressure Distribution Comparison

Figure 6-30 Comparison of original and optimized NACA 64418 airfoil shapes and pressure distributions obtained using MOGA algorithm

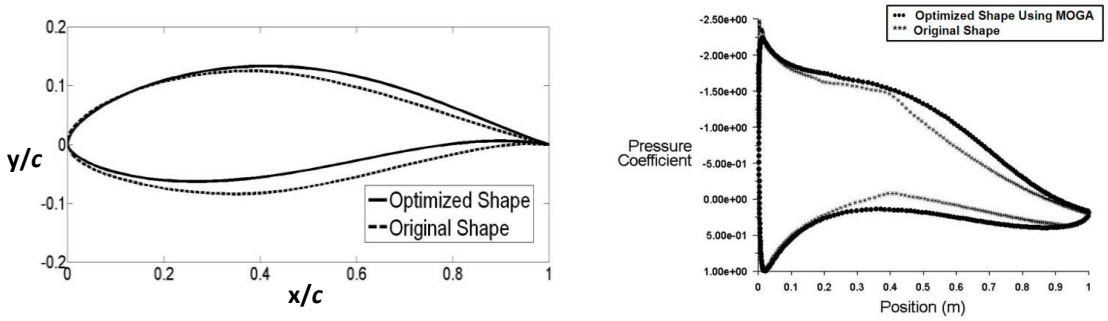

(a) Airfoil Shape Comparison (b) Pressure Distribution Comparison

Figure 6-31 Comparison of original and optimized NACA 64421 airfoil shapes and pressure distributions obtained using MOGA algorithm

Chapter 7 Blade Element Momentum Theory (BEM) for Wind Turbine Applications

7.1 Overview

This chapter focuses on evaluation of the performance of 3D wind turbine blades using analysis methods based on Blade Element Momentum Theory. There are two parts in this study. The first part is to assess the performance of various airfoil sections on power generation from a wind turbine. The second part is to capture the dynamic behavior of wind turbines due to the existence of wind turbine wake by adding a simplified dynamic inflow model to the basic BEM method [95].

Because of recent emphasis on carbon free renewable energy, there has been great deal of research directed towards the design of aerodynamically efficient wind turbines. There are mainly two kinds of wind turbines: Horizontal –Axis Wind Turbines (HAWT) and Vertical-Axis Wind Turbines (VAWT). Between them, HAWTs are the most commercially deployed turbines all over the world since they are able to generate more electricity at a given wind speed, especially in large wind farm applications when the wind is intermittent [96]. This study focuses on improving the HAWT performance by changing the blade airfoil sections while the chord length and the twist angle along the blade span are kept fixed.

In order to calculate the wind turbine power, a Java-based aerodynamic analysis tool using Blade Element Momentum Theory has been developed based on Ceyhan's method [20]. The BEM analysis tool is validated against the field test data and Ceyhan's BEM results for two wind turbines: NREL (National Renewable Energy Laboratory, USA) Phase II and III wind turbines. The NREL Phase II wind turbine has an untwisted and un-tapered blade while the NREL Phase III wind turbine has a twisted and un-tapered blade. Validations are performed to show the

capabilities of our BEM analysis tool. The developed BEM tool is accurate and efficient in calculating the wind turbine performance based on comparisons with the test data.

The airfoil sections used in this study are thick airfoils. They were used as the baseline airfoils for shape optimization using genetic algorithms in previous studies by the authors because of their aerodynamic and structural advantages [23] as described in Chapter 6. In this study we employ FB series (FB-3500-0050, FB-3500-0875, FB-3500-1750) [73], FX 66-S196-V1 [74], DU 91-W2-250 [75] and NACA 64421 [76] airfoils. Their aerodynamic characteristics including C_l and C_d are collected and expanded to a wider range of angles of attack for BEM calculation. The wind power calculation results for blades with these airfoil sections are compared with the original NREL Phase II, Phase II and Risoe wind turbines. It is shown that thick airfoil sections can increase the wind turbine power by as much as 100 percent.

The inclusion of simplified dynamic inflow model makes it possible to conduct simulations of the wind turbine performance in a large time scale when the operating conditions may change. This study focuses on the starting stage of the original NREL Phase II, Phase II and Risoe wind turbines at free wind speed of 12 m/s. By comparing with the results from the basic BEM method, the inclusion of a simplified dynamic inflow model in BEM code has demonstrated its capability in capturing the instant behavior of the wind turbines.

7.2 Blade Element Momentum Theory

This study employs Blade Element Momentum Theory for calculation of power output of a HAWT. The BEM theory models the axial (or normal) and tangential induction factors by equating the force and torque relations for a small ring in the turbine plane (modeled as an actuator disk) derived from either the momentum theory or the blade element theory [20].

7.2.1 Momentum Theory

In the momentum theory, we consider the stream tube surrounding the wind turbine which is modeled as an actuator disc as shown in Figure 7-1. Assuming steady, uniform, axisymmetric incompressible, inviscid flow with a nonrotating wake, the mass conservation in the stream tube gives the following relation:

$$\rho U_1 A_1 = \rho U_2 A_d = \rho U_4 A_4 \tag{7-1}$$

where A_d is area of the actuator disk.

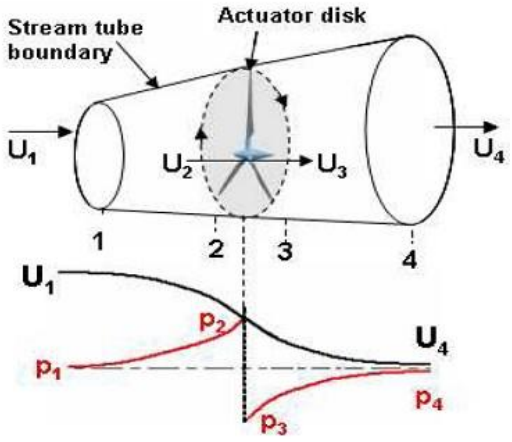

Figure 7-1 Actuator disk model of a wind turbine [20]

Since the actuator disc induces velocity in the stream tube, an axial induction factor a is defined as:

$$a = \frac{U_1 - U_2}{U_1} \tag{7-2}$$

Thus, we have

$$U_2 = U_1(1-a) \tag{7-3}$$

$$U_4 = U_1(1-2a) \tag{7-4}$$

Applying the Bernoulli equations to point 1, 2 and 3, 4, we can derive the following expression for pressure difference across the actuator disk:

$$p_2 - p_3 = \frac{1}{2}\rho(U_1^2 - U_4^2) \tag{7-5}$$

Thus, the net force normal to the plane on a ring of width *dr* in the actuator disk can be calculated as:

$$dF = (p_2 - p_3)dA_d = 4\rho U_1^2 a(1-a)\pi r dr \qquad (7\text{-}6)$$

Now, we consider the rotating annular stream tube shown in Figure 7-2.

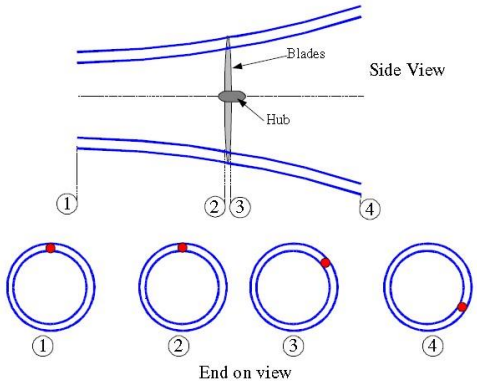

Figure 7-2 Rotating annular stream tube [20]

Define an angular induction factor *a* ´as:

$$a' = \frac{\omega}{2\Omega} \qquad (7\text{-}7)$$

where ω is the angular velocity of the blade wake and Ω is the angular velocity of the blade. For a small element *dr*, the corresponding torque is given by:

$$dQ = \rho 2\pi r dr U_2 \omega r^2 \qquad (7\text{-}8)$$

Together with (7-7), the torque is calculated as:

$$dQ = 4a'(1-a)\rho U_1 \Omega r^3 \pi dr \qquad (7\text{-}9)$$

7.2.2 Blade Element Theory

In the blade element theory, the blade is assumed to be divided into *N* sections which are called the blade elements. It is assumed that there is zero aerodynamic interaction between the blade elements and there is negligible spanwise velocity component on the blade. The forces on the blade element are solely determined by the lift and drag characteristics of 2D airfoils of the blade element; lift and drag components are defined perpendicular and parallel to the relative wind

speed direction. The total tangential velocity experienced by the blade element is (1+ a') Ωr and the axial velocity is (1- a) U_∞. The relative wind velocity at the blade is given by:

$$W = \frac{U_\infty(1-a)}{\sin\phi} \tag{7-10}$$

The angle between the relative wind velocity and the plane of rotation is given by:

$$\tan\phi = \frac{U_\infty(1-a)}{\Omega r(1-a')} = \frac{(1-a)}{(1-a')\lambda_r} \tag{7-11}$$

where λ_r is the local tip speed ratio.

The net force normal to the plane of rotation for each blade element and the resulting torque on each blade element can be written as:

$$dF = dL\cos\phi + dD\sin\phi \tag{7-12}$$

$$dQ = r(dL\sin\phi - dD\cos\phi) \tag{7-13}$$

where dL and dD are the lift and drag forces on the blade elements respectively. They are defined as:

$$dL = C_L\frac{1}{2}\rho W^2 c dr \tag{7-14}$$

$$dD = C_D\frac{1}{2}\rho W^2 c dr \tag{7-15}$$

For a multi-bladed wind turbine with ***B*** number of blades, one can write:

$$dF = B\frac{1}{2}\rho W^2(C_L\cos\phi + C_D\sin\phi)c dr \tag{7-16}$$

$$dQ = B\frac{1}{2}\rho W^2(C_L\sin\phi - C_D\cos\phi)cr dr \tag{7-17}$$

Defining the local solidity as $\sigma' = \frac{Bc}{2\pi r}$ and replacing W with equation (7-10), equations (7-16) and (7-17) become:

$$dF = \sigma'\pi\rho\frac{U_\infty^2(1-a)^2}{\sin^2\phi}(C_L\cos\phi + C_D\sin\phi)r dr \tag{7-18}$$

$$dQ = \sigma'\pi\rho\frac{U_\infty^2(1-a)^2}{\sin^2\phi}(C_L\sin\phi - C_D\cos\phi)r^2 dr \tag{7-19}$$

7.2.3 Tip Loss Correction and Modified BEM Theory

The original BEM theory does not include 3D characteristics of the flow and viscous losses due to separation and turbulence. Some modification needs to be applied to the theory to take into account these losses. The modified BEM theory includes the tip-loss and Glauert corrections [20]. The tip-loss model serves to correct the induced velocity resulting from the vortices shed from the blade tips into the wake on the induced velocity field while the hub-loss model corrects the induced velocity resulting from a vortex being shed near the hub of the rotor [20]. These losses are calculated as:

$$F_{tip} = \frac{2}{\pi}\cos^{-1}\left(\exp\left(-\frac{B}{2}\frac{R-r}{r\sin\phi}\right)\right) \tag{7-20}$$

$$F_{hub} = \frac{2}{\pi}\cos^{-1}\left(\exp\left(-\frac{B}{2}\frac{r-r_{hub}}{r_{hub}\sin\phi}\right)\right) \tag{7-21}$$

The net tip loss is given by

$$F = F_{tip} * F_{hub} \tag{7-22}$$

The Glauert empirical relation with a modification for the tip loss factor is given as:

$$C_T = \frac{8}{9} + (4F - \frac{40}{9})a + (\frac{50}{9} - 4F)a^2$$

$$a = \frac{18F - 20 - 3\sqrt{C_T(50-36F) + 12F(3F-4)}}{30F - 50} \tag{7-23}$$

After considering tip loss and Glauert correction, we have four equations - (7-24) and (7-25) derived from the momentum theory and (7-26) and (7-27) obtained from blade element theory:

$$dF = 4F\rho U_1^2 a(1-a)\pi r dr \tag{7-24}$$

$$dQ = 4Fa'(1-a)\rho U_1 \Omega r^3 \pi dr \tag{7-25}$$

$$dF = \sigma'\pi\rho\frac{U_\infty^2(1-a)^2}{\sin^2\phi}(C_L\cos\phi + C_D\sin\phi)r dr \tag{7-26}$$

$$dQ = \sigma'\pi\rho\frac{U_\infty^2(1-a)^2}{\sin^2\phi}(C_L\sin\phi - C_D\cos\phi)r^2 dr \tag{7-27}$$

By equating the force relation (7-24) and (7-26) and torque relation (7-25) and (7-24), the axial induction factor a and the angular induction factor a' can be calculated. The process to

calculate the induction factors is an iterative process shown in Figure 7-3. When the iteration converges, the induction factors can be determined and are then used to calculate the angles of attacks and thrust for each blade element separately for the wind turbine performance analysis. The total power from the rotor is given by:

$$P = \int_{rh}^{R} dP = \int_{rh}^{R} \Omega dQ \tag{7-28}$$

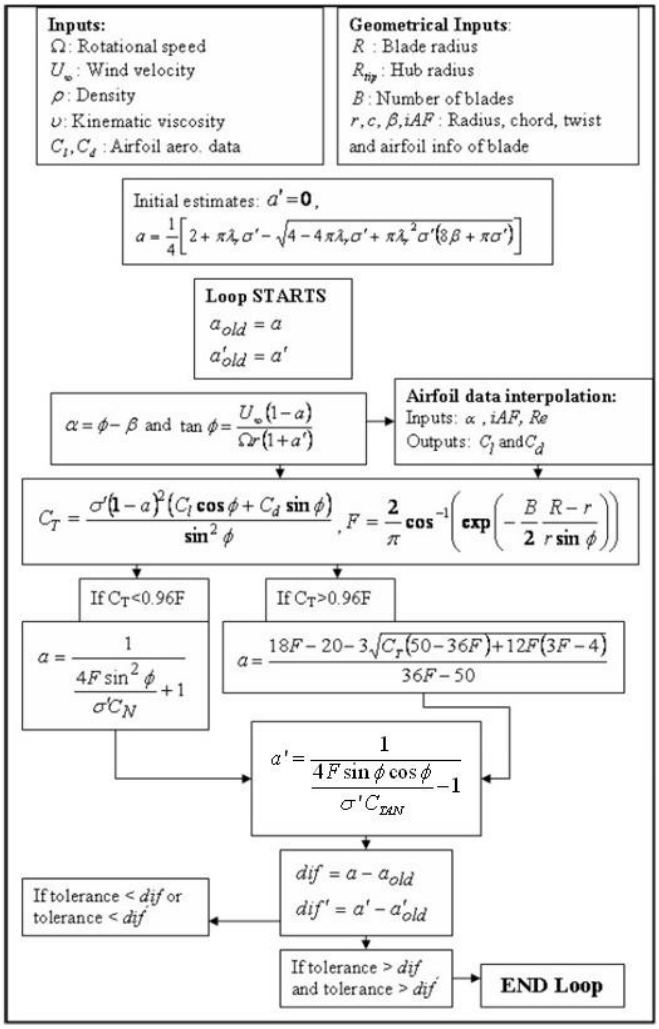

Figure 7-3 Iterative procedure for induction factors calculation

7.3 Simplified Dynamic Inflow Aerodynamic Model

The BEM Theory discussed in section 7.3 is the basic BEM Theory. It describes the steady state values of the induction factors and the aerodynamic coefficients C_P and C_T. The aerodynamic model applied to the basic BEM Theory is named as the quasi-steady aerodynamic model, which assumes instant equilibrium of the wake when conditions change [95]. Therefore, the axial induction factor a and the angular induction factor a' are also denoted as a_n^{qs} and a_t^{qs}. For a_n^{qs}, 'n' denotes 'normal' meaning that it's the induction factor of the normal induced velocity to the rotor plane. For a_t^{qs}, 't' denotes 'tangential' meaning that it's the induction factor of the tangential induced velocity. The corresponding induced velocities are assumed to settle to their stationary values instantly [95], which can described in the following way:

$$v_n(r) = V_{rel} a_n^{qs}(\lambda, \theta, r) \tag{7-29}$$

$$v_t(r) = V_{rel} a_t^{qs}(\lambda, \theta, r) \tag{7-30}$$

A more realistic aerodynamic model is introduced in this section to capture the behavior of the wake behind an operating wind turbine; it is a simple dynamic inflow aerodynamic model. Due to the existence of the wind turbine wake, the aerodynamic forces always settle to their new steady-state values after the wake settles to a new equilibrium whenever changes in operating conditions occur [95]. In this simplified dynamic inflow model, the tangential induced wind speeds are assumed to be quasi-steady, and thus the induced tangential wind speed states $v_t(r)$. The normal induced wind speed states $v_n(r)$ are computed from a single averaged induced normal wind speed state $\bar{v}_n(t)$ with the temporal dynamics:

$$\tau_1 \dot{\bar{v}}_n + \bar{v}_n = V_{rel} \bar{a}_n^{qs}(\lambda, \theta) \tag{7-31}$$

where the time constant τ_1 satisfies:

$$\tau_1 = \frac{1}{2} \frac{1.1R}{V_{rel} - 1.3\bar{v}_n} \tag{7-32}$$

where R is turbine radius, V_{rel} is relative wind speed normal to the rotor plane.

Solving equation (7-31) with the initial condition $\bar{v}_n(0) = 0$ gives the following solution:

$$\bar{v}_n(t) = \frac{V_{rel}\bar{a}_n^{qs}(\lambda,\theta) - \dfrac{10V_{rel}\beta(t)}{13}}{\beta(t)-1} \tag{7-33}$$

where

$$\beta(t) = \exp\left\{V_{rel}(13\bar{a}_n^{qs}(\lambda,\theta)-10)\left[\frac{2t}{11R} + \frac{\ln\left(1.3\bar{a}_n^{qs}(\lambda,\theta)\right)}{V_{rel}(13\bar{a}_n^{qs}(\lambda,\theta)-10)}\right]\right\} \tag{7-34}$$

The induced normal wind speed states $v_n(r)$ can then be obtained in the following way:

$$v_n(r) = \frac{a_n^{qs}(\lambda,\theta,r)}{\bar{a}_n^{qs}(\lambda,\theta)}\bar{v}_n, \bar{a}_n^{qs}(\lambda,\theta) > 0 \tag{7-35}$$

where

$$\bar{a}_n^{qs}(\lambda,\theta) = \frac{1}{R}\int_0^R a_n^{qs}(\lambda,\theta,r)dr \tag{7-36}$$

This assumption is valid if the dynamic and quasi-steady distributions along the blade do not change too much when moving from one point of operation to another point of operation with changing wind condition.

Because the tangential induced wind speeds are assumed to be quasi-steady and the normal induced wind speed states $v_n(r)$ also depend on a_n^{qs}, the calculation with the inflow model follows the basic BEM procedure shown Figure 7-3, after all the quasi-steady induction factors are computed. Figure 7-4 shows the additional code for simplified inflow model that is included in the original quasi-steady BEM code for evaluation of the wind turbine performance. Figure 7-3 and 7-4 together form the complete procedure for the assessment of wind turbine performance using BEM theory with a simplified dynamic inflow model.

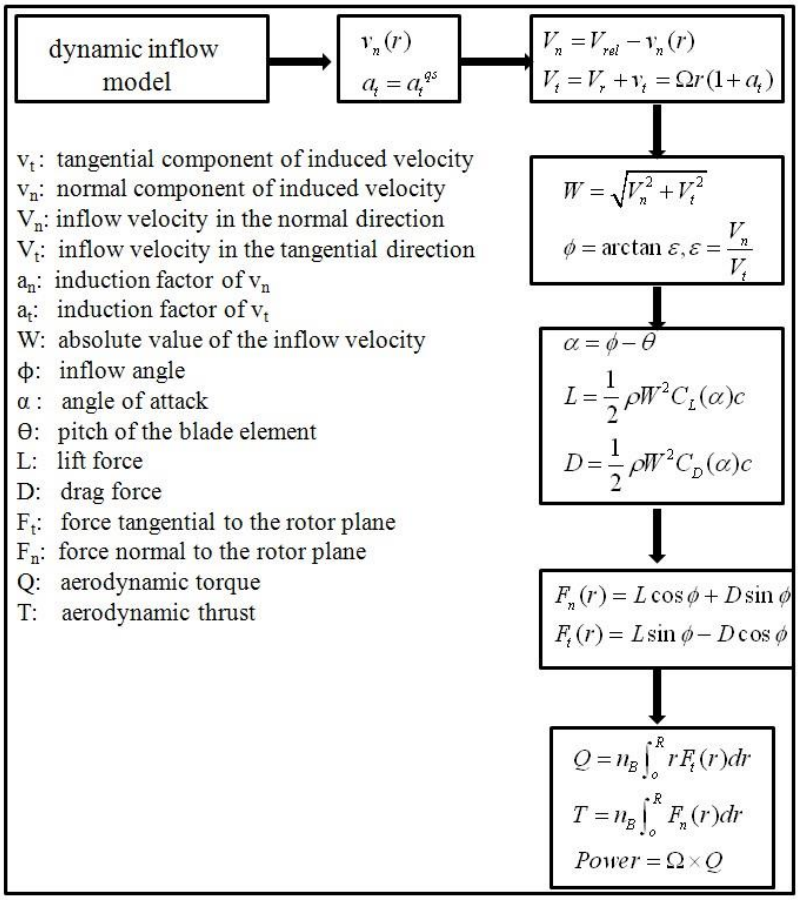

Figure 7-4 Evaluation procedure for dynamic inflow model calculation

7.4 Airfoil Data Preparation

As shown in the BEM iteration process in Figure 7-3 for induction factors calculation, aerodynamic characteristics (C_l and C_d) of airfoils are needed to determine the thrust coefficient C_T. This study employs the airfoils shapes including S809 [20], FB series (FB-3500-0050, FB-3500-0875, FB-3500-1750), FX 66-S196-V1, DU 91-W2-250 and NACA 64421 airfoils. Their experimental data are available in the open literature for a range of angles-of-attack (usually from -5 to 15 degrees) and Reynolds numbers [73, 76, 94]. However, in the actual operation of a wind turbine, the blades experience very high angle-of-attack regimes. The currently available data needs to be expanded to cover high angles-of -attack regimes. This study uses Viterna's method in AirfoilPrep v2.2 developed by NREL [20] as the extrapolation tool to construct the C_l

and C_d data between -180 and +180 degrees of angles of attack. The Reynolds numbers are chosen as some appropriate fixed numbers. Figure 7-5 shows an example of airfoil data extrapolation for DU 91-W2-250 airfoil.

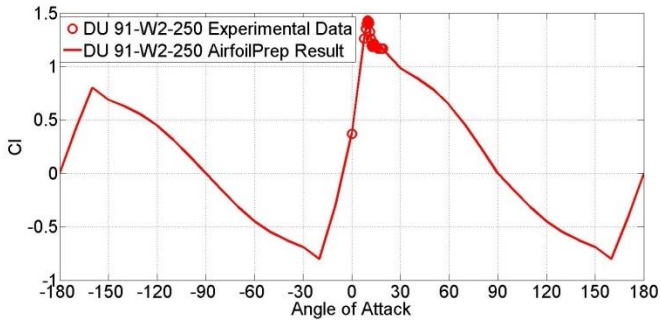

(a) Lift coefficient C_l

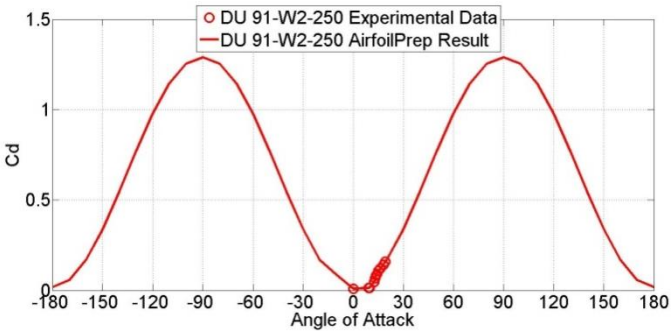

(b) Drag coefficient C_d

Figure 7-5 Airfoil data extrapolation compared with the available experimental data

7.5 Results and Discussion

7.5.1 Validation of BEM Analysis Tool

Before calculating the wind turbine power using thick airfoils, BEM code validations are performed to assess its accuracy and efficiency. Three different wind turbines are employed in the validation process. The calculated results are compared with the experimental data in Reference [20] and the BEM results of Ceyhan [20]. The first validation case is for the NREL

untwisted and un-tapered blade wind turbine known as the NREL Phase II wind turbine. The wind turbine employs S809 airfoil section along the blade without any twist and taper. The operating conditions and geometrical properties are shown in Table 7-1 and Figure 7-6. The second validation case is the NREL twisted and un-tapered wind turbine called NREL Phase III wind turbine. It adds some twist to the turbine blade along the blade span. Table 7-2 and Figure 7-7 show the operating conditions and geometrical properties. The third validation case is the Risoe wind turbine. This wind turbine has both twist and taper in the blades. In Risoe wind turbine, NACA 63-2xx series airfoils are used. Table 7-3 and Figure 7-8 show the operating conditions and geometrical properties of Risoe wind turbine.

Table 7-1 NREL Phase II wind turbine general characteristics

Number of Blades	3
Turbine Diameter	10.06 m
Rotational Speed	71.3 rpm
Cut-in Wind Speed	6 m/s
Control	Stall Control
Rated Power	19.8 kW
Root Extension	0.723 m
Blade Set Angle	12 degrees
Twist	None
Chord	0.4572@all span location
Airfoil	S809

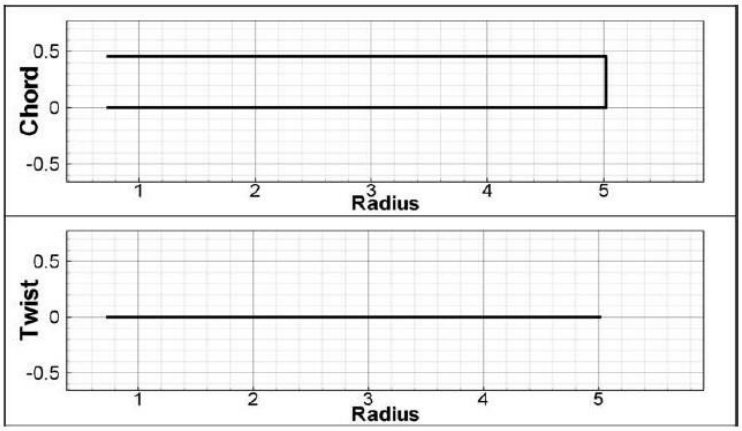

Figure 7-6 Geometric properties of NREL Phase II wind turbine

Table 7-2 NREL Phase III wind turbine general characteristics

Number of Blades	3
Turbine Diameter	10.06 m
Rotational Speed	71.3 rpm`
Cut-in Wind Speed	6 m/s
Control	Stall Control
Rated Power	19.8 kW
Root Extension	0.723 m
Blade Set Angle	3 degrees
Twist	44 degrees (max.)
Chord	0.4572@all span location
Airfoil	S809

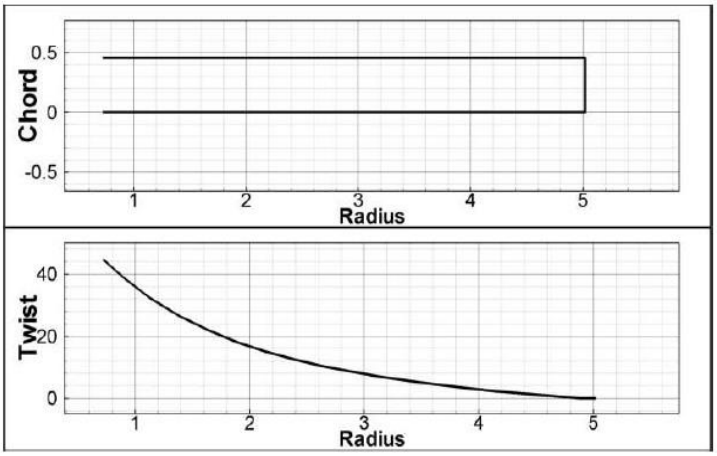

Figure 7-7 Geometric properties of NREL Phase III wind turbine

Table 7-3 Risoe wind turbine general characteristics

Number of Blades	3
Turbine Diameter	19.0 m
Rotational Speed	35.6 and 47.5 rpm`
Cut-in Wind Speed	4 m/s
Control	Stall Control
Rated Power	100 kW
Root Extension	2.3 m
Blade Set Angle	1.8 degrees
Twist	15 degrees (max.)
Root Chord	1.09 m
Tip Chord	0.45 m
Airfoil	NACA 63-2xx series

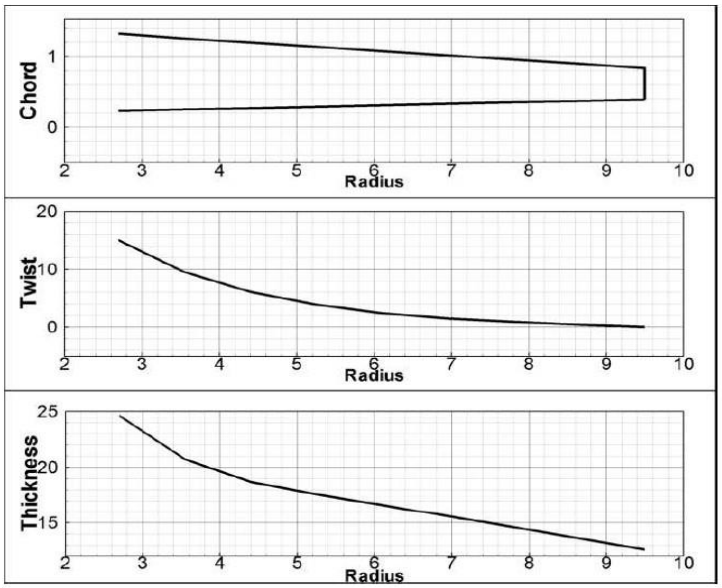

Figure 7-8 Geometric properties of Risoe wind turbine

Figure 7-9, 7-10 and 7-11 show the comparison of results among NREL Phase II, NREL Phase III and Risoe wind turbines. These three figures show that the BEM analysis tool employed in this study performs quite well in matching the experimental data for a wide range of wind speeds, especially at high wind speeds (greater than 8 m/s). The improvement in comparisons between the test data and computations at small wind speeds (lower than 8 m/s) requires more accurate C_L and C_D data. Considering that most large scale wind turbines operate at high wind speed, the validation results are acceptable and the BEM analysis tool can be considered as a good code to estimate the power output from a wind turbine using thick airfoils mentioned before.

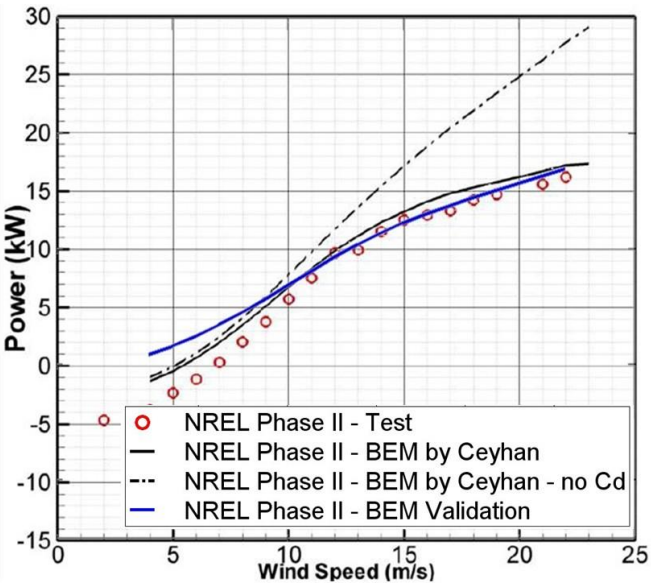

Figure 7-9 Comparison of BEM calculations with test data for NREL Phase II wind turbine

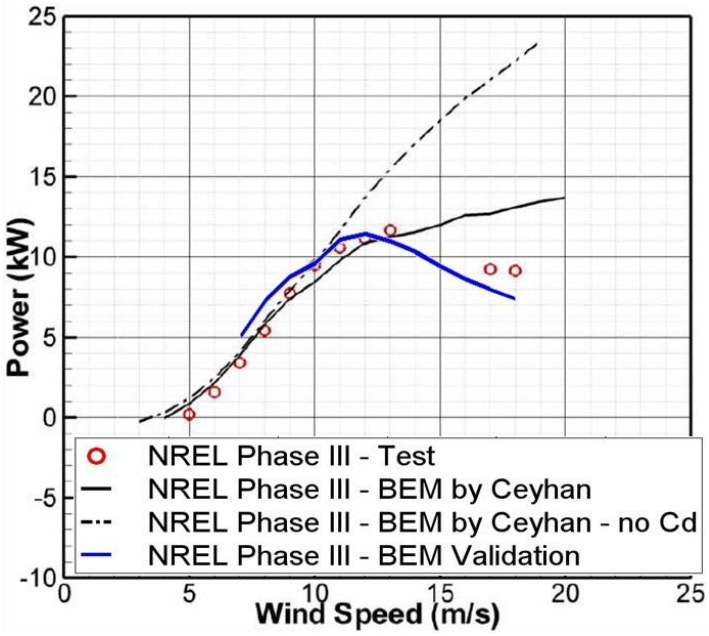

Figure 7-10 Comparison of BEM calculations with test data for NREL Phase III wind turbine

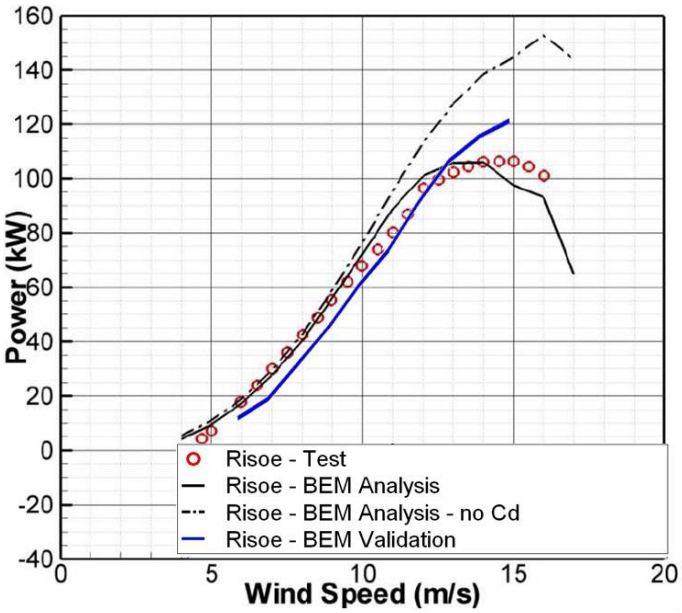

Figure 7-11 Comparison of BEM calculations with test data for Risoe wind turbine

7.5.2 Results of the Performance of Thick Airfoils

In this section, we analyze the performance of various wind turbines (NREL Phase II and Phase III, and Risoe) using thick airfoil sections for their blades employing the BEM code. The power output of turbines is computed with new airfoil sections for blades and is compared with original NREL Phase II and Phase III, and Risoe turbines. Table 7-4 and Figure 7-12 show the operating conditions and geometrical properties of the wind turbines with untwisted and un-tapered blades using a variety of thick airfoil sections. Figure 7-13 shows the power output of the wind turbines using different airfoil sections in Table 7-4 and their comparison with the original NREL Phase II wind turbine with S809 airfoil section for its blades.

Table 7-4 General characteristics of wind turbine using thick airfoil sections

Number of Blades	3
Turbine Diameter	10.06m
Rotational Speed	71.3rpm
Cut-in Wind Speed	6 m/s
Control	Stall Control
Rated Power	19.8kw
Root Extension	0.723m

Blade Set Angle	12 degrees
Twist	None
Chord	0.4572@all span location
Airfoil Sections	FB series (FB-3500-0050, FB-3500-0875, FB-3500-1750), FX 66-S196-V1, DU 91-W2-250, NACA 64421

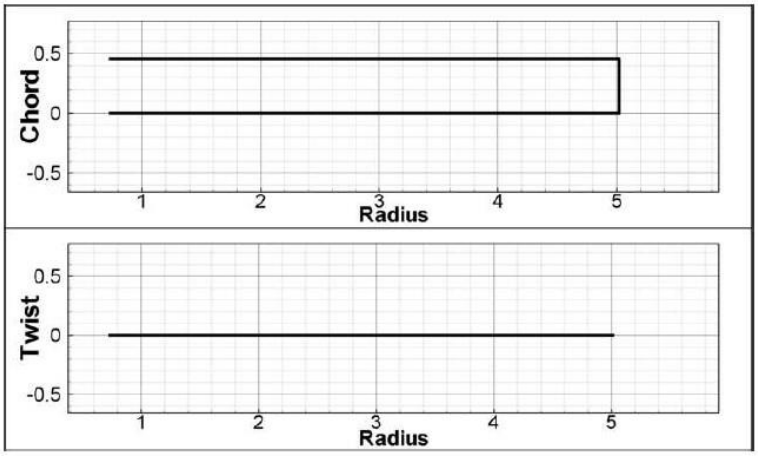

Figure 7-12 Geometric properties of wind turbine using thick airfoil sections

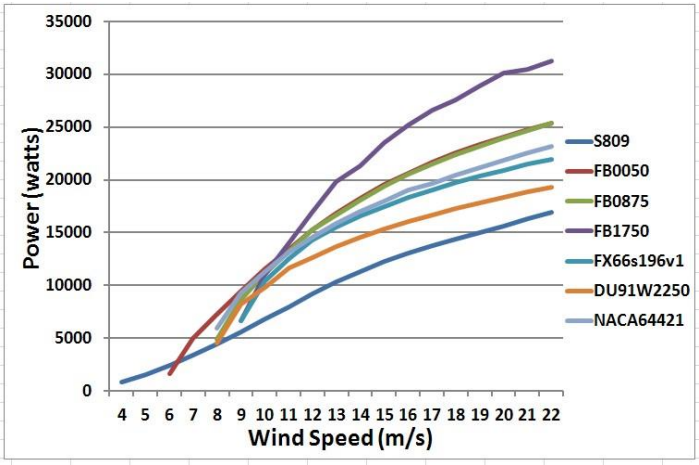

Figure 7-13 Comparison of power output of a wind turbine of Table 7-4 with different airfoil sections with the original NREL Phase II wind turbine with S809 airfoil section

The comparison of results in Figure 7-13 shows that all the wind turbines in Table 7-4 which employ thick airfoils sections have superior performance than the NREL Phase II wind

turbine. Among them, wind turbines with Flat-back airfoils generate greater power than those with other airfoil sections. In particular, the turbine with FB 1750 airfoil section blades generates the largest power output at higher wind speed (greater than 10 m/s). Its power output is almost double compared to that of the original NREL Phase II wind turbine. It can also be noted from Figure 7-13 that for wind speeds between 8 - 10 m/s, wind turbines in Table 7-4 with thick airfoil sections generate consistently more power compared to the NREL Phase II turbine with S809 airfoil section for its blades. However at lower wind speeds below 8m/s, there is no appreciable difference in the power generation with change in the blade airfoil section.

Table 7-5 and Figure 7-14 show the operating conditions and geometrical properties of the wind turbines with twisted and un-tapered blades using a variety of thick airfoil sections. Figure 7-15 shows the power output of the wind turbines using different airfoil sections in Table 7-5 and their comparison with the original NREL Phase III wind turbine with S809 airfoil section for its blades.

Table 7-5 General characteristics of a wind turbine using thick airfoil sections

Number of Blades	3
Turbine Diameter	10.06m
Rotational Speed	71.3rpm`
Cut-in Wind Speed	6 m/s
Control	Stall Control
Rated Power	19.8kw
Root Extension	0.723m
Blade Set Angle	3 degrees
Twist	44 degrees (max.)
Chord	0.4572@all span location
Airfoil Sections	FB series (FB-3500-0050, FB-3500-0875, FB-3500-1750), FX 66-S196-V1, DU 91-W2-250, NACA 64421

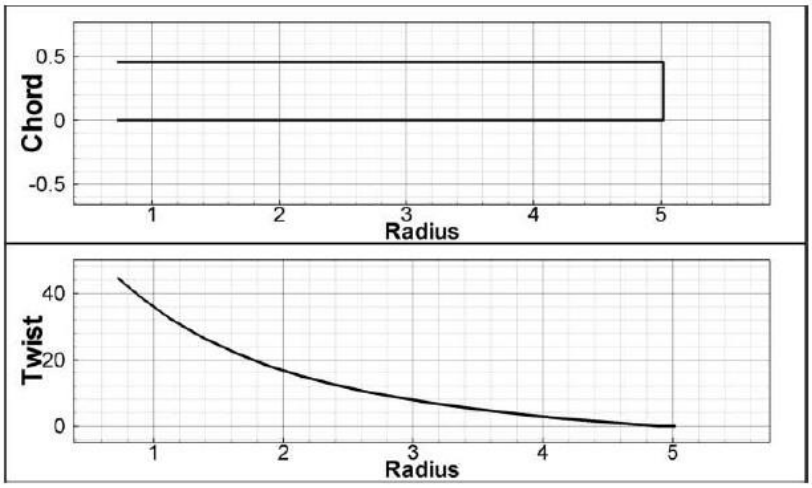

Figure 7-14 Geometric properties of wind turbine using thick airfoil sections

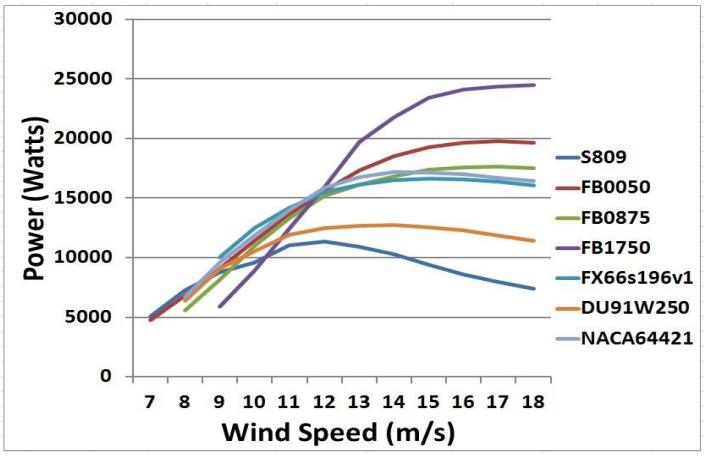

Figure 7-15 Comparison of power output of a wind turbine of Table 7-5 with different airfoil sections with the original NREL Phase III wind turbine with S809 airfoil section

The comparison of results in Figure 7-15 shows that all the wind turbines in Table 7-5 which employ thick airfoils sections have superior performance than the NREL Phase III wind turbine except for the turbines with FB series airfoil blade sections, which only perform better at higher wind speeds (larger than 10m/s). However at wind speed larger than 10m/s, the performance of wind turbines with FB series blade sections is superior. In particular, the turbine with FB 1750 airfoil section blades generates the largest power output at higher wind speed (greater than 10 m/s). Its power output is almost two to three times compared to that of the original NREL Phase III wind turbine. It can also be noted from Figure 7-15 that for wind speeds between 8 - 10 m/s, wind turbines in Table 7-5 with thick airfoil sections generate consistently more power compared to the NREL Phase III turbine with S809 airfoil section for its blades.

However at lower wind speeds below 8m/s, there is no appreciable difference in the power generation with change in the blade airfoil section.

Table 7-6 and Figure 7-16 show the operating conditions and geometrical properties of the wind turbines with both twisted and tapered blades using a variety of thick airfoil sections. Figure 7-17 shows the power output of the wind turbines using different airfoil sections in Table 7-6 and their comparison with the original Risoe wind turbine with NACA 63-2xx series airfoil section for its blades.

The comparison of results in Figure 7-17 shows that all the wind turbines in Table 7-6 which employ thick airfoils sections have slightly superior performance than the Risoe wind turbine only at higher wind speeds (larger than 10m/s). However at wind speeds lower than 10m/s, there is no appreciable difference in the performance.

Table 7-6 Risoe wind turbine general characteristics

Number of Blades	3
Turbine Diameter	19.0 m
Rotational Speed	35.6 and 47.5 rpm`
Cut-in Wind Speed	4 m/s
Control	Stall Control
Rated Power	100 kw
Root Extension	2.3 m
Blade Set Angle	1.8 degrees
Twist	15 degrees (max.)
Root Chord	1.09 m
Tip Chord	0.45 m
Airfoil Sections	FB series (FB-3500-0050, FB-3500-0875, FB-3500-1750), FX 66-S196-V1, DU 91-W2-250, NACA 64421

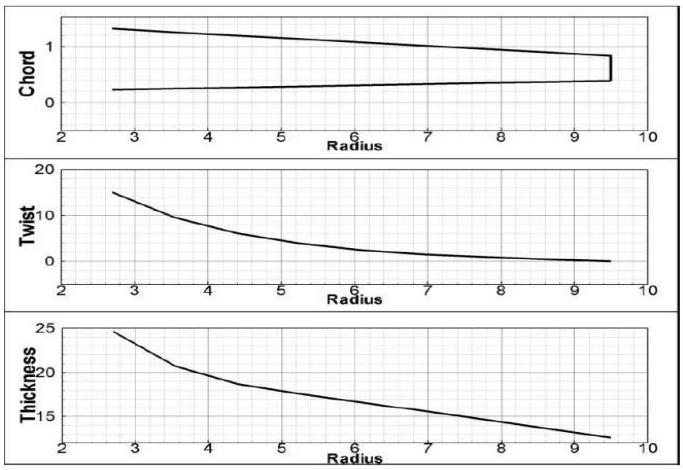

Figure 7-16 Geometric properties of wind turbine using thick airfoil sections

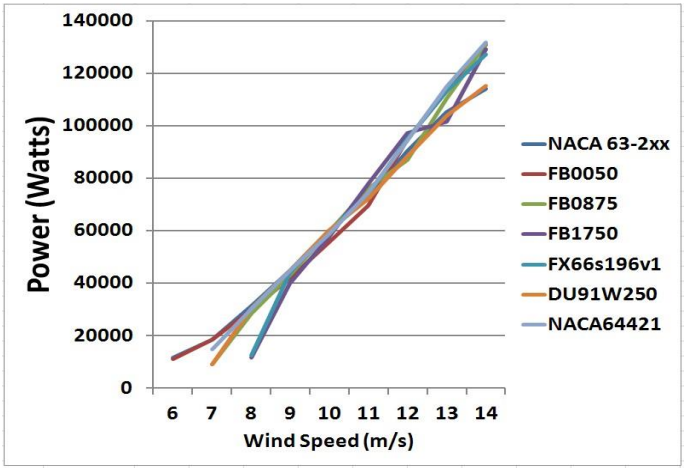

Figure 7-17 Comparison of power output of a wind turbine of Table 7-6 with different airfoil sections with the original Risoe wind turbine with NACA 63-2xx airfoil section

Some parametric studies were also performed to determine the effect of change in turbine diameter and the number of blades on turbine power output. For the study of the effect of change in turbine diameter on power output, the NREL Phase II turbine was selected. Figure 7-18 shows the variation of power output with wind speed for different turbine diameters. As expected, the wind turbines with larger turbine diameter produce higher power. However it is important to note from Figure 7-18 that the combined effect of higher wind speed and larger diameter can be very substantial (well-known from simple analysis); it is validated here by using the more complex BEM code.

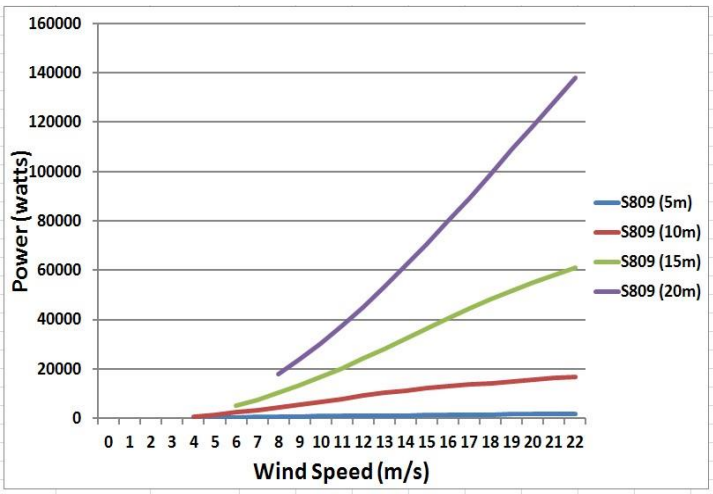

Figure 7-18 Variation of power output with wind speed for different diameters of NREL Phase II wind turbine

For studying the effect of number of blades on the turbine power out, both NREL II and III wind turbines were selected. FB1750 airfoil blade section was chosen because of its outstanding performance in power production. The number of blades was changed from 1 to 5. Figure 7-19 shows the comparison of the power output of NREL II configuration based wind turbine with different number of blades compared to the original 3-bladed NREL II wind turbine (which uses the S809 airfoil section).

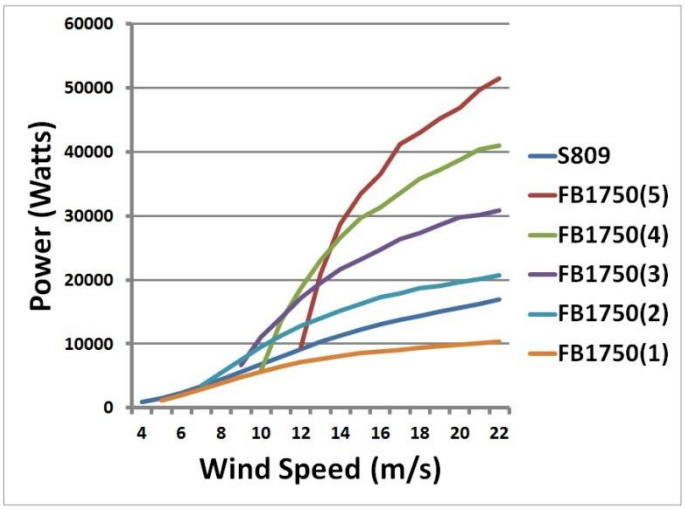

Figure 7-19 Comparison of power output from original 3-bladed NREL II configuration based wind turbine (with S 809 blade sections) with NREL II wind turbine with 1 to 5 blades (with FB 1750 airfoil section)

Figure 7-20 shows the comparison of the power output of NREL III - based wind turbine with various numbers of blades with the original 3-bladed NREL III wind turbine (which uses S809 airfoil section). It can be concluded from Figures 7-19 and 7-20 that more number of blades tends to increase the power output at high wind speed (greater than 12 m/s) while maintaining or even decreasing the power output at lower wind speeds. Furthermore, as expected, the power output from one-bladed wind turbine is smaller than the original 3-bladed NREL II and III wind turbines even though it employs the FB1750 airfoil as blade cross section. However, one can observe that the two-bladed wind turbines have started to show superior performance at high wind speed. For NREL II configuration based wind turbine, all cases except that of one-blade wind turbine have better power output than the original NREL II turbine for the entire wind speed range. For NREL III configuration based base wind turbines, the increase in power output happens only at high wind speeds.

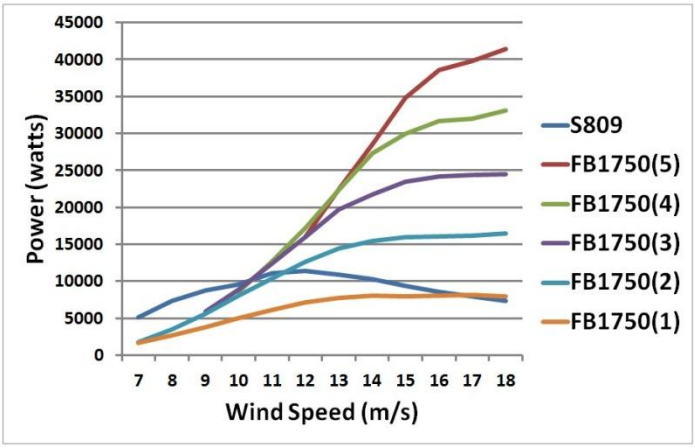

Figure 7-20 Comparison of power output from original 3-bladed NREL III wind turbine (with S809 airfoil section) with NREL III configuration based wind turbines for different number of blades (with FB1750 airfoil section)

7.5.3 Results of Simplified Dynamic Inflow Model

This section studies the wind turbine performance in a slow time scale. The effect of change in operating conditions are simulated based on two different models, namely BEM^{qs} (or basic BEM) and BEM^{inflow} (or simplified dynamic inflow model). The purpose is to investigate the effect of dynamic inflow in wind speed estimation over a deterministic wind speed close to the rated

operation [95]. Three types of wind turbines from Reference [20] are studied, namely NREL Phase II, NREL PhaseIII and Risoe wind turbines. For the purpose of comparison, the wind speed of 12 m/s is chosen for all the three wind turbines while this wind speed is near the rated power of Risoe wind turbine. The considered input operating condition is the wind turbine rotational speed Ω (rad/s). Since this study focuses on the startup stage of wind turbines from stillness to operating rotation, the changes in Ω as input to the aero dynamic models are shown in Figure 7-21 for NREL-Phase II and Phase III wind turbines, and in Figure 7-22 for Risoe wind turbine. Figure 7-23, 7-24 and 7-25 show the outputs from aerodynamic models in the form of wind turbine power generation.

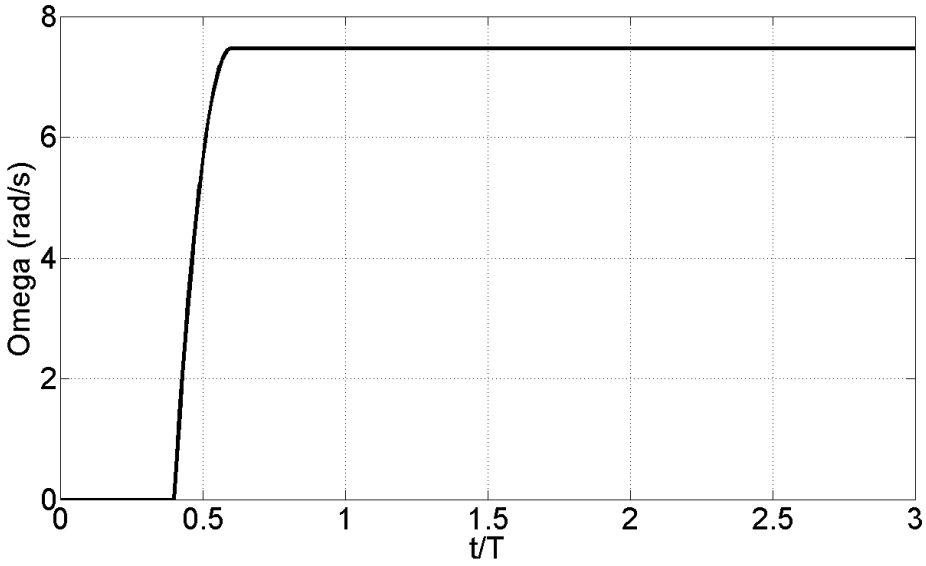

Figure 7-21 Input to the aerodynamic model for NREL Phase II and Phase III wind turbines

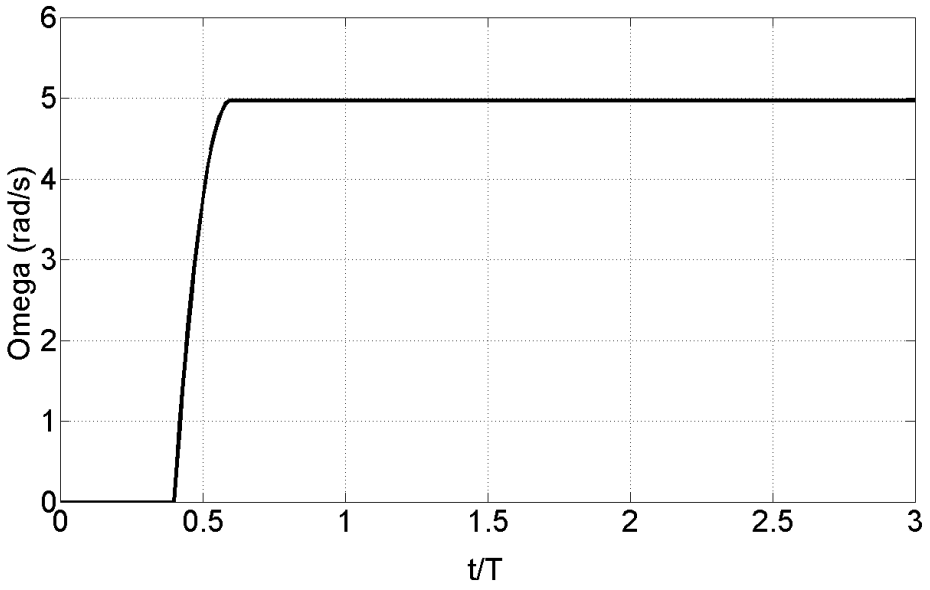

Figure 7-22 Input to the aerodynamic model for Risoe wind turbine

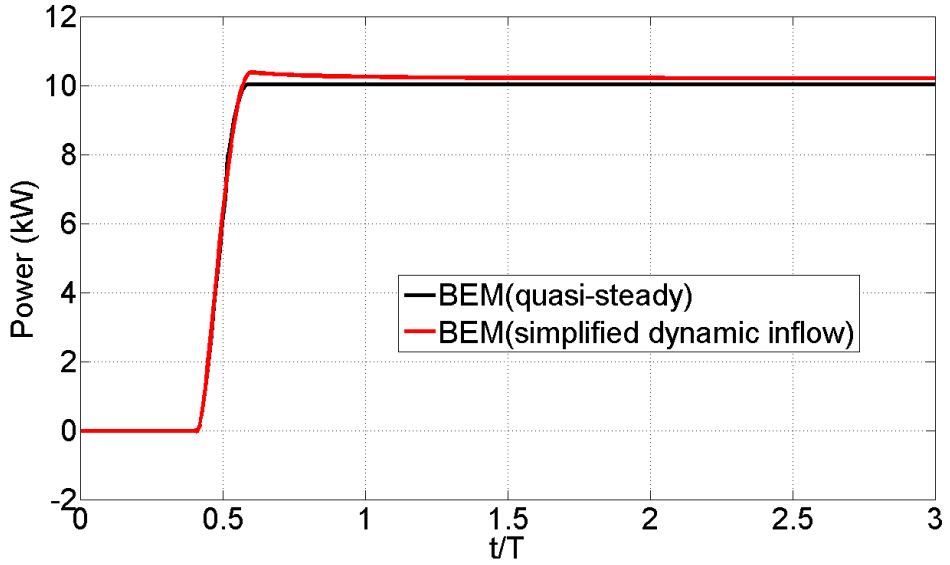

Figure 7-23 Output from the aerodynamic model for NREL Phase II wind turbine

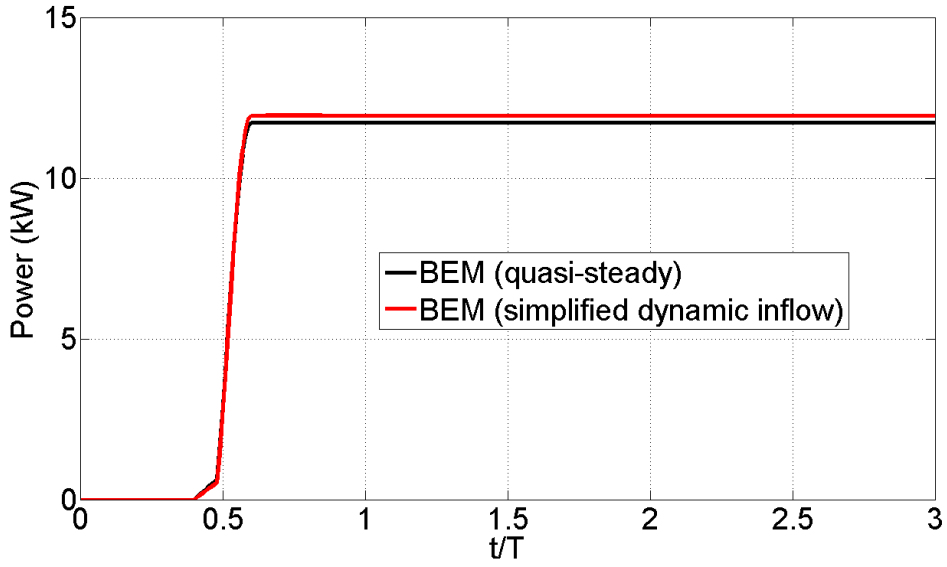

Figure 7-24 Output from the aerodynamic model for NREL Phase III wind turbine

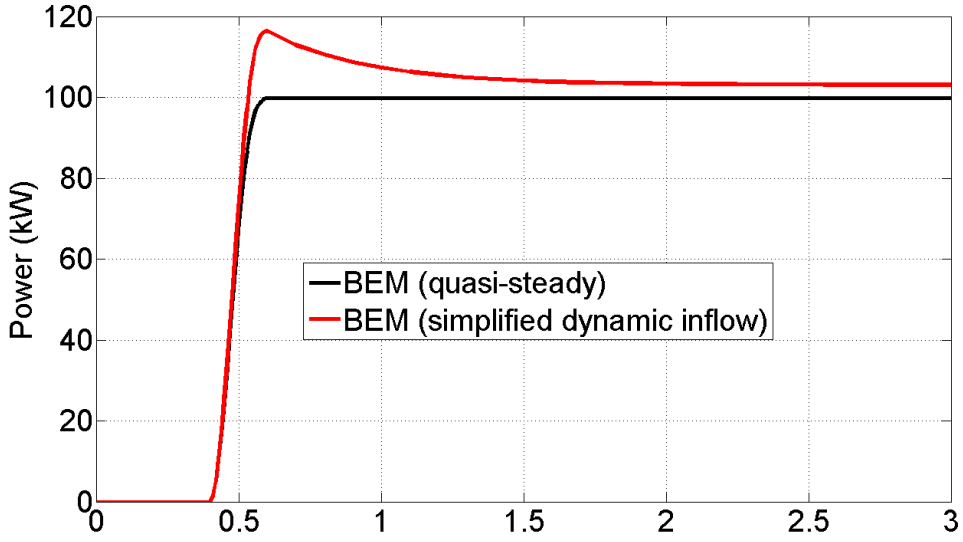

Figure 7-25 Output from aerodynamic model for Risoe wind turbine

Figure 7-21 and 7-22 describe the starting stage of wind turbines at a fixed wind speed of 12m/s. The input rotational speed Ω changes from zero to the corresponding operating value for each wind turbines considered. Figure 7-21 corresponds to NREL-Phase II and III wind turbines and Figure 7-22 corresponds to Risoe wind turbine. From the output power generation curves of

Figure 7-23, 7-24 and 7-25, one can see the wind turbine behavior on a large time scale; the inclusion of dynamic inflow model introduces a change in the basic BEM mainly by increasing Ω from zero to the operating value in a very small time. In steady operation period of the wind turbine, there is very small difference between the two models and the experimental data as expected, implying that both the codes BEM^{qs} and BEM^{inflow} accurately evaluate the power generation as expected.

During the change in Ω, the basic BEM^{qs} predicts the power increasing gradually with Ω until reaching the steady state value, while BEM^{inflow} first predicts a power output higher than BEM^{qs} then decreases slowly to the steady state value. This difference is due to the difference in the intrinsic capability of the two codes described in the previous section. Due to the delayed response of the aerodynamic forces to the change in operating wind conditions, the real performance of wind turbine to the changing wind condition is always different than the steady-state value until the operating condition has settled to a new equilibrium. The results show that the simplified dynamic inflow model can capture the performance of a wind turbine under changing wind condition. The results also show that among the three wind turbines considered, the basic BEM method BEM^{qs} has poor predictions in determining the power of Risoe wind turbine while for the NREL wind turbines, the results are reasonable using both the BEM^{qs} and BEM^{inflow} code. The results reported here are preliminary and require future refinement and application of BEM^{inflow}.

Chapter 8 Optimization of Wind Farm Layouts

8.1 Overview

This study focuses on the optimization of wind turbine distributions in the wind farm model in Ref. [52]. For a HAWT, this study employs a more accurate wake model due to Werle [97] and a more realistic cost model for large turbines (80-120m diameter) with more realistic constraints on turbine placement than random distribution of Mosetti et al. [52] or uniformly distributed square grid arrangement of Grady et al. [53]. This study finds that the uniformly distributed square grid arrangement of Grady et al. [53] is indeed optimal for large HAWT even with improved wake and cost models.

This study also focuses on the wind farms with vertical-axis wind turbines (VAWT) such as Darrieus rotor. A simple wake model following the work of Jensen [55] is developed for the VAWT. It is found that a uniform grid arrangement is also best in the case of a VAWT for optimal power generation.

8.2 Wake, Power and Cost Modeling of a HAWT

8.2.1 Jensen's Wake Modeling of a HAWT

All the results reported to date in the literature on optimal layout of wind turbines in a wind farm employ the simple wake model of Jensen [55] and use a genetic algorithm for optimization of an objective function based on power output or a combination of power output and cost [52-54]. In Jensen's model, the near field effects of the turbine wake are neglected and the near wake is simplified as an axisymmetric wake with a velocity defect which linearly spreads with distance downstream into the far – field where it encounters another turbine as shown in Figure 8-1. Let *U*

be the mean wind speed, then employing the inviscid actuator disc theory of Betz, it can be shown that

$$V_0 = (1-2a)U \quad \text{and} \quad r_0 = r_r\sqrt{\frac{1-a}{1-2a}} \tag{8-1}$$

where r_0 is the radius of the axisymmetric wake immediately behind the turbine rotor, a is the axial induction factor, and r_r is the rotor radius of the turbine.

The wind velocity in the wake at a distance x downstream can then be determined using the principle of conservation of momentum as:

$$u = U[1-\frac{2a}{(1+\alpha(x/r_0))^2}] \tag{8-2}$$

It can be shown by the Betz's theory that the turbine thrust coefficient C_T is related to the axial induction factor a by the following relation:

$$a = \frac{1-\sqrt{1-C_T}}{2} \tag{8-3}$$

The entrainment constant α is empirically given as [53]:

$$\alpha = \frac{0.5}{\ln(z/z_0)} \tag{8-4}$$

where z is the turbine hub height and z_0 is the surface roughness.

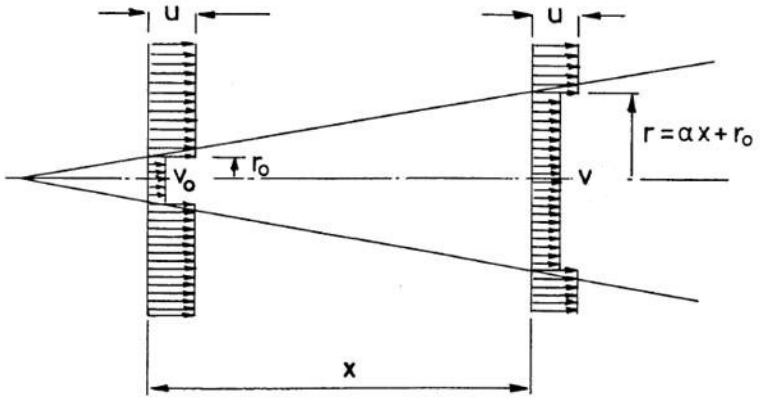

Figure 8-1 Schematic of the Jensen's wake model [53]

8.2.2 Werle's Wake Modeling of a HAWT

Werle [97] attempted to improve on the simple wake model of Jensen [55]. He divided the wake into three parts: the near wake, the intermediate wake and the far wake. His model is supposedly better since it considers the near wake region, where the velocity is slightly higher compared to intermediate wake region as shown in Figure 8-2. Jenson's model does not consider the near wake region. Let X be the non-dimensional distance downstream of the turbine:

$$X \equiv x / D_p \tag{8-5}$$

where D_p is the turbine diameter $D_p = 2r_r$. Let D_w denote the diameter of the velocity defect in the wake at X. Then Werle's wake model can be described by the following expressions which give the wind speed and wake growth downstream of the turbine:

For $X < X_m$,

$$u = 1 - \frac{1-U}{2}\left[1 + \frac{2X}{\sqrt{1+4X^2}}\right] \tag{8-6}$$

$$D_w / D_p = \sqrt{\frac{1+U}{2u}} \tag{8-7}$$

For $X > X_m$,

$$u = 1 - \frac{1-u_m}{[(X-X_m)(2(1-u_m))^{3/2} / C_T^{1/2} + 1]^{2/3}} \tag{8-8}$$

$$D_w / D_p = D_m / D_p [C_T (X - X_m) / (D_m / D_p)^3 + 1]^{1/3} \tag{8-9}$$

In equation (8-6) to (8-9), X_m is the location where the far wake model is coupled to the near wake, D_m is the diameter of the wake at X_m and u_m is the velocity in the wake at X_m. X_m is given by:

$$X_m = 2 + K_m \frac{2r_0}{D_p} \frac{1+U_0}{1-U_0} \tag{8-10}$$

D_m / D_p is given by:

$$D_m / D_p = \sqrt{\frac{1+U_0}{2u_m}} \tag{8-11}$$

and u_m is given by:

$$u_m = 1 - \frac{1-U}{2}\left[1 + \frac{2X_m}{\sqrt{1+4X_m^2}}\right] \tag{8-12}$$

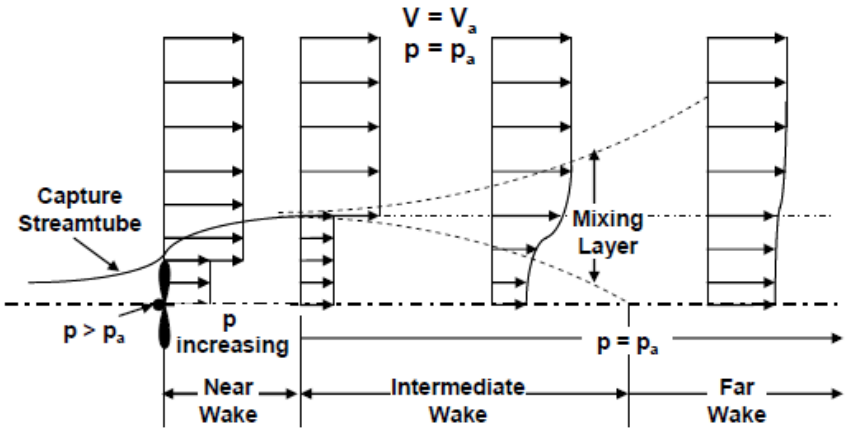

Figure 8-2 Schematic of Werle's wake model [127]

8.2.3 Multiple Wake and Cost Modeling for HAWT

In general a HAWT downstream of an array of turbines may encounter multiple wakes due to several turbines upstream of it. Since various wakes of the array of turbines form a mixed wake, the kinetic energy of this mixed wake is assumed to be equal to the sum of the kinetic energy of various wake deficits. This results in the following expression for the velocity downstream of N turbines [52]:

$$(1 - \frac{\bar{u}}{U})^2 = \sum_{i=1}^{N} (1 - \frac{u_i}{U})^2 \tag{8-13}$$

In equation (8-13), $\bar{u}$ is the average velocity experienced by the turbine due to the wake deficit velocity of multiple turbines given by u_i, $i = 1 \ldots\ldots N$. Assuming the non-dimensionalized cost/year of a single turbine to be 1, a maximum cost reduction of 1/3 can be obtained for each turbine if a large number of machines are installed. We then assume that the total cost/year of the whole wind farm can be expressed by the following relation [53]:

$$cost = N(\frac{2}{3} + \frac{1}{3}e^{-0.00174N^2}) \tag{8-14}$$

The power curve presented in Mosetti et al. [52] for the HAWT gives the following expression for power output of the whole wind farm:

$$P = \sum_{i=1}^{N} 0.3\bar{u}_i^{\,3} \tag{8-15}$$

The optimization is based on the following objective function:

$$\textit{Objective function} = \frac{cost}{P} \tag{8-16}$$

Equation (8-16) is the cost function for the optimization with genetic algorithm.

8.3 Wake, Power and Cost Modeling of a VAWT

8.3.1 Single Stream Model of a VAWT

The book by Manwell, McGowan and Rogers [98] describes the analysis of the single stream tube model for a two-dimensional single straight-blade vertical axis wind turbine. The geometry of this simple model is shown in Figure 8-3; the blade is rotating in the counter-clockwise direction while the wind blows from left to the right. Some modifications are made to the model described in the book by Manwell et al. [98] so that it can be applied to the flow field with multiple wakes. Let $e = u_{local}/U$, where u_{local} represents the velocity u in the wake of a single turbine or $\bar{u}$, the velocity due to multiple wakes. Now, applying the blade element theory together with the principle of momentum conservation and assuming high tip speed ratios λ, the following expressions for induction factor *a* and power coefficient *Cp* for a single vertical axis wind turbine are obtained as [98]:

$$a \approx \frac{1}{16}\frac{Bc}{R} e C_{l,\alpha} \lambda \tag{8-17}$$

$$C_p \approx 4ea(1-a)^2 - \frac{1}{2}\frac{Bc}{R} C_{d,0} \lambda^3 \tag{8-18}$$

Then, the power output of single VAWT is given by:

$$P_s = \frac{1}{2}\rho 2RHU^3 C_p \tag{8-19}$$

where B is the number of blades, c is the chord length of the blade airfoil, R is the rotor radius, λ is the tip speed ratio, H is the total blade length, ρ is air density, U is the free stream velocity and $C_{l,\alpha}$ is the lift curve slope for small angles of attack (below stall).

We assume a symmetrical airfoil; the lift coefficient is linearly related to the angle of attack, that is $C_l = C_{l,\alpha}\alpha$. $C_{l,\alpha}$ is calculated from the lift vs. angle of attack curve for NACA0015 from NACA report [99]. In this study, $C_{l,\alpha} \approx \frac{18}{\pi}$ and $C_{d,0}$ is assumed to be zero.

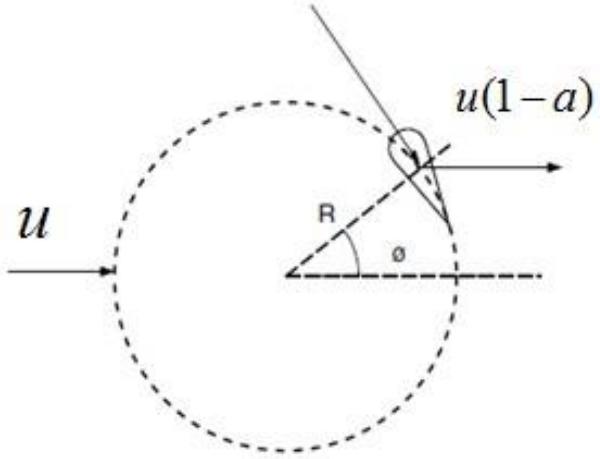

Figure 8-3 Single stream rube geometry of a VAWT

8.3.2 Wake Model for a VAWT

Again, we assume the VAWT to be an actuator disc so the near field behind the wind turbine is neglected. We modify the Jensen's model [55] of the wake and apply it to determine the wake of a VAWT. Now, the cross-section area of the streamtube is a square of width 2*R* and height *H* instead of a circle. From the conservation of momentum,

$$2r_0 HV_0 + 2(r - r_0)HU = 2rHu \tag{8-20}$$

where r_0 and r are as shown in Figure 8-1.

Therefore, we obtain the following expression for the velocity downstream of a single VAWT:

$$u = U[1 - \frac{2a}{1 + \alpha(x / r_0)}] \tag{8-21}$$

In equation (8-21), α is the same as given in equation (8-4). For wind turbine downstream encountering multiple wakes, again equation (8-13) is employed. The velocity $\bar{u}$ is then used to determine the power output of the wind turbine.

8.4 Results and Discussion

8.4.1 Layout Optimization of HAWT Wind Farm

We consider two cases of HAWTs with the geometric parameters shown in Table 8-1. These parameters in the second column were also used by Grady et al. [53] in their study while the ones in the third column were cited in Reference [100] as the size of the tallest wind turbine in the U.S. in 2005. The size of the farm considered is $50D_r$ x $50D_r$ and a wind with uniform speed of 12 m/s is considered. Here D_r is the rotor diameter of a HAWT. This assumption results in the following simplification: the optimization for one $50D_r$ x $50D_r$ wind farm equals to the optimization for one column of the size $5D_r$ x $50D_r$ since the largest wake in one column still stays in it. After knowing the layout in one column, the layout for the whole wind farm is composed with 10 columns with the same pattern. Also, the best power output is 10 times the one for one column.

Table 8-1 Geometric parameters of a HAWT

Size parameters	Case I	Case II
Hub height, z [m]	60	80
Rotor radius, r_r [m]	20	41
Thrust coefficient, C_T	0.88	0.88

In this study, we first employ the wake model of Jensen [55] with case I in Table 8-1. Figure 8-4 shows the convergence history of the objective function given by equation (8-16). The calculation starts with a best objective function of approximately 473 and power output of about 1409 kW. It jumps quickly to a higher value and stays unchanged for the rest of the generations up to 250. The best objective function value obtained is 479.5 with cost equal to 2.98 and total power equal to 1431.2 kW. The history of medians follows the same trend and converges to the same value as the best objective value. The mean objective values also gets close to this value but stays unsteady due to the mutation in GA. Figure 8-5 shows the configuration for placement of wind turbines to get the optimal value of the objective function for the entire wind farm; identical results were obtained by Grady et al. [53]. Figure 8-5(a) is the optimal configuration for the farm with just one column with the same cell size. Figure 8-5(b) is the extended optimized result for a farm land with a size of $50D_r$ x $50D_r$. The extended result for the whole farm has a total power output of 14312 kW.

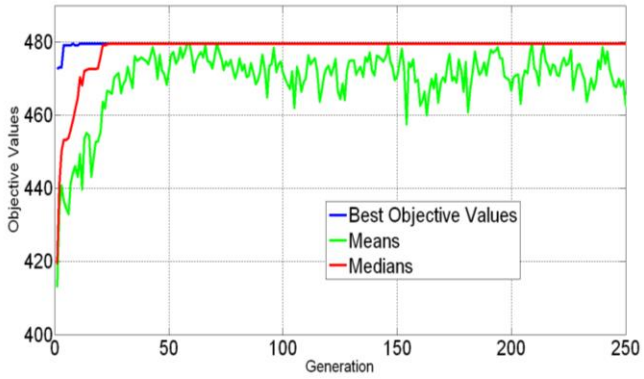

(a) Best, mean and median objective values

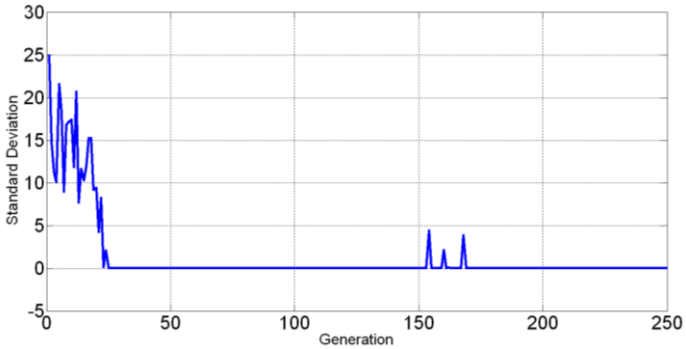

(b) Standard deviations

Figure 8-4 Convergence history of the objective function (total power/cost) for HAWT wind farm using GA for case I

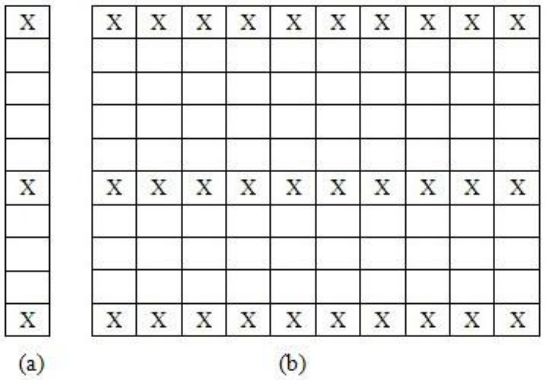

Figure 8-5 Optimal layout of HAWT in a $50D_r$ x $50D_r$ wind farm

Next, we study the effect on the optimization results by using a more complex but realistic wake model due to Werle [97] for both of the cases in Table 8-1 by assuming that the cost/year of two turbines stays unchanged. Figure 8-6 shows the changes in the wake velocity and wake growth behind a turbine. The curves in red are those obtained for the turbine parameters used in this study given in Table 8-1. The red curves calculated in this study for C_T = 0.88 fall accurately among those calculated by Werle [97] for different values of C_T. Using the wake model of Werle, we can perform the optimization study in Table 8-2. The convergence history is shown in Figure 8-7. The values in Table 8-2 are very close to those obtained by using Jensen's [55] model. The optimal layout configuration for the wind farm is the same as shown in Figure 8-5.

Table 8-2 Optimization results using Werle's wake model

Optimal values	Case I	Case II
Objective function	454.3	412.9
Cost/year	2.98	2.98
Total power [kW]	1355.7	1230.4

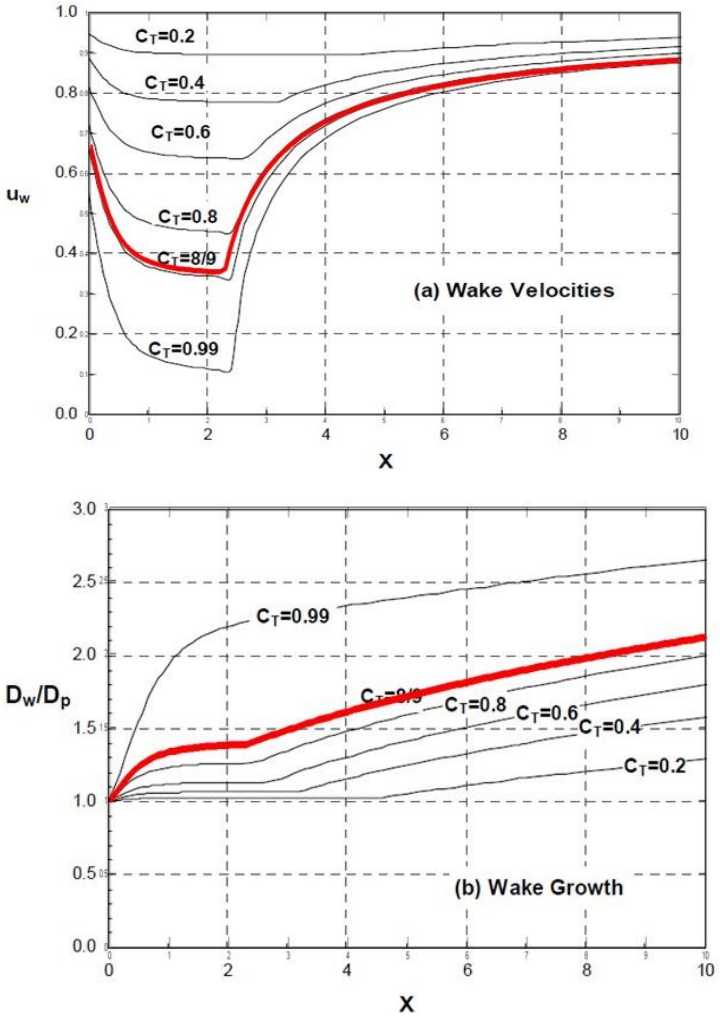

Figure 8-6 The variation in wake velocity and growth behind the HAWT using Werle's model [97]; the curves in red are present calculations for C_T=0.88.

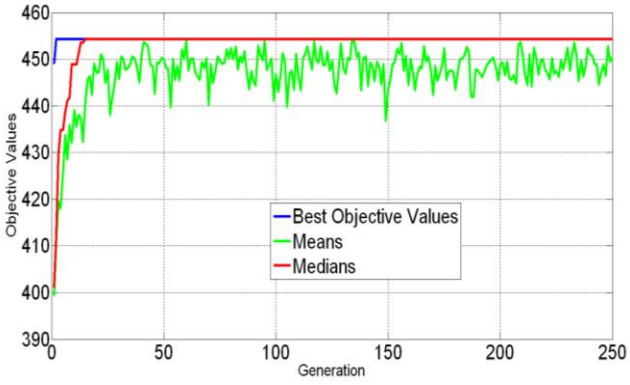

(a) Best, mean and median objective values for Case I

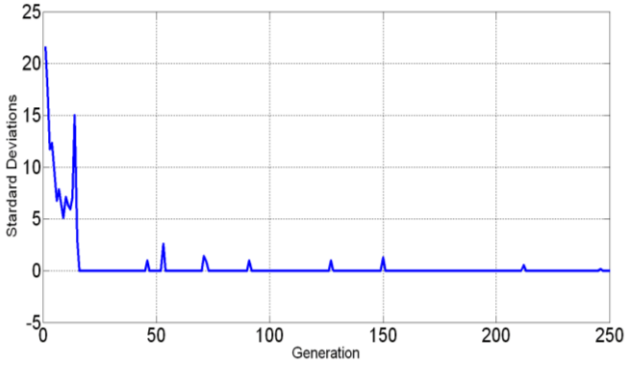

(b) Standard deviations for Case I

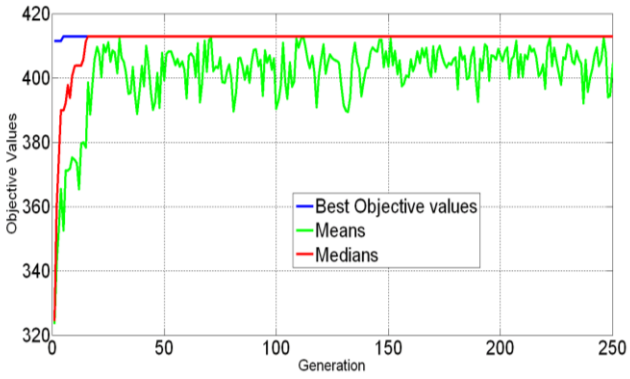

(c) Best, mean and median objective values for Case II

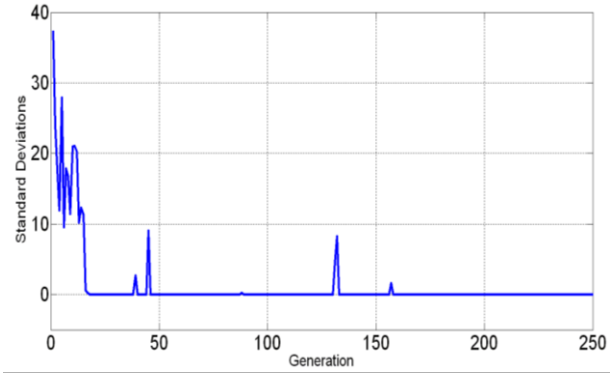

(d) Standard deviations for Case II

Figure 8-7 Convergence history of the objective function (total power/cost) for HAWT wind farm using GA with Werle's wake model [97] for cases I, II

8.4.2 Layout Optimization of VAWT Wind Farm

We consider VAWT with the geometric parameters shown in Table 8-3. Case III have been taken from the paper of Staelens et al. [101] and Case III has a double rotor radius compared to Case IV so that the tip-speed ratio also doubles. Again, the size of the farm is $50D_r$ x $50D_r$ and a wind with uniform speed of 12 m/s is considered.

Table 8-3 Geometric parameters of a VAWT

Variable	Values	
	Case III	Case IV
Rotor radius, R [m]	6	3
Blade profile	NACA0015	
Blade chord, c [m]	0.2	
Blade length, H [m]	6	
Hub height, z [m]	6	
Rotational speed, ω [rad/s]	13.09	
Tip-speed ratio, X_{EQ}	2.9	
Wind Speed, U [m/s]	12	
Air density, ρ_∞ [kg/m^3]	1.21	

Figure 8-8 shows the convergence history of the GA optimization for VAWT wind farm. The results are given in Table 8-4. The optimal layout is the same as that of a HAWT as shown in Figure 8-9.

Table 8-4 Optimization results for VAWT wind farm

Optimization Objective	Case III	Case IV
Total Power Output [kW]	537.7	460.6

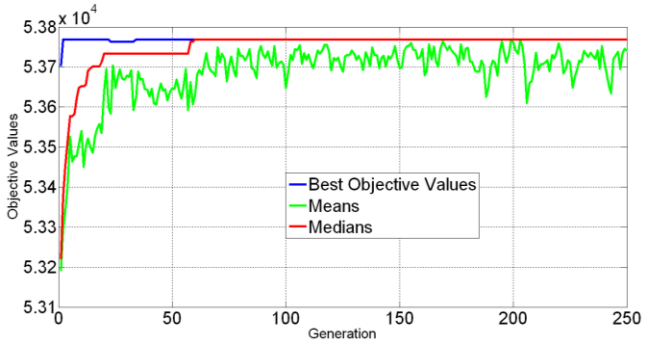

(a) Best, mean and median objective values for Case III

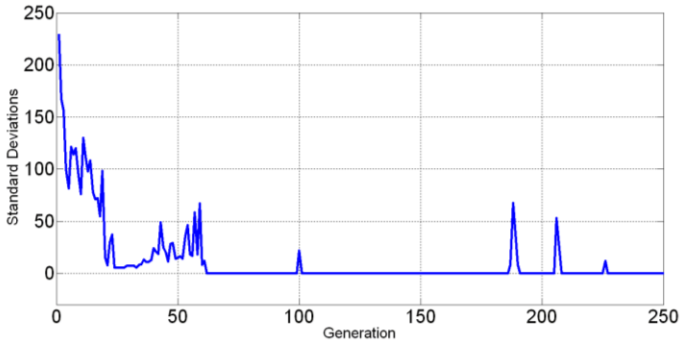

(b) Standard deviations for Case III

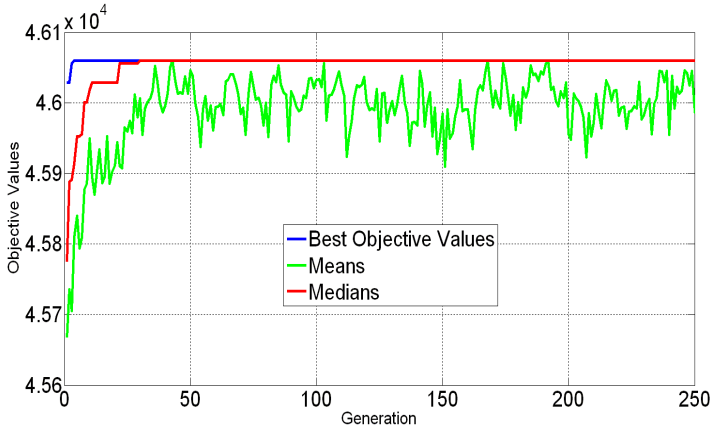

(c) Best, mean and median objective values for Case IV

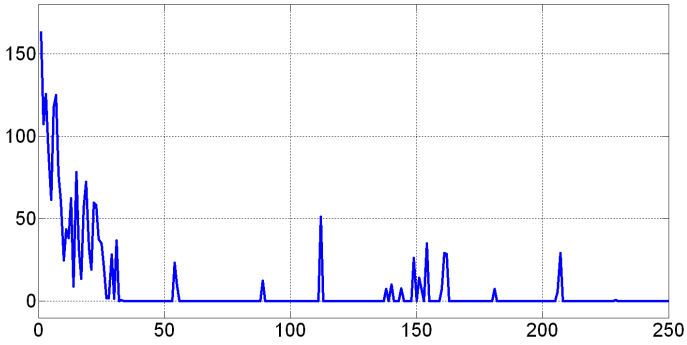

(d) Standard deviations for Case IV

Figure 8-8 Convergence history of the objective function (total power/cost) for VAWT wind farm using GA

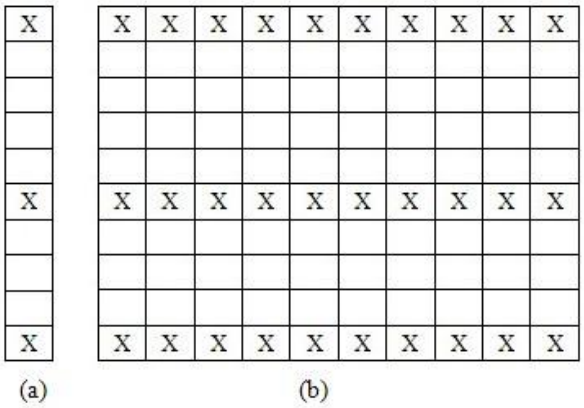

Figure 8-9 Optimal layout of VAWT in a $50D_r$ x $50D_r$ wind farm

Chapter 9 Optimization of a 3-D Wind-Turbine Blade

9.1 Overview

This chapter addresses the optimization of a finite span blade in a 3D flow field. The blade shape considered is a simple straight-bladed untapered wing with a NACA 0012 airfoil as cross section. Although the case studied in this chapter is far from the real wind turbine blade, it is still of great interest in the context of the 3D optimization.

Computationally, 3D shape optimization is far from demanding than 2D. The governing equations increase in complexity due to an extra transport equation for the third velocity component. Physically, there exists non-uniform spanwise pressure loading and tip vortex formation in 3D fixed wing flow. The tip vortices entrain much of the turbulent wake behind the wing and evolve downstream. Their existence and persistence is a crucial element in lifting line theory such that the total circulation of the tip vortex is equal (for potential flow) to the bound circulation over the wing, which is proportional to lift. Their salient features are high swirl velocities, low vortex core pressures, contribution to induced drag, and axial velocity deficits with respect to the surrounding flow. Tip vortices are an example of a coherent turbulent structure; they pose a challenge for most of the turbulence models.

This chapter focuses on optimizing the cross sectional shapes of a 3D straight-bladed untapered wind--turbine blade. The baseline shape of the cross sections is NACA 0012 airfoils. The geometry of the blade shape is shown in Figure 9-1. The chord length is 0.203m and the half span length is 0.879m. The commercial CFD software FLUENT is used to calculate the 3D flow field together with a genetic algorithm as the optimization method to find the optimal shapes with improved aerodynamic characteristics.

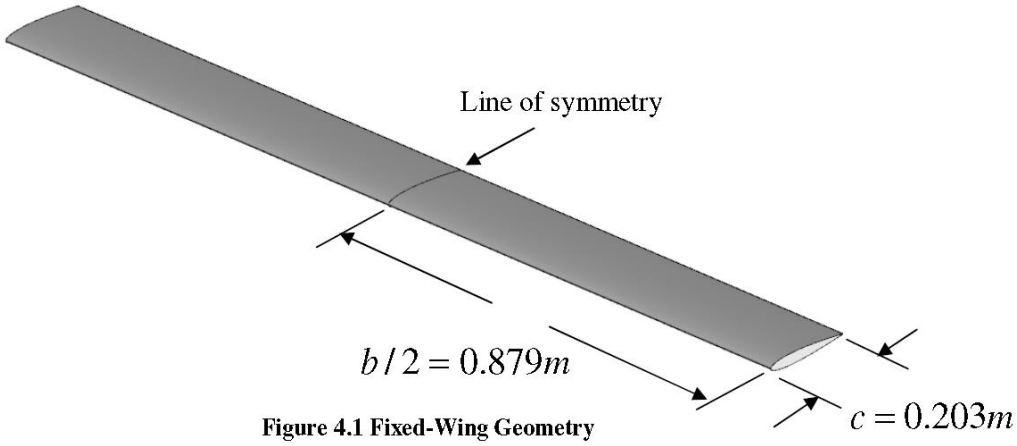

Figure 9-1 Geometry of wind turbine blade with NACA 0012 cross section

9.2 Wind Tunnel Modeling and Mesh Generation

Since the turbine blade is symmetric about the line in the middle as shown in Figure 9-1, only half of the geometry shown is enough for calculation. In order to create the computational domain and generate mesh, the commercially available software "Gambit" is used to build a wind tunnel model and generate an unstructured mesh around the blade in the computational domain. As shown in Figure 9-2, a 3D straight untapered blade is placed inside a computational domain (mimicking a wind tunnel) with inflow and outflow boundaries as shown. The wall boundary condition is applied to the top and bottom surface of the computational box and to the blade surface. The back and front surfaces of the computational box are set as symmetry boundary condition due to the free motion of air on these surfaces.

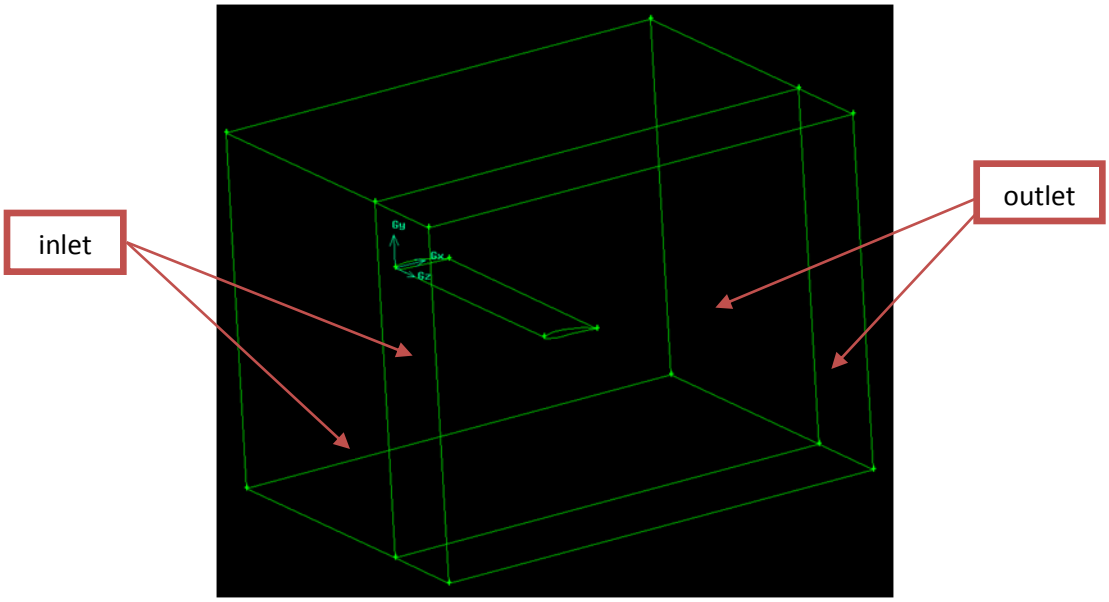

Figure 9-2 Computational model of wind tunnel with a 3D straight untapered blade inside

Gambit reads the commands in a journal file to automatically create the geometry and produce mesh files that are imported into FLUENT for computation. Figure 9-3 is an example of the unstructured mesh generated on the back surface of the wind tunnel.

As shown in Figure 9-3, one important part of the mesh shape is that it must be smooth and dense enough to be suitable for any arbitrary airfoil shape and 3D wing form. Thus, in application of the genetic algorithm, the wind tunnel geometry is always the same, but the airfoil/blade in the center of the tunnel changes from one generation to the next. This poses a challenge for mesh generation in 3D. Faces are meshed using quadrilateral cells, and we require that the number of nodes on opposite faces be identical. To ensure this distribution, we define a set number of nodes (and not relative node spacing) along each edge. Otherwise, thicker or more cambered airfoil edges would have more nodes than thinner ones if a relative distribution was used. A refined boundary layer is carefully constructed around the airfoil to capture the boundary layer behavior.

Figure 9-4 is an example of the mesh generated around the airfoil surface. Although the meshes are unstructured in the flow field, they are structured on the airfoil surfaces due to the boundary layer. The meshes are finer around the leading and trailing edge part of the wing and coarser on the other parts.

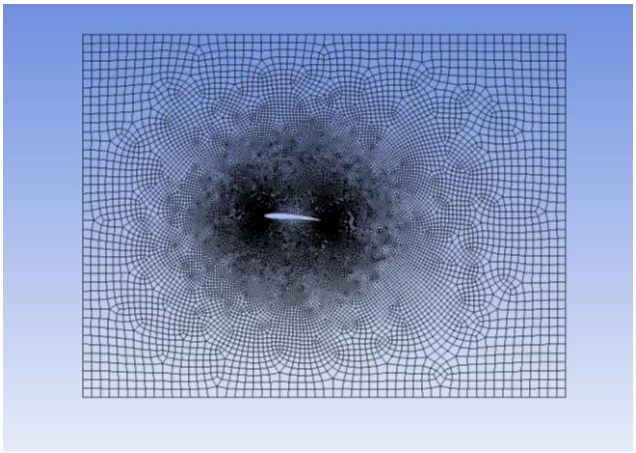

Figure 9-3 Example of mesh on the back surface of the wind tunnel

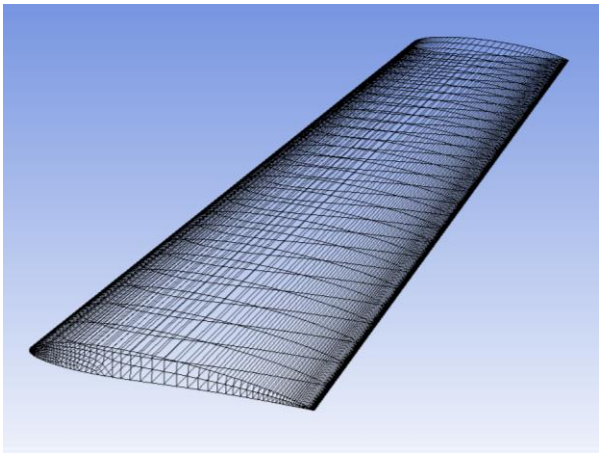

Figure 9-4 Mesh on the blade surface

Figure 9-5 shows a typical complete mesh in the computational domain (not all mesh points are shown in the figure for the purpose of clarity). The interior of the boundary is meshed with a hex/wedge cell scheme. The meshes around the wing are very dense and are carefully refined so that they can provide good prediction of the boundary layer behavior especially when there is boundary layer separation on the suction surface. The generated mesh has a node/cell/face count of 1,022,346/991,093/3,004,425. When meshing is complete, the boundaries are defined and a 3D mesh is written to the file.

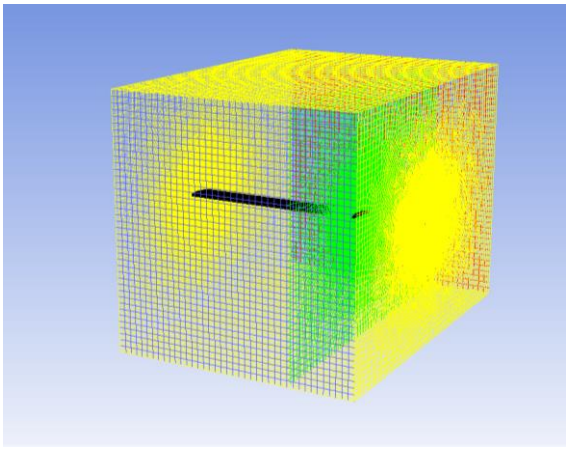

Figure 9-5 Mesh inside the computational domain

9.3 Implementation of MOGA

9.3.1 Flow Field Computation

FLUENT is used to solve for the coefficients of lift and drag for the 3D blade. A journal file is used to automatically initialize and evaluate each blade while saving a record of the relevant coefficients, C_L and C_D. The FLUENT journal initializes the calculations for a specified Reynolds number of 530000. Temperature and static pressure are defined at sea level conditions as 288.16 K and 101325 Pa respectively. These values are quite reasonable for a wind turbine whose maximum altitude does not exceed a few hundred meters. At this temperature and pressure, density is taken to be ρ = 1.225 kg/m^3 and laminar viscosity is taken as μ =1.7894x10^{-5} kg/m*s. The one equation S-A turbulence model is employed with MOGA. The S-A model gives a reasonable prediction of the aerodynamic performance at low Reynolds numbers.

9.3.2 Blade Section Parameterization

Since the blade shape studied is straight and untapered, there is no need to parameterize the shape in the spanwise direction. The cross sectional shapes, which are airfoils, are parameterized

using Bezier curves. Figure 9-6 shows an example of Bezier curves. The airfoil is divided into top and bottom boundary. Since a large number of blade shapes are evaluated for their aerodynamic performance during the optimization process, control points are allowed to move for different shapes. Some constraints are employed, including the maximum thickness constraints and constraints on coordinates boundaries. The maximum thickness of the airfoils varies from 0.11c to 0.13c. The boundaries for the Bezier control points are shown in Table 9-1.

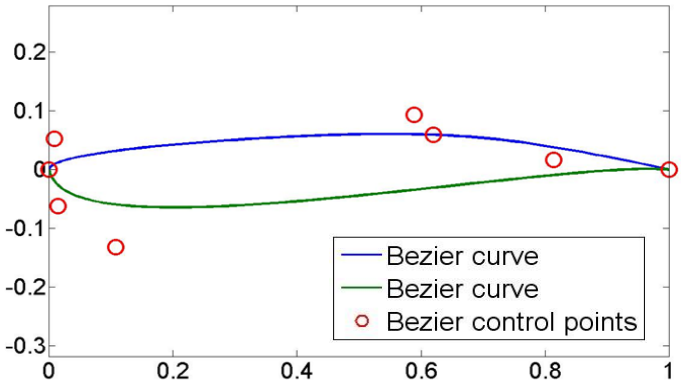

Figure 9-6 Example of Bezier Curve and Bezier control points

Table 9-1 Constraints for Bezier control points

Airfoil		**NACA 0012**
Top Boundaries	x_1	0.03
	x_2	0.8
	x_3	1
	y_1	0.09
	y_2	0.11
	y_3	0.11
	m_1	0.04
	m_2	0.4
	m_3	1
	n_1	-0.02
	n_2	-0.02
	n_3	0.02
Airfoil		**NACA 0012**
Bottom Boundaries	x_1	0
	x_2	0.03
	x_3	0.8
	y_1	0.02

	y_2	0.04
	y_3	0.04
	m_1	0
	m_2	0.04
	m_3	0.4
	n_1	-0.09
	n_2	-0.2
	n_3	-0.04

9.3.3 Algorithm Implementation

Employing the NSGA-II and the jMetal single- and multi-objective GA software packages mentioned in Chapter 4, this study employs a generation size of 20 individuals with a crossover probability of 0.9. The mutation rate is determined as 1/(the number of variables). The crossover section uses the simulated binary crossover (SBX) operator. The mutations section uses the polynomial mutation operator. The selection operator uses the binary tournament operator.

For MOGA, there are two objectives in the calculation: objective 1 is to minimize (100**Cd/Cl*) and objective 2 is to minimize (10/*Cl*). Convergence is determined by only focusing on the individual that always has the best performance of objective 1 and correspondingly the worst performance of objective 2 in the Pareto-solution of each generation. When the two objectives of this individual are not changing, the convergence is met.

9.4 Results and Discussion

9.4.1 Optimization Results

The primary objective of this optimization case is to maximize both C_L / C_D and C_L at moderate angle-of- attack. The angle-of-attack is chosen as 5 degree. Figure 9-7 shows the typical evolution history of the optimization. In this figure, we plot the normalized objectives versus the generation number. Among the many individuals in one generation, we define the individual

with the minimum objective 1 (100*C_D/C_L) and therefore the maximum objective 2 (10/C_L) as the best individual in the generation. This is identical with the convergence criteria employed before in previous chapters. Then, we take the normalization process as dividing all the objectives of the best individual in each generation by the objectives in the first generation. Their plots can be seen in Figure 9-7. As shown in Figure 9-7, both the objectives converge very quickly in the first several generations and are stable for a very long time, which means they have converged to the optimized solutions. Table 9-2 shows the C_L, C_D and C_L/C_D of the optimized blade compared to the original blade using the NACA 0012 as cross section shape.

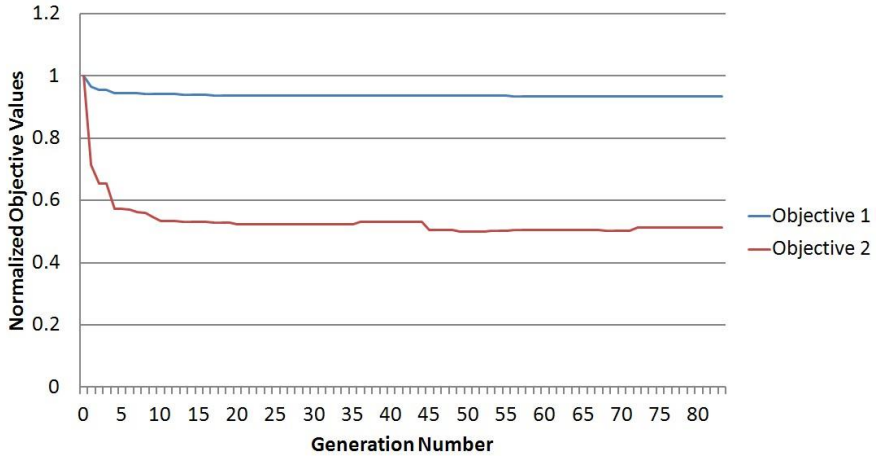

Figure 9-7 Convergence history for the best airfoil in each generation

Table 9-2 Comparison of the aerodynamic properties of the optimized and original blade sections

Airfoil	Maximum Thickness	C_L / C_D		C_L		C_D	
		optimized	original	optimized	original	optimized	original
NACA 0012	0.11c	23.2	19.91	0.74258	0.42153	0.032	0.02117

Figures 9-8 shows (a) the optimized shape of the cross-section area and (b) the whole optimized shape of the blade. Figure 9-9， 9-10， 9-11 and 9-12 show (a) the pressure distribution (b) the velocity contours at wing root, wing mid-span, 3/4 span of wing and wing tip respectively. Figure 9-13 shows the comparison of pressure coefficient distributions at various locations along the wing span from root to tip.

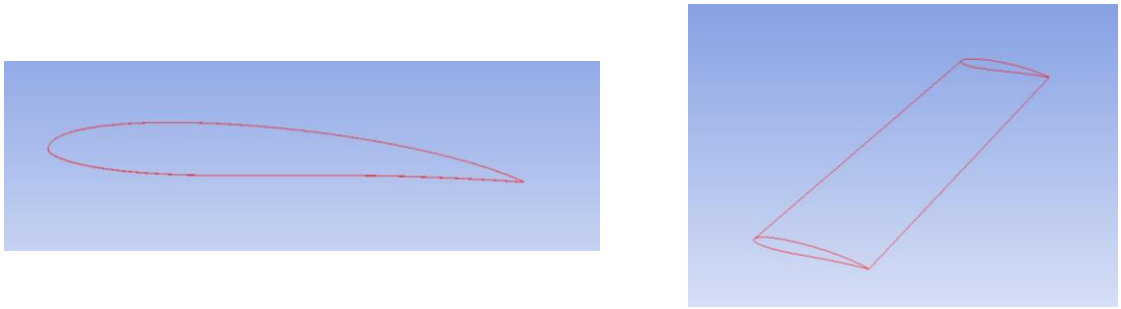

(a) optimized shape of the cross-section area (b) whole optimized wing/blade

Figure 9-8 Shape of the optimized wing/blade

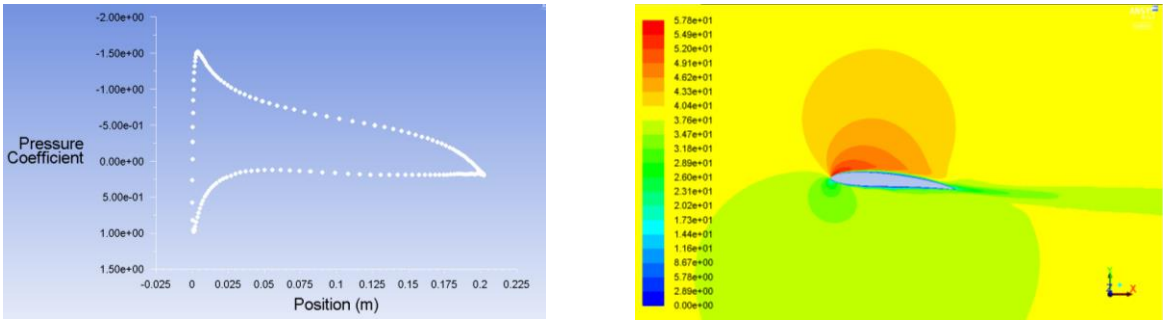

(a) pressure coefficient distribution (b) velocity contours

Figure 9-9 Aerodynamic performance at root of the optimized wing/blade

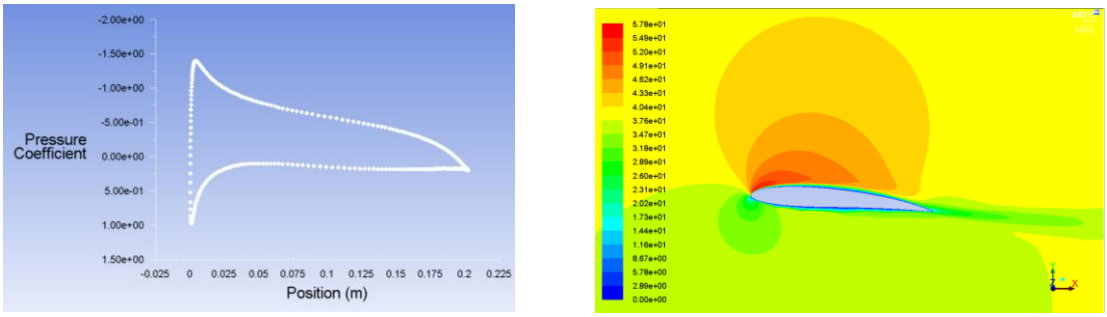

(a) pressure coefficient distribution (b) velocity contours

Figure 9-10 Aerodynamic performance at mid-span of the optimized wing/blade

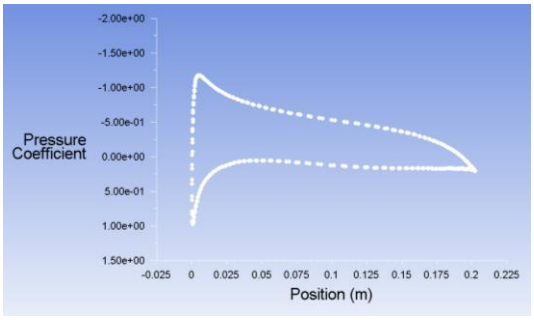

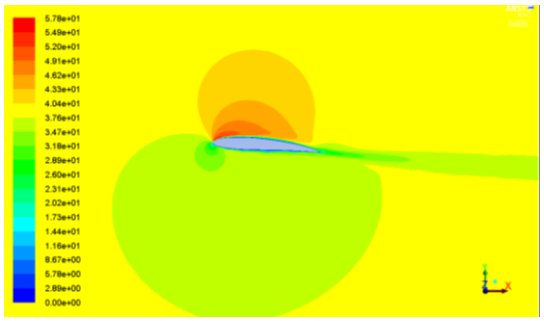

(a) pressure coefficient distribution (b) velocity contours

Figure 9-11 Aerodynamic performance at 0.75-span of the optimized wing/blade

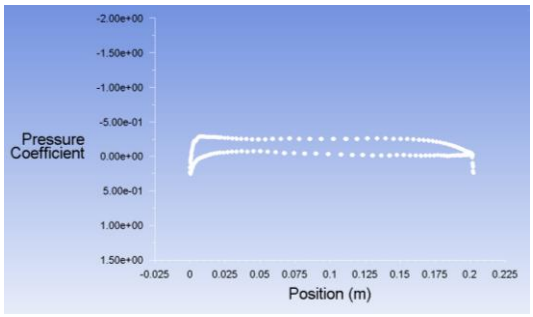

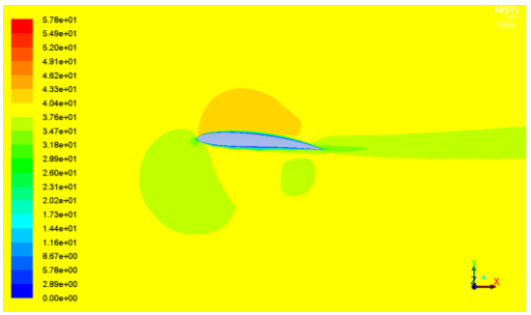

(a) pressure coefficient distribution (b) velocity contours

Figure 9-12 Aerodynamic performance at tip of the optimized wing/blade

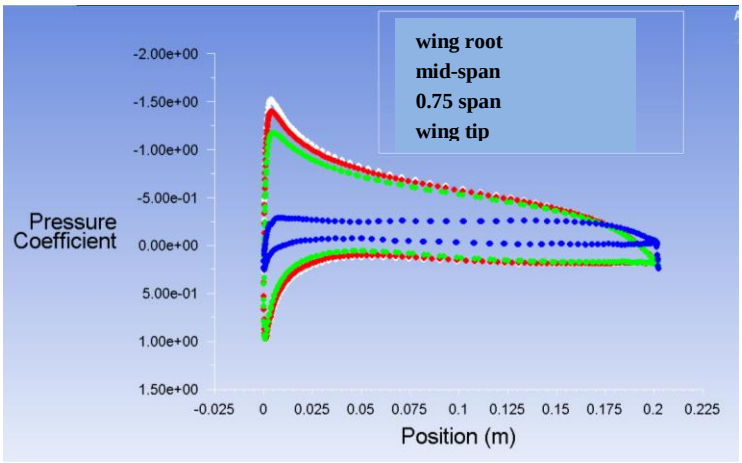

Figure 9-13 Comparison of pressure coefficient distribution at various locations of the optimized wing/blade

9.4.2 Discussions

Figure 9-14 shows the comparison of cross-section shapes between the optimized and original wing. As described before, the original wing uses NACA 0012 airfoil as cross-section. Figures 9-15 to 9-18 show the comparisons of pressure coefficient distribution on the airfoil surface at 4 locations along the wing: wing root, mid-span, 0.75span and wing tip. The shape comparison indicates that the optimized wing has a more cambered cross section shape while the maximum thickness is kept almost unchanged.

Comparing the figures of pressure coefficient distribution, one can notice that for the same location, the optimized airfoil has greater pressure difference at the trailing half of the body than the original NACA 0012 airfoils. This can be explained by the shape difference between the original and optimized airfoil.

For the same kind of airfoils, no matter the original or the optimized shape, the pressure difference between the top and bottom surface is the largest at wing root and smallest at the wing tip. Besides, the decrease in the pressure difference becomes greater when it gets close to the wing tip. This indicates that the wind tip effects strongly affect the aerodynamic behavior of the wing near the wing tip region. Therefore, it's very important to capture the real physics at the wing tip area to get a good evaluation of the aerodynamics of the wing. On the top surface the optimized airfoil, due to its more cambered shape, it results in a lower pressure than the original airfoil. On the bottom surface the situation reverses, resulting in a higher pressure than the original airfoil. This is the reason for higher C_L. However, due to more cambered shape, the drag of the optimized airfoil increases. Since the focus of this study is more on the overall performance, namely C_L/C_D, as long as the lift to drag ratio increases and lift doesn't decrease, the optimized results are considered acceptable. This is proven by the results in Table 9-2. The results also demonstrate the advantage of MOGA optimization method.

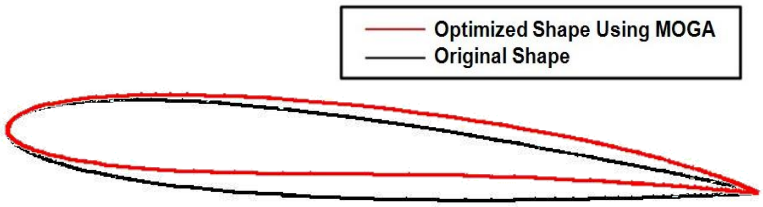

Figure 9-14 Comparison of optimized and original shape of the cross section

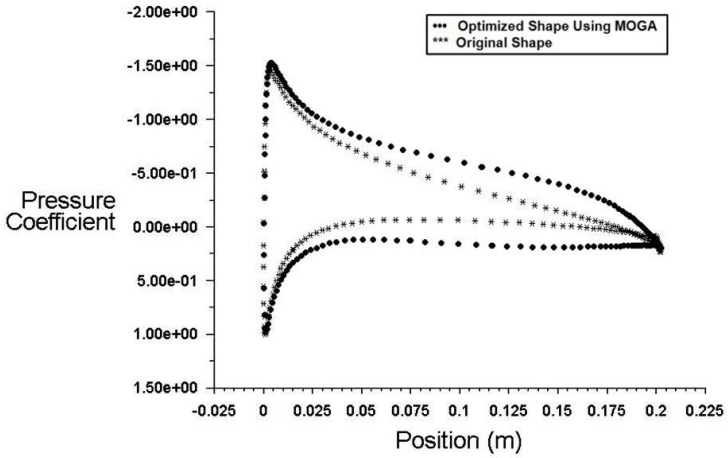

Figure 9-15 Comparison of pressure coefficient distributions at root of the optimized and original wings

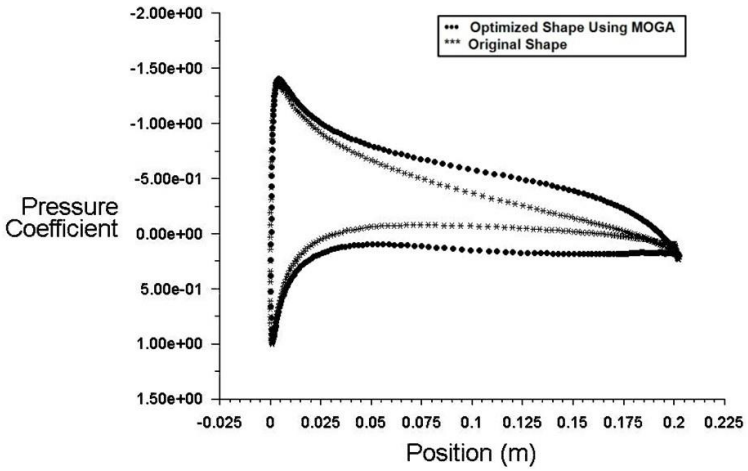

Figure 9-16 Comparison of pressure coefficient distributions at mid-span of the optimized and original wings

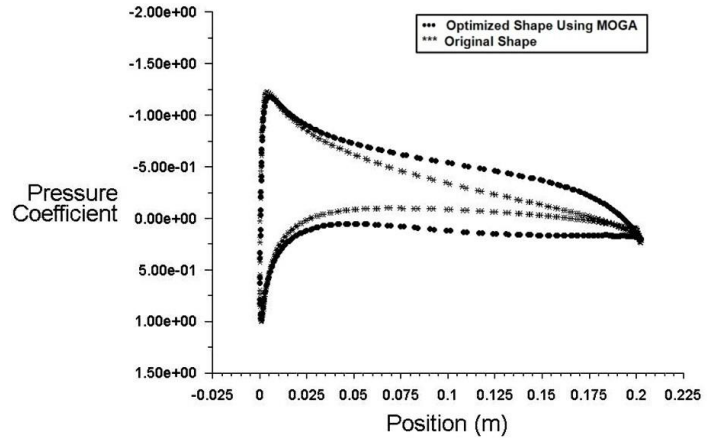

Figure 9-17 Comparison of pressure coefficient distributions at 0.75-span of the optimized and original wings

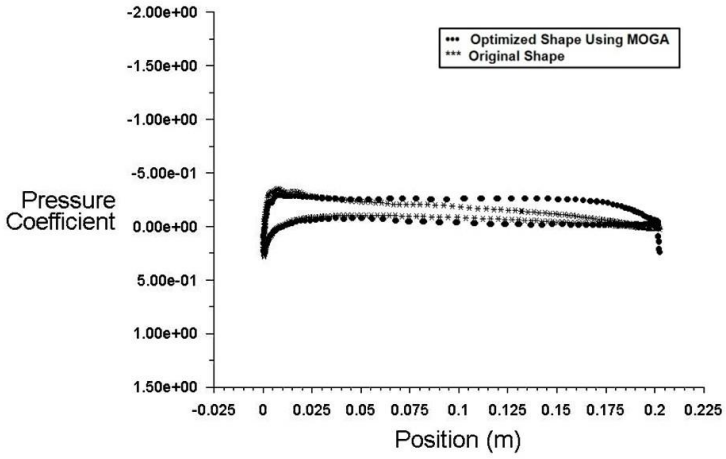

Figure 9-18 Comparison of pressure coefficient distributions at tip of the optimized and original wings

Chapter 10 Conclusions

The focus of this dissertation has been on development and application of optimization techniques to optimization of wind-turbine blades and wind-farm layout. This work has made contributions in the following areas:

(1) Developed a powerful optimization methodology for wind turbine airfoil/wing applications using both single- and multi- objective genetic algorithms integrated with CFD tools.

(2) Successfully optimized several widely used wind turbine airfoils.

(3) Developed and applied the Blade Element Momentum theory based code to determine the power output of HAWT using a variety of thick airfoils. In addition, improved the BEM method by integrating a simplified dynamic inflow model to capture the instantaneous behavior of wind turbines under varying wind conditions.

(4) Developed and improved several existing wind turbine wake models to optimize the distributions of both Horizontal- Axis and Vertical- Axis Wind Turbines in large-scale wind farms for greater power generation.

In the first part of this dissertation, the optimization methodology was validated by performing the shape optimization of 4 subsonic and transonic airfoils. The optimization objectives were to reduce drag by achieving shock-free airfoils while maintaining the lift within an acceptable range. The optimization results showed that the GA technique can be employed efficiently and accurately to produce globally optimal airfoils with excellent aerodynamic properties using a desired objective value (C_l and/or C_d and/or C_l /C_d). In addition, this part of the study also demonstrated that the application of multi-objective GA can result in superior shock-free airfoils by minimizing the drag and maximizing the lift to drag ratio.

In second part of this dissertation, GA techniques are applied to the shape optimization of thick wind-turbine airfoils including Flatback airfoils, FX 66-S196-V1, DU 91-W2-250, NACA 64418 and NACA 64421 airfoils. The optimization targets were to improve the aerodynamic performance of the airfoils by improving C_l/C_d and/or C_l. For Flatback airfoils, both the single- and multi- objective GA were applied, MOGA demonstrated superior performance in achieving multiple optimization targets. The MOGA technology was then applied to optimizing FX 66-S196-V1, DU 91-W2-250, NACA 64418 and NACA 64421 airfoils. The optimization results showed that the application of multi-objective GA can result in superior airfoil by maximizing both the lift and lift to drag ratio.

In the third part of this dissertation, the primary focus has been to investigate the effect of blade airfoil sections on power output of a wind turbine. An improved Blade Element Momentum theory based code was developed for this purpose. The BEM code was validated by comparing its results with experimental data available for NREL Phase II and Phase III turbines and the Risoe turbine. It was shown that the wind turbines with thick airfoil sections can generate greater power than the original NREL Phase II, Phase III and Risoe wind turbines particularly at higher wind speeds (larger than 10 m/s). In addition, a simplified dynamic inflow aerodynamic model was included in the BEM code to capture the behavior of the wake behind an operating wind turbine. The basic BEM code was modified into a new BEM method designated $\text{BEM}^{\text{inflow}}$. The original NREL Phase II, Phase III and Risoe wind turbines were evaluated for their power generation at a wind speed of 12 m/s with input operating rotational speed changing from zero to rated operating values. The results from $\text{BEM}^{\text{inflow}}$ and original BEM code were compared. It was shown that $\text{BEM}^{\text{inflow}}$ code can capture the instantaneous change in wind velocity while the basic BEM method can only calculate the steady state behavior.

In the fourth part of this dissertation, the results demonstrate that the layout optimization of a HAWT wind farm using GA gives a uniform grid arrangement similar to that obtained by Grady et al. [53]; this is different from that obtained by Mosetti who obtained a somewhat random arrangement. The choice of the wake model has little effect on the layout; however there are small differences in the total power output. The use of a more realistic wake model due to Werle [97] is suggested for study of layout of larger HAWT and bigger wind farms. The results

obtained for a VAWT wind farm should be considered preliminary because of the use of a very simplified wake model.

In the last part of this dissertation, a preliminary optimization study was performed for a 3D straight-bladed untaperd wind turbine blade with a cross section of NACA 0012 airfoil. The optimization objectives were to achieve optimal cross section shape with improved C_L/C_D and C_L. The flow field was modeled as a physical wind tunnel and the blade surfaces were considered for wind tip effects. The optimization results demonstrated superior performance of the optimized blades using the MOGA technology.

Chapter 11 Future Work

The main focus of this work has been the optimization of 2D wind turbine airfoils. In the future, other more commonly used wind turbine airfoils can be included for the optimization and evaluated for their impact on generation of wind power.

With more airfoils being considered for optimization, a database of the optimized airfoils including their aerodynamic properties could be established for a wide range of operating conditions (Reynolds numbers, angle of attack, etc). This will lead to more choices in developing efficient wind-turbine blades. More realistic dynamic inflow models should be added in the BEM^{inflow} code.

For the wind farm optimization, future work may focus on extending the current models to more realistic conditions for a large-scale wind farm, taking into account variations in wind speed and directions and a combination of HAWT and VAWT of varying sizes. Additional work could also take into account bigger size VAWT of different type with more realistic wake models for wind farms. In addition, a comparative cost and power study should be performed to determine the relative economics of HAWT and VAWT wind farms.

References

1. GWEC, Global Wind Statistics 2011.
2. U.S. Department of Energy. Advantages and Challenges of Wind Energy. Wind Program 2013; Available from: https://www1.eere.energy.gov/wind/wind_ad.html.
3. Lee, H., Manwell, J., Gray, T. Historic Wind Development in New England. 2011; Available: http://www.windpoweringamerica.gov/newengland/history_windfarms.asp.
4. American Wind Energy Association (AWEA), AWEA 4th Quarter 2012 Public Market Report.
5. National Renewable Energy Laboratory. Installed Wind Capacity. 2013 ; Available: http://www.windpoweringamerica.gov/wind_installed_capacity.asp. [cited 2012 January 19]
6. U.S. Energy Information Administration, Electric Power Monthly. 2013, U.S. Department of Energy.
7. American Wind Energy Assiciation, AWEA U.S. Wind Industry Fourth Quarter 2012 Market Report. 2013.
8. American Wind Energy Association, AWEA press release. 2013.
9. Wind power in the United States. 2013 [cited 2013 August 20th]; Available from: http://en.wikipedia.org/wiki/Wind_power_in_the_United_States.
10. Turkey in the Wind. 2007 [cited 2013 August 20th]; Available from: http://jcwinnie.biz/wordpress/?p=2330.
11. Gipe, P. Vertical Axis Wind Turbine. Wind-works.org 2013 [cited 2013 August 20th]; Available from: http://www.wind-works.org/cms/index.php?id=399&tx_ttnews[tt_news]=2194&cHash=d1b21f3bd1f35d9e4804f1598b27bd86.
12. Brower, M.C., Robinson, N.M., Hale, E., Wind Flow Modeling Uncertainty. 2010, AWS Trupower, LLC: Albany, NY.
13. Tymos, B. Wind Turbines - Betz Law Explained. 2009 [cited 2013 August 20]; Available from: http://c21.phas.ubc.ca/article/wind-turbines-betz-law-explained.

14. Wilson, S., Shepherds Flat Wind Farm 2011. 2011.
15. Foley, J.A. Noise from Offshore Wind Farm Construction Could Harm Marine Marine Mammal Life. Nature World News 2013 [cited 2013 September 5]; Available from: http://www.natureworldnews.com/articles/4751/20131104/noise-offshore-wind-farm-construction-harm-marine-mammal-life.htm.
16. Laird, D., Blade Design Codes. Sandia National Laboratories, 2004 Wind Turbine Blade Workshop.
17. Perez-Blanco, H., McCaffrey, M. Aerodynamic Performance of Preferred Wind Turbine Airfoils. in Proceeding of ASME Turbo Expo 2012: Power for Land, Sea and Air, GT 2012. Copenhagen, Denmark.
18. Harbeck, M., Jameson, A., Exploring the limits of shock-free transonic airfoil design, in In: 43rd Aerospace Sciences Meeting and Exhibit. New York: AIAA: Reno, NV, USA.
19. Leoviriyakit, K., Jameson, A., Multi-point wing planform optimization via control theory, in In: 43rd AIAA Aerospace Sciences Meeting & Exhibit. 2005, New York: AIAA: Reno, NV, USA.
20. Ceyhan, O., Sezer-Uzol, N., Tuncer, I.H. Optimization of horizontal axis wind turbines by using BEM theory and genetic algorithm. in Proceedings of the 5th Ankara International Aerospace Conference. METU, Ankara, Turkey.
21. Chen, X., Agarwal, R., Optimization of Flatback Airfoils for Wind-Turbine Blades Using a Genetic Algorithm. J. of Aircraft. Vol. 49(No. 2): p. pp. 622-629.
22. Chen, X., Agarwal, R., Optimization of FX, DU and NACA Airfoils for Wind Turbine Blades Using a Multi-Objective Genetic Algorithm, in 51st AIAA Aerospace Sciences Meeting. Grapevine, TX.
23. Grasso, F., Development of Thick Airfoils for Wind Turbines, in 50th AIAA Aerospace Sciences Meeting. 2012: Nashville, TN, USA.
24. DeFalcot, I., DelBalio, R., Cioppa, A.D., Tarantino, E. A parallel genetic algorithm for transonic airfoil optimisation. in In Proceeding of International Conference on Evolutionary Computation. 1995.
25. Brian, J.R., William, C.A., Anastasios, L.S., Aerodynamic and Aeroacoustic Optimization of Airfoils via a Parallel Genetic Algorithm, in AIAA Paper, 98-4811.

26. ANSYS Inc., ANSYS, Inc. Software Products.
27. Hicks, R.M., Murman, E.M., Vanderplaats, G.N., An assessment of airfoil design by numerical optimization. July 1974.
28. Hicks, R.M., Vanderplaats, G.N., Application of numerical optimization to the design of supercritical airfoils without drag-creep. 1977.
29. Jameson, A., Aerodynamic design via control theory.
30. Drela, M., Design and optimization method for multi-element airfoils.
31. Cosentino, G.B., Holst, T.L., Numerical optimization design of advanced transonic wing configurations. Journal of Aircraft, 1986. 23: p. 129-199.
32. Glauert, H., The Analysis of Experimental Results in the Windmill Brake and Vortex Ring States of an Airscrew. 1926.
33. Wilson, R.E., Aerodynamic Behavior of Wind Turbines, in Wind Turbine Technology, D.A. Spera, ed, Editor. 1994, The American Society of echanical Engineers: New York, NY. p. 231-232.
34. Ragheb, M. Theory of Wind Machines Betz equation. 2008 March 15, 2010].
35. Fuglsang, P., Madsen, H.A., Optimization method for wind turbine rotors. Journal of Wind Engineering and Industrial Aerodynamics, 1999. 80(1-2): p. 191-206.
36. Stiesdal, H., The wind turbine, components and operation. 1999.
37. Hansen, M.O.L., Aerodynamics of wind turbines. 2000: James and James Science Publisher Ltd.
38. Benini, E., Toffolo, A., Optimal design of horizontal-axis wind turbines using blade-element theory and evolutionary computation. Journal of Solar Energy Engineering, 2002. 124(4): p. 357-363.
39. Grauer, A., Efficiency of three wind energy generator systems. IEEE Transactions on Energy Conversion. Vol. 11(No. 3): p. 650-657.
40. Tan, C.M. A Comparative Study of Evolutionary Algorithm and Swarm Algorithm for Airfoil Shape Optimization Problems. in Proc. of 41st Aerospace Sciences Meeting and Exhibit. Reno, Nevada.
41. Alpman, E., Airfoil Shape Optimization Using Evolutionary Algorithms. Aerospace Engineering Department, Pennstate University.

42. Burger, C., Roy, H. Wind Turbine Airfoil Performance Optimization using the Vortex Lattice Method and a Genetic Algorithm. in Proc. of 4th AIAA Energy Conversion Conference. San Diego, CA.
43. Schmidt, M.F., The economic optimization of wind turbine design, in Mechanical Engineering. 2007, Georgia Institute of Technology.
44. Kenway, G., Martins, R.R.A.J. Aerostructural Shape Optimization of Wind Turbine Blades Considering Site-Specic Winds. in Proc. of 12th AIAA/ISSMO Multidisciplinary Analysis and Optimization Conference. British Columbia, Canada, Victoria.
45. Xuan, H., et. al, Aerodynamic and Aeroacoustic Optimization of a Wind Turbine Blade by a Genetic Algorithm. 2008, China Academy of Aerospace Aerodynamics.
46. Vicini, A., Quagliarella, D., Inverse and Direct Airfoil Design Using a Multiobjective Genetic Algorithm. AIAA Journal. 35(9): p. 1499-1505.
47. Bourguet, R., Martinat, G., Harran, G., Braza, M., Aerodynamic multi-criteria shape optimization ofvawt blade profile by viscous approach. Wind Energy 2007: p. 215–219.
48. Rahai, H., Hefazi, H., Vertical axis wind turbine with optimized blade profile.
49. Sun, H., Wind turbine airfoil design using response surface method. Journal of Mechanical Science and Technology, 2011. 25(5): p. 1335-1340.
50. Lee, K., Kim, K., Lee, D., Lee, K., Park, J., Two-step optimization for wind turbine blade with probability approach. Journal of Solar Energy Engineering, 2010. 132.
51. Casás, V.D., Peña, F.L., Duro, R.J. Automatic design and optimization of wind turbine blades. in Proc. of the International Conference on Computational Intelligence for Modeling Control and Automation and International Conference on Intelligent Agents Web Technologies and International Commerce (CIMCA'06). 2006. Sydney, Australia
52. Mosetti, G., Poloni, C., Diviacco, B., Optimization of Wind Turbine Positioning in Large Wind Farms by Means of a Genetic Algorithm. J. of Wind Engineering and Aerodynamics, 1994. 51: p. 105-116.
53. Grady, S.A., Hussaini, M.Y., Abdulla, M.M., Placement of Wind Turbines Using Genetic Algorithms. Renewable Energy, 2005. 30: p. 259-270.
54. Wan, C., Wang, J., Yang, G., Li, X., Zhang, X. Optimal Micro-Siting of Wind Turbines by Genetic Algorithms Based on Improved Wind and Turbine Models. in Proc. of Joint

48th IEEE Conference on Decision and Control and 28th Chinese Control Conference. Shanghai, China.

55. Jensen, N.O., A Note on Wind Generator Interaction. 1993, Riso National Laboratory, Rosklide, Denmark.
56. Katic, I., Høstrup, J., Jensen, N.O. A simple model for cluster efficiency. in In EWEC'86. 1986. Rome.
57. Bansal, R., Shatti, T., Kothari, D., On some of the design aspects of wind energy conversion systems. Energy Conversion and Management, 2002. 43(16): p. 2175-87.
58. Erkut, E., Neuman, S., A survey of analytical models for locating undesirable facilities. European Journal of Operational Research, 1989. 40(275).
59. Patel, M., Wind and solar power systems. 1999, Boca Raton: CRC Press.
60. Ozturk, U., Norman, B., Heuristic methods for wind energy conversion system positioning. Electric Power Systems Research. 70(3): p. 179–85.
61. Lackner, M.A., Elkinton, C.N., An analytical framework for offshore wind farm layout optimization. Wind Engineering, 2007. 31(17).
62. Castro Mora, J., Calero Baron, J.M., Riquelme Santos, J.M., Burgos Payan, M., An evolutive algorithm for wind farm optimal design. Neurocomputing, 2007. 70(2651).
63. Kusiak, A., Song, Z., Design of wind farm layout for maximum wind energy capture. Renewable Energy 2010. 35: p. 685–694.
64. Dabiri, J.O., Potential order-of-magnitude enhancement of wind farm power density via counter-rotating vertical-axis wind turbine arrays J. of Renewable Sustainable Energy, 2011. 3(4): p. 3104.
65. Mittal et al. Investigation of two analytical wake models using data from wind farms. in Proceedings of the ASME 2011 International Mechanical Engineering Congress & Exposition.
66. Ishihara, T., Yamaguchi, A., Fujino, Y., Development of a New Wake Model Based on a Wind Tunnel Experiment. Global Wind Power, 2004.
67. Gonzalez, J.S., Optimization of Wind Farm Turbine Layout Including Decision Making Under Risk. IEEE Systems Journal, 2012. 6(1).

68. Chen et al., Wind farm layout optimization using genetic algorithm with different hub height wind turbines, in IMECE2011. Denver, Colorado, USA.
69. TPI Composites Inc., Innovative Design Approaches for Large Wind Turbine Blades. 2003.
70. TPI Composites Inc., Innovative Design Approaches for Large Wind Turbine Blades—Final Report. 2004.
71. Standish, K.J., van Dam, C.P., Aerodynamic Analysis of Blunt Trailing Edge Airfoils. ASME J. Sol. Energy Eng., 2003. 125(4): p. 479–487.
72. Van Rooij, R.P.J.O.M., Timmer, W.A., Roughness Sensitivity Considerations for Thick Rotor Blade Airfoils. ASME J. Sol. Energy Eng., 2003. 125(4): p. 468–478.
73. Baker, J.P., Mayda, E.A., van Dam, C.P., Experimental Analysis of Thick Blunt Trailing Edge Wind Turbine Airfoils. ASME J. of Solar Energy Eng., 2006. 128: p. 422-431.
74. Gooden, J.H.M., Experimental Low-Speed Aerodynamic Characteristics of the Wortmann FX 66-S-196 VI Airfoil. Technical Soaring, 1979. 5(3): p. 21.
75. Timmer, W.A., van Rooij, R.P.J.O.M., Summary of the Delft University Wind Turbine Dedicated Airfoils. Journal of Solar Energy Engineering, 2003. 125: p. 488-496.
76. Timmer, W.A., An Overview of NACA 6-digit Airfoil Series Characteristics with Reference to Airfoils for Large Wind Turbine Blades, in AIAA 47th Aerospace Sciences Meeting. Orlando, Florida
77. Alexander, G. NACA Airfoil Series. Aerospaceweb.org [cited 2013 March 22nd]; Available from: http://www.aerospaceweb.org/question/airfoils/q0041.shtml.
78. GAMBIT 6.2, Geometry and Mesh Generation Preprocessor. 2007, Ansys Inc.
79. Goldberg, D.E., Genetic Algorithms in Search, Optimization & Machine Learning. 1st ed ed. 1989, Boston: Addison-Wesley Professional.
80. Srinivas, N., Deb, K., Multi-objective function optimization using non-dominated sorting genetic algorithms. Evolutionary Computation, 1994. 2(3): p. 221–248.
81. Konak, A., Coit, D.W., Smith, A.E., Multi-objective optimization using genetic algorithms: A tutorial. Reliability Engineering and System Safety, 2006. 9: p. 992-1007.
82. Deb, K., Pratap, A., Agarwal, S., et al., A fast and elitist multi-objective genetic algorithm: NSGA-II. IEEE Transactions on Evolutionary Computation 2002. 6(2).

83. Deb, K. Single and multi-objective optimization using evolutionary computation. in Proceedings of the 6th International Conference on Hydro-informatics 2004. Singapore: World Scientific.
84. Durillo, J.J., Nebro, A.J., Alba, E. The jMetal framework for multi-objective optimization: Design and architecture. in In: Proceedings of the IEEE congress on evolutionary computation. 2010. Barcelona, Spain: IEEE.
85. ANSYS Inc., ANSYS user manual.
86. Sederberg, T. BYU Bézier curves.
87. Vanderplaats, G.N., Numerical Optimization Techniques for Engineering Design: with Applications. 1984, New York: Mc Graw Hill.
88. Franke, M. RAE 2822 Aerofoil. 2003; Available from: http://www.cfd.tu-berlin.de/research/thermofluid/transport/node6.html
89. Padovan, L., Pediroda, V., Poloni, C., Multi objective robust design optimization of airfoils in transonic field, in Multidisciplinary Methods for Analysis Optimization and Control of Complex Systems, Mathematics in Industry, Capasso, V., Periaux, J., Editor. 2005, Springer-Verlag: Berlin Heidelberg. p. 283-295.
90. Abdol-Hamid, K.S., Lakshmanan, B., Carlson, R., Application of navier-stokes code PAB3D with k-ε turbulence model to attached and separated flows, NASA technical paper. 1995.
91. Gregory, N., Wilby, P.G., NPL 9615 and NACA 0012: A comparison of aerodynamic data, in Report for Aeronautical Research Council of U.K., H.M. Stationery Office. 1973.
92. Tangler, J.L., Somers, D.M. , NREL Airfoil Families for HAWTS. 1995.
93. Chen, X., Agarwal, R. , Optimization of Flatback Airfoils for Wind Turbine Blades Using a Genetic Algorithm, in AIAA Aerospace Sciences Meeting. 2010: Orlando, FL.
94. Bertagnolio, F., Sørensen, N.N., Johansen, J., Fuglsang, P., Wind Turbine Airfoil Catalogue. 2001, Risø National Laboratory: Roskilde, Denmark.
95. Henriksen, L.C., Hansen, M.H., Poulsen, N.K., A simplified dynamic inflow model and its effect on the performance of free mean wind speed estimation. Wind Energy, 2012.
96. Vertical axis wind turbines v/s horizontal axis Wind Turbines. Energy-XS 2010; Available from: http://www.energyexcess.com/node/7.

97. Werle, M.J., A New Analytical Model for Wind Turbine Wakes. Flodesign Inc.: Wilbraham, MA.
98. Manwell, J.F., Mcgowan, J.G., Rogers, A.L., Wind Energy Explained. 2009: Wiley.
99. Jacobs, E.N., Sherman, A., Airfoil Section Characteristics as affected by Variations of the Reynolds Number. 1937.
100. Global Energy Concepts, in Wind Turbine Technology Overview. 2005. p. 7.
101. Staelens, Y., Saeed, F., Paraschivoiu, I., A Straight-bladed Variable-pitch VAWT Concept for Improved Power Generation. 2003.

Vita

Xiaomin Chen

Degrees

Ph.D., Mechanical Engineering, Washington University in St Louis, May 2014
M.S., Mechanical Engineering, Washington University in St Louis, May 2010
B.S., Mechanical Engineering, Shanghai Jiao Tong University, June 2008

Professional

American Society of Mechanical Engineering (ASME)
American Institute of Aeronautics and Astronautics (AIAA)

Publications

Xiaomin Chen and Ramesh Agarwal. "Optimization of Flatback Airfoils for Wind-Turbine Blades Using a Genetic Algorithm", *Journal of Aircraft*, Vol. 49, No. 2 (2012), pp. 622-629.

Xiaomin Chen and Ramesh Agarwal. "Optimization of flatback airfoils for wind turbine blades", *Aircraft Engineering and Aerospace Technology*, Vol. 85 Iss: 5(2013), pp.355 – 365.

Xiaomin Chen and Ramesh K. Agarwal. "Optimization of Wind Turbine Blade Airfoils Using a Multi-Objective Genetic Algorithm", *Journal of Aircraft*, Vol. 50, No. 2 (2013), pp. 519-527. doi: 10.2514/1.C031910.

Xiaomin Chen and Ramesh K. Agarwal. "Shape optimization of airfoils in transonic flow using a multi-objective genetic algorithm", *Proceedings of the Institution of Mechanical Engineer, Part G: Journal of Aerospace Engineering*, published online before print August 27, 2013, doi: 10.1177/0954410013500613.

Xiaomin Chen and Ramesh K. Agarwal. "Optimal placement of horizontal – and vertical – axis wind turbines in a wind farm for maximum power generation using a genetic algorithm", *International Journal of Energy and Environment*, Vol. 3, Iss: 6 (2012), pp.927-938.

Xiaomin Chen and Ramesh K. Agarwal. "Assessment of the performance of various airfoil sections on power generation from a wind turbine using the blade element momentum theory", *International Journal of Energy and Environment*, Vol. 4, Iss: 5 (2013), pp.835-850.

Xiaomin Chen and Ramesh K. Agarwal. "Optimization of Flatback Airfoils for Wind Turbine

Blades Using a Genetic Algorithm with an Artificial Newral Network", *the 48th AIAA Aerospace Science Meeting Including the New Horizons Forum and Aerospace Exposition*, 4-7 January 2010, Orlando, Florida.

Robert Fares and Xiaomin Chen. "Shape Optimization of an Axisymmetric Diffuser and a 3D Hydro-turbine Draft Tube Using a Genetic Algorithm", *2010 Missouri Space Grant Consortium*, April 2010, Rolla, Missouri.

Xiaomin Chen and Ramesh K. Agarwal. "Optimal placement of horizontal – and vertical – axis wind turbines in a wind farm for maximum power generation using a genetic algorithm", *the 5th International Conference on Energy Sustainability*, August 7-10, 2011, Washington DC.

Xiaomin Chen and Ramesh K. Agarwal. "Optimization of Flatback Airfoils for Wind Turbine Blades Using a Multi-Objective Genetic Algorithm ", *ASME 2012 6th International Conference on Energy Sustainability*, Parts A and B, July 23-26, 2012, San Diego, California.

Xiaomin Chen and Ramesh K. Agarwal. "Optimization of FX, DU and NACA airfoils for wind turbine blades using a multi-objective genetic algorithm", *the 51st Aerospace Sciences Meeting*, January 7-10, 2013, Grapevine, TX.

Xiaomin Chen and Ramesh K. Agarwal. "Shape optimization of airfoils in transonic flow using a multi-objective genetic algorithm", *the 43rd AIAA Fluid Dynamics Conference*, June 24-27, 2013, San Diego, CA.

Xiaomin Chen and Ramesh K. Agarwal. "Assessment of the performance of various airoil sections on power generation from a wind turbine using the blade element momentum theory", *the 7th International Conference on Energy Sustainability*, July 14-19, 2013, Minneapolis, MN.